The Planetary Science Journal, 5:213 (47pp), 2024 September https://doi.org/10.3847/PSJ/ad5b5e

Geophysical Observations of the 2023 September 24 OSIRIS-REx Sample Return Capsule Reentry

Elizabeth A. Silber[1], Daniel C. Bowman[2], Chris G. Carr[3], David P. Eisenberg[4], Brian R. Elbing[5], Benjamin Fernando[6], Milton A. Garcés[7,8], Robert Haaser[9], Siddharth Krishnamoorthy[10], Charles A. Langston[11], Yasuhiro Nishikawa[12], Jeremy Webster[3], Jacob F. Anderson[13], Stephen Arrowsmith[14], Sonia Bazargan[11], Luke Beardslee[15], Brant Beck[4], Jordan W. Bishop[3], Philip Blom[3], Grant Bracht[4], David L. Chichester[16], Anthony Christe[17], Jacob Clarke[14], Kenneth Cummins[18], James Cutts[10], Lisa Danielson[3], Carly Donahue[3], Kenneth Eack[9], Michael Fleigle[2], Douglas Fox[5], Ashish Goel[10], David Green[19], Yuta Hasumi[12], Chris Hayward[14], Dan Hicks[20], Jay Hix[16], Stephen Horton[11], Emalee Hough[5], David P. Huber[21], Madeline A. Hunt[13], Jennifer Inman[22], S. M. Ariful Islam[11], Jacob Izraelevitz[10], Jamey D. Jacob[5], James Johnson[16], Real J. KC[5], Attila Komjathy[10], Eric Lam[23], Justin LaPierre[24], Kevin Lewis[6], Richard D. Lewis[25], Patrick Liu[23], Léo Martire[10], Meaghan McCleary[22], Elisa A. McGhee[26], Ipsita Mitra[11], Amitabh Nag[9], Luis Ocampo Giraldo[16], Karen Pearson[27], Mathieu Plaisir[18], Sarah K. Popenhagen[7], Hamid Rassoul[18], Miro Ronac Giannone[1,14], Mirza Samnani[10], Nicholas Schmerr[28], Kate Spillman[5], Girish Srinivas[4], Samuel K. Takazawa[7], Alex Tempert[18], Reagan Turley[28], Cory Van Beek[4], Loïc Viens[3], Owen A. Walsh[13], Nathan Weinstein[4], Robert White[29], Brian Williams[7], Trevor C. Wilson[5], Shirin Wyckoff[7], Masa-yuki Yamamoto[12], Zachary Yap[5], Tyler Yoshiyama[7], and Cleat Zeiler[29]

[1] Sandia National Laboratories, Geophysics, Albuquerque, NM 87123, USA; esilbe@sandia.gov
[2] Sandia National Laboratories, Geophysical Detection Programs, Albuquerque, NM 87123, USA
[3] Los Alamos National Laboratory, Earth and Environmental Sciences Division, PO Box 1663, Los Alamos, NM 87544, USA
[4] TDA Research Inc, 12345 W. 52nd Avenue, Wheat Ridge, CO 80033, USA
[5] Oklahoma State University, Mechanical and Aerospace Engineering, Stillwater, OK 74078, USA
[6] Johns Hopkins University, Department of Earth and Planetary Sciences, Baltimore, MD 21218, USA
[7] University of Hawaii, Infrasound Lab, 73970 Makako Bay Drive 205, Kailua-Kona, HI 96740, USA
[8] University of Hawaii, Applied Research Lab, 73970 Makako Bay Drive 117, Kailua-Kona, HI 96740, USA
[9] Los Alamos National Laboratory, ISR-2, P.O. Box 1663, MS-B241, Los Alamos, NM 87545, USA
[10] NASA Jet Propulsion Laboratory, California Institute of Technology, 4800 Oak Grove Drive, Pasadena, CA 91109, USA
[11] University of Memphis, Center for Earthquake Research and Information, 3876 Central Avenue, Ste. 1, Memphis, TN 38152, USA
[12] Kochi University of Technology, School of Systems Engineering, 185 Miyanokuchi, Tosayamada, Kami, Kochi, 7828502, Japan
[13] Boise State University, Geosciences, 1910 University Drive, Boise, ID 83725, USA
[14] Southern Methodist University, Earth Sciences, 3225 Daniel Avenue, Dallas, TX 75205, USA
[15] Silixa Ltd, 3102 Broadway Street, Suite E, Missoula, MT 59808, USA
[16] Idaho National Laboratory, Nuclear Nonproliferation Division, PO Box 1625, MS2212, Idaho Falls, ID 83415, USA
[17] RedVox, Inc., 73970 Makako Bay Drive 116, Kailua-Kona, HI 96740, USA
[18] Florida Institute of Technology, Geospace Physics Laboratory, 150 W. University Boulevard, Melbourne, FL 32901, USA
[19] AWE Blacknest, Brimpton Common, Reading, Berkshire, RG7 4RS, UK
[20] United States Department of Defense, KBR Consultant, Las Cruces, NM88011, USA
[21] University of Texas-El Paso, Earth, Environmental, and Resource Sciences, 500 W University, El Paso, TX 79902, USA
[22] NASA Langley Research Center, SCIFLI, Hampton, VA 23681, USA
[23] Air Force Research Laboratory, Sensing Effects & Analysis, 2241 Avionics Circle, Wright-Patterson AFB, OH 45433, USA
[24] Sandia National Laboratories, Atmospheric Science, Albuquerque, NM 87123, USA
[25] Defense Threat Reduction Agency (DTRA), 8725 John J. Kingman Road, Stop 6201, Fort Belvoir, VA 22060, USA
[26] Colorado State University, Department of Geosciences, 1482 Campus Delivery, Fort Collins, CO 80523, USA
[27] Independent Researcher, Bowie, MD 20715, USA
[28] University of Maryland, Dept. of Geology, College Park, MD 20742, USA
[29] Nevada National Security Sites, Science and Technology, 2621 Losee Road, North Las Vegas, NV 89030, USA
Received 2024 May 15; revised 2024 June 14; accepted 2024 June 19; published 2024 September 30

Abstract

Sample return capsules (SRCs) entering Earth's atmosphere at hypervelocity from interplanetary space are a valuable resource for studying meteor phenomena. The 2023 September 24 arrival of the Origins, Spectral Interpretation, Resource Identification, and Security-Regolith Explorer SRC provided an unprecedented chance for geophysical observations of a well-characterized source with known parameters, including timing and trajectory. A collaborative effort involving researchers from 16 institutions executed a carefully planned geophysical observational campaign at strategically chosen locations, deploying over 400 ground-based sensors encompassing infrasound, seismic, distributed acoustic sensing, and Global Positioning System technologies. Additionally, balloons equipped with infrasound sensors were launched to capture signals at higher altitudes. This campaign (the largest of its kind so far) yielded a wealth of invaluable data anticipated to fuel scientific inquiry for years to come. The success of the observational campaign is evidenced by the near-universal detection of signals across instruments, both proximal and distal. This paper presents a comprehensive overview of the collective scientific effort,

field deployment, and preliminary findings. The early findings have the potential to inform future space missions and terrestrial campaigns, contributing to our understanding of meteoroid interactions with planetary atmospheres. Furthermore, the data set collected during this campaign will improve entry and propagation models and augment the study of atmospheric dynamics and shock phenomena generated by meteoroids and similar sources.

Unified Astronomy Thesaurus concepts: Meteors (1041); Meteoroids (1040); Solar system (1528); Planetary atmospheres (1244); Planetary science (1255); Remote sensing (2191)

Materials only available in the online version of record: machine-readable tables

1. Introduction

Geophysical sensing of objects entering planetary atmospheres and surfaces is of immense importance for understanding impact-induced physical processes on Earth and beyond. Interplanetary space is teeming with meteoroids, asteroids, and comets (e.g., Belton 2004; Chapman 2008) and is sometimes even visited by objects originating from beyond our solar system, such as 1I/'Oumuamua (Meech et al. 2017). While the rate of large, extremely energetic and planet-altering impacts has largely dissipated over time since the Late Heavy Bombardment, smaller impacts continue to happen on Earth and elsewhere. For example, the lunar surface is frequently impacted by objects large enough to produce light emissions visible from Earth (e.g., Ortiz et al. 2006, 2015; Avdellidou & Vaubaillon 2019). Moreover, bright flashes seen in the atmosphere of Venus have been attributed to meteoroids (Blaske et al. 2023). On Mars, freshly formed impact craters have been found (Posiolova et al. 2022; Daubar et al. 2023), and possible seismic and acoustic wave signatures from meteoroid entries were detected by NASA's InSight lander (Garcia et al. 2022).

Unfortunately, it is profoundly difficult to predict impacts of meter-sized and larger objects with sufficient temporal and spatial accuracy and with long enough advance notice to allow comprehensive observational campaign planning. Thus, it is nearly impossible and prohibitively costly to mount a comprehensive observational campaign using a full range of sensing modalities. Therefore, virtually all observations are incidental—instruments either passively "wait" for an event to happen over a certain region (e.g., Devillepoix et al. 2020) or make a detection as a by-product of a completely different observational mission (e.g., Jenniskens et al. 2018). While small meteoroids are numerous, objects in a meter-size range are significantly more scarce and thus profoundly more difficult to capture with a multitude of instruments. Even if detailed observations take place, source characterization does not come without its own challenges. Impeding factors include incomplete ground truth, inability to directly measure and sample the object, lack of comparable events (no two natural objects are alike), limitations in models and theoretical considerations, and other uncertainties (Silber 2024).

Therefore, it is imperative to make use of well-characterized artificial objects that can serve as natural meteoroid/asteroid analogs (e.g., ReVelle et al. 2005). Ideal candidates are space mission sample return capsules (SRCs) that reenter from interplanetary space and thus achieve speeds that match those of (slow) natural meteors ($>11\,\mathrm{km\,s^{-1}}$). Their speed is also relatively close to the mean speed of natural asteroid entries ($25–30\,\mathrm{km\,s^{-1}}$; Janches et al. 2006). Only five sample return missions have reentered from interplanetary space since the end of the Apollo era: Genesis (ReVelle et al. 2005), Stardust (ReVelle & Edwards 2007), Hayabusa 1 (Ishihara & Hiramatsu 2012), Hayabusa 2 (Sansom et al. 2022), and Origins, Spectral Interpretation, Resource Identification, and Security-Regolith Explorer (OSIRIS-REx; Silber et al. 2023a; Fernando et al. 2024). All five were detected by dedicated geophysical instruments (infrasound or/and seismic; see Silber et al. 2023a for details).

To understand the relevance and application of artificial objects, such as SRCs, toward the study of larger meteoroid dynamics in the planetary atmospheres, we start with a brief overview of meteor phenomena.

Approximately 10^5 tons $\mathrm{yr^{-1}}$ of extraterrestrial material enter Earth's atmosphere, ranging in size from dust particles to meters (Plane 2012). Most particles peak in diameters around 2×10^{-4} m (Kalashnikova et al. 2000; Plane 2012), with only an extremely small fraction corresponding to meter-sized and larger objects (Drolshagen et al. 2017; Moorhead et al. 2017). Typical entry speeds are $11.2–72.8\,\mathrm{km\,s^{-1}}$ for objects originating in the solar system (Ceplecha et al. 1998). Speeds greater than $\sim 73\,\mathrm{km\,s^{-1}}$ correspond to objects visiting from interstellar space, although some exceptions around that velocity have been noted (Peña-Asensio et al. 2024). Asteroids ($\geqslant 1$ m in diameter) and meteoroids (<1 m in diameter), through their collisions with local atmosphere and subsequent ablation, produce a light phenomenon known as a meteor or a shooting star (Ceplecha et al. 1998). Very bright meteors are known as fireballs (brighter than Venus, magnitude -4) and bolides (brighter than magnitude -14; Belton 2004), and exceptionally bright events (exceeding magnitude -20) are known as superbolides (Ceplecha et al. 1998).

Of particular interest to the scientific and planetary defense communities are the asteroids and a subset of sufficiently large and fast meteoroids that produce shock waves upon entering the upper regions of the atmosphere (Tsikulin 1970; Bronshten 1983; Ceplecha et al. 1998; Silber et al. 2018). Specifically, the shock waves can lead to formation of secondary physical phenomena, from low-frequency acoustic waves and seismic shaking (e.g., ReVelle 1974; Ceplecha et al. 1998; Evers & Haak 2003; Ishihara et al. 2004; Arrowsmith et al. 2007, 2008a; Caudron et al. 2016; Silber & Brown 2019; Pilger et al. 2020) to ionospheric disturbances (e.g., Yang et al. 2014; Perevalova et al. 2015; Luo et al. 2020). When recorded by geophysical instruments, the signatures of these phenomena can be analyzed to infer physical properties and characteristics of the emitting source (e.g., ReVelle 1976). Smaller meteoroids with diameters 0.1–10 cm, while still capable of generating shock waves, are not of interest in this study, as in most cases these completely ablate at altitudes between $\sim$70 and 100 km (Ceplecha et al. 1998; Silber & Brown 2014).

Large objects can penetrate deep into the atmosphere, depositing a tremendous amount of energy at mid- and low altitudes (typically below 50 km), and sometimes their fragments may reach the surface as meteorites. A recent example is the Chelyabinsk superbolide, whose arrival caught the

scientific community by surprise. The Chelyabinsk impactor was ∼18 m in diameter, and it deposited energy of approximately 500 kt of TNT equivalent (1 TNT = 1.484×10^{12} J), leaving a wake of destruction beneath its path (Brown et al. 2013; Popova et al. 2013).

SRCs can serve as reasonable analogs for meter-sized objects that are generally studied using a variety of sensing modalities, including ground-based (e.g., optical (e.g., Devillepoix et al. 2020), radar (e.g., Janches et al. 2006), infrasound (e.g., Silber & Brown 2014), seismic (e.g., Edwards et al. 2008), and space-based instruments (e.g., US government sensors, Brown et al. 2002; Geostationary Lightning Mapper, Jenniskens et al. 2018). In this paper, we place an emphasis on geophysical observations that include infrasound (ground-based and airborne), acoustic (audible), seismic, distributed acoustic sensing (DAS), and Global Positioning System (GPS). We will outline the function of these in Section 2.

We present multimodal observations of the OSIRIS-REx reentry, the largest geophysical observational campaign of a controlled reentry ever conducted. Multimodal, large-scale observational campaigns of reentry and similar phenomena with well-known ground truth require careful planning, coordination, and execution. There is also only one chance to get it right—the object's reentry cannot be delayed or modified to meet the observation campaign's needs. Given that this was an enormous undertaking that involved many scientists from over a dozen institutions, we felt that it was pertinent to consolidate our efforts into a single publication that will provide a complete contextual picture of the campaign and serve as a scientific reference for data types and sources, for study replication, and for building on this work by others. Furthermore, campaigns like this one provide an unparalleled learning opportunity for future "one-shot" terrestrial and space exploration missions.

This paper is organized as follows: In Section 2, we give a brief background on geophysical sensing modalities. In Section 3, we outline a primer on meteor-generated shock waves and how they can be detected by geophysical instruments. The OSIRIS-REx reentry is presented in Section 4. In Section 5, we describe the institutional involvement and the geographical context. In Section 6, we describe the field deployment effort and various instruments used. In Section 7, we present the preliminary results. In Section 8, we outline our conclusions and path forward.

2. A Brief Primer on Geophysical Sensing Modalities

Infrasound is defined as sound waves below the limit of human hearing (<20 Hz). Infrasound sensing finds widespread utility in monitoring natural phenomena such as volcanic eruptions (e.g., Matoza et al. 2019), earthquakes (e.g., Arrowsmith et al. 2011), and meteorological events (Stopa et al. 2012). Additionally, it serves as a critical tool for detecting and characterizing anthropogenic activities, including explosions (e.g., Mutschlecner & Whitaker 2006; Arrowsmith et al. 2008b; Obenberger et al. 2022) and rockets (e.g., Balachandran & Donn 1971; Pilger et al. 2021). Infrasound monitoring also supports efforts in nuclear test ban verification (Brachet et al. 2010). The most typical instruments include ground-based sensors. These can be permanent or temporary installations. The latter are useful for short-term observational campaigns. In recent years, there has been an emergence of balloon-borne infrasound sensing (Bowman & Albert 2018; Silber et al. 2023b), which has opened new avenues for detection and characterization of ground and elevated infrasound sources and for validation of theoretical predictions (Albert et al. 2023). Balloon-borne infrasound has been proposed as a feasible mode of exploration for planets with thick atmospheres where other sensing modalities either are not possible or are exceedingly more costly (Krishnamoorthy & Bowman 2023). Balloons also offer a unique vantage point, away from heavy tropospheric noise, and in a presumably quieter region of the atmosphere (Krishnamoorthy et al. 2020). There have been successful detections of high-altitude and ground-based phenomena on balloons, including rocket launches, atmospheric explosions, chemical explosions, storms, and gravity waves (Bowman & Lees 2018; Albert et al. 2023). While bolide detection by a balloon-borne infrasound sensor has never been confirmed, it is expected that these platforms would readily detect a bolide should one occur in the vicinity.

Much of seismic analysis involves observing and modeling the wavefields generated from sources interior to or on the surface of Earth. Earthquakes, volcanic disturbances, chemical and nuclear explosions, and artificial energy sources such as vibration-producing trucks or even handheld hammer blows can provide seismic wavefields that can be modeled to determine the physical characteristics of Earth over scales from meters to 10,000 km. Impulsive atmospheric sources such as explosions (e.g., Matoza et al. 2022), bolide sonic booms (Le Pichon et al. 2002; Langston 2004; D'Auria et al. 2006), or even thunder (Lin & Langston 2009a, 2009b) can be interesting in their own right, as well as providing for new wavefields for investigating Earth structure using records from seismometers.

DAS systems are a rapidly emerging technology that provide spatially dense (∼1–10 m), extensive (tens of kilometers), and high-fidelity seismic measurements by sensing with fiber-optic cables (e.g., Hartog 2017). Previous studies have demonstrated that DAS can capture a variety of seismoacoustic signals, including seismic waves from earthquakes and explosions (e.g., Lindsey et al. 2017; Fang et al. 2020), and meteorites (Vera Rodriguez et al. 2023). While seismometers and infrasound sensors have been employed to measure signals from spacecraft reentry events prior to the OSIRIS-REx SRC (e.g., ReVelle & Edwards 2007; Edwards et al. 2007), the OSIRIS-REx event is the first instance of DAS deployment to record a reentry. Similarly, while DAS has not yet been deployed in extraterrestrial settings, data returned from seismometers and/or infrasound sensors have provided information about the seismic activity and structure of the Moon and Mars (e.g., Giardini et al. 2020; Lognonné et al. 2020; Nunn et al. 2020) and the atmosphere of Mars (e.g., Banfield et al. 2020; Ortiz et al. 2022).

Energetic and explosive events near Earth are well-known to produce acoustic (compression) waves that propagate upward and outward into the atmosphere. When these acoustic waves propagate upward into the ionosphere, they couple with ionospheric plasma, producing electron density fluctuations (Miller et al. 1986; Forbes & Roble 1990). Wave periods generated by these events range from 2 to 16 minutes, with ground-level speeds between 300 and 400 m s^{-1}. Speeds dramatically increase with altitude above the mesosphere owing to changes in density and increases in background thermosphere temperatures. At altitudes near peak electron density (250–400 km), speeds can range from 700 to 900 m s^{-1}. In all, it takes approximately 8–10 minutes for the wave generated at Earth's surface to propagate to these altitudes.

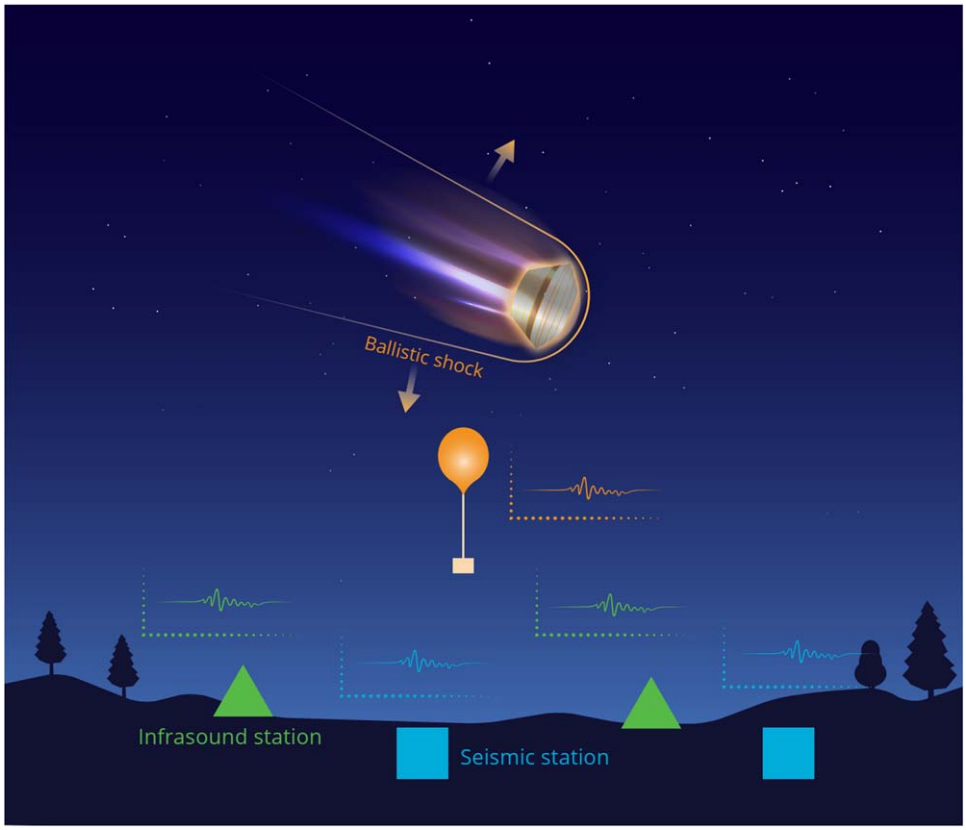

Figure 1. Diagram showing the shock wave generated by an SRC (analog to meteoroids) as it travels through the atmosphere. Ground-based infrasound and seismic instruments and airborne infrasound instruments could detect the shock waves depending on circumstances. Diagram not to scale. Diagram does not include all possible sensing modalities that might be used in geophysical observations of reentry.

These waves create electron density perturbation signals that are probed remotely, such as using electromagnetic instruments. Impulsive events like meteors (e.g., Yang et al. 2014; Perevalova et al. 2015; Luo et al. 2020), volcanic eruptions (e.g., Shimada et al. 1990), earthquakes (e.g., Otsuka et al. 2006), tsunamis (e.g., Blewitt et al. 2009), rocket launches (e.g., Afraimovich et al. 2001), and ground explosions (e.g., Fitzgerald 1997) have been examined using these methods. Here we are interested in examining the effects of the shock wave generated by the hypersonic OSIRIS-REx SRC reentry and how it might affect the ionosphere and signals used to probe it. We employ GPS *L*-band signals, which are frequently used to probe the ionosphere, but signatures often suffer a delay of 1–30 minutes before they impact the ionosphere and can be detected.

3. Meteor-generated Shock Waves

In this section, we offer a concise overview of meteor-generated shock waves and their correlation with acoustic and, on occasion, seismic waves (e.g., Edwards et al. 2008; Silber & Brown 2019). We also briefly outline the similarities between shock waves generated by natural objects and their artificial analogs (Figure 1).

In principle, the mechanisms governing meteor-generated shock waves are broadly relevant to artificial hypersonic analogs (and vice versa), including space mission reentries, rendering them valuable proxies for investigating meteor phenomena (ReVelle et al. 2005; Silber et al. 2023a).

When a meteoroid (or an asteroid) reaches the continuum flow regime as it descends through Earth's exponentially denser atmosphere at hypervelocity, it generates a shock wave (Krehl 2011; Silber et al. 2018 and references therein). Meteoroids travel at extremely high Mach numbers, from 35 to 240. Mach number (M) is the ratio of the meteoroid speed and the local speed of sound. At such speeds, the Mach cone angle (outlining the adiabatically expanding ablational flow field) is small enough that the shock front can be approximated as a cylinder, therefore forming the so-called cylindrical line source (Plooster 1970; ReVelle 1976). The shock travels ballistically, or perpendicularly to the meteoroid flight trajectory, and energy is deposited into the surrounding atmosphere as a function of path length. It is important to note that the fundamental difference in shock waves between the large meteoroids/asteroids and artificial analogs is the fact that the shock waves generated by natural objects are ablationally amplified, while objects such as SRCs have a very limited ablation rate. Another key difference is the significantly higher magnitude and intensity of the hyperthermally driven chemical reactions in the ablationally amplified meteor/asteroid flow field, which ultimately affects the strength of a shock wave. Moreover, meteoroids and asteroids frequently experience fragmentation, which can occur in the form of continuous fragmentation, gross fragmentation, or some combination of the two (e.g., Trigo-Rodríguez et al. 2021; Silber 2024). In such cases, the shock wave is no longer generated by the object's hypersonic passage alone, but it also includes the shock with quasi-spherical or spherical geometry (also known as point source). The SRCs do not include such a point-source component, allowing the hypersonic shock wave to be studied without interference from such signals.

The blast radius (R_0) represents the volume of a region containing superheated adiabatically expanding plasma in the flow field immediately behind the shock front, where highly nonlinear processes take place. The mathematical expression is $R_0 = (E_0/p_0)^{0.5}$, where E_0 is the energy per unit length and p_0 is the ambient pressure. Assuming no fragmentation, the blast radius can be approximated as $R_0 \sim Md_m$, where M is the Mach number and d_m is the meteoroid diameter. It is generally accepted that beyond approximately $10R_0$ the shock decays to a weak shock regime, and at some point to a linear acoustic wave (Plooster 1970; Tsikulin 1970; ReVelle 1976). A comprehensive review of meteor-generated shock waves can be found in Silber et al. (2018), and a review on meteor-generated infrasound can be found in Silber & Brown (2019).

Shock waves generated by hypersonic passage of meteoroids (and other impulsive sources) ultimately decay to infrasound, which has the remarkable ability to propagate over vast distances with minimal attenuation (Evans et al. 1972). At a very close range from the source, the acoustic wave might have both inaudible and audible components. A familiar example of the audible component would be a sonic boom generated by a jet when it breaks the sound barrier. The 1908 Tunguska airburst was the first documented bolide-generated infrasound (Whipple 1930), followed by a dozen or so events during the 1960s and the 1970s (Revelle 1997; Silber et al. 2009). Since the inception of the Comprehensive Nuclear-Test-Ban Treaty in the mid-1990s (Brachet et al. 2010), infrasound has gained momentum as a vital sensing modality used toward global detection of large bolides (e.g., Pilger et al. 2015, 2020).

In some instances, infrasound might have enough energy to induce seismic waves, known as air-coupled or atmospheric seismic waves, which can be detected by seismometers and other seismic monitoring instruments (Edwards et al. 2008). The characteristics of these seismic waves, such as their amplitude, frequency, and arrival time, can provide valuable information about the source. It is important to note that while bolide sonic booms can induce seismic waves, the seismic signals produced are typically much weaker and shorter-lived compared to those generated by earthquakes or other large-scale seismic events (e.g., impacts). There are three modes of coupling: (1) direct coupling (the incident acoustic wave induces ground motion), (2) precursory (generated by the infrasound wave impacting the ground at specific incidence angles that allow resonant coupling to subsurface seismic propagation modes that then travel independently to the recording station), and (3) impact (surface and body waves generated when a fragment of a meteoroid hits the surface; see Cumming 1989; Edwards et al. 2008).

4. OSIRIS-REx and Geophysical Observation Considerations

Controlled and well-characterized reentries from interplanetary space at velocities exceeding 11 km s^{-1} are exceptionally rare. Only five such reentries have taken place since the end of the Apollo era, with the most recent one being OSIRIS-REx in 2023 September (Silber et al. 2023a). Prior to that, Genesis landed in 2004 (ReVelle et al. 2005), Stardust in 2008 (ReVelle & Edwards 2007), Hayabusa 1 in 2010 (Fujita et al. 2011; Watanabe et al. 2011; Yamamoto et al. 2011), and Hayabusa 2 in 2020 (Sarli & Tsuda 2017; Nishikawa et al. 2022; Sansom et al. 2022; Yamada & Yoshihara 2022). The physical parameters for the five SRCs are listed in Silber et al. (2023a). Both Genesis and Stardust landed in the United States, and their signals were detected by instruments installed at the West Wendover Airport in Utah (ReVelle et al. 2005; ReVelle & Edwards 2007). Genesis was detected via infrasound, and the acoustic signatures generated by the last three were recorded by both infrasound and seismic instruments. A review describing seismoacoustic detections of these four reentries is given by Silber et al. (2023a), and we therefore keep the discussion to a minimum.

The OSIRIS-REx space mission was designed to collect samples of the near-Earth asteroid Bennu and bring those particles to Earth for analysis (Ajluni et al. 2015; Beshore et al. 2015; Lauretta et al. 2017). This was the first asteroid sample collection mission for the United States. On 2023 September 24, the SRC separated from the main craft and entered the atmosphere at a very shallow angle (nearly horizontal). The SRC is 81 cm wide and has a mass of ∼46 kg. The atmospheric interface was at an altitude of 125 km above a point close to San Francisco, California (14:42 UTC, 8:42 MDT). After a few minutes of flight, it safely touched down on the Department of Defense's Utah Test and Training Range (UTTR) at a speed of 5 m s^{-1} (18 km h^{-1}), slightly faster than originally anticipated (Gran 2023). The reentry consisted of several flight phases, including hypersonic, transonic, and dark flight (see Silber et al. 2023a for further details). The drogue parachute was supposed to open at an altitude of ∼30.4 km to slow down and stabilize the SRC before the main parachute sequence, but it failed as a result of faulty wiring (Francis et al. 2024). When the main parachute opened at 2.74 km altitude, the drogue was also released, but because it was already cut loose, it flew off. The main parachute managed to sufficiently slow the SRC down, facilitating soft landing at 14:52 UTC, a minute earlier than planned (Gran 2023; Francis et al. 2024).

The SRC return of the OSIRIS-REx mission offered a rare opportunity to record both the incident atmospheric pressure field of the incoming Mach cone at the ground surface and induced seismic motions near Earth's surface at a known location in time and space. Factors that are important in deducing the effects of the acoustic−seismic interaction at the ground surface include obtaining basic knowledge about the incident wavefield, such as its horizontal slowness and azimuth of approach (Lin & Langston 2009a). It is a testament to the accuracy of NASA orbital dynamics that the trajectory and arrival time of the returning capsule could be controlled for a landing in western Utah. However, the exact behavior of the expanding Mach cone and how it interacts with a particular place on the ground depend on not only the precise path geometry but atmospheric winds that can cause lateral variations in sound speed, distorting the acoustic wave front on its descent from the upper atmosphere. In principle, the horizontal phase velocity of the downgoing acoustic wave could vary from infinite velocity (vertical incidence) to approximately 0.33 km s^{-1} for near-horizontal wave propagation. Conversion of the atmospheric acoustic wave into propagating P and S body waves or Rayleigh waves will strongly depend on the local wave slowness. Directional attributes, such as particle motion, will also depend on wave azimuth of approach.

The nominal trajectory, based on the entry, descent, and landing (EDL) simulations (Francis et al. 2024), was provided by NASA (M. Moreau, personal communication); the ground track is shown in Figure 2. The color represents the altitude. The peak heating, dynamic pressure, and Mach number as a

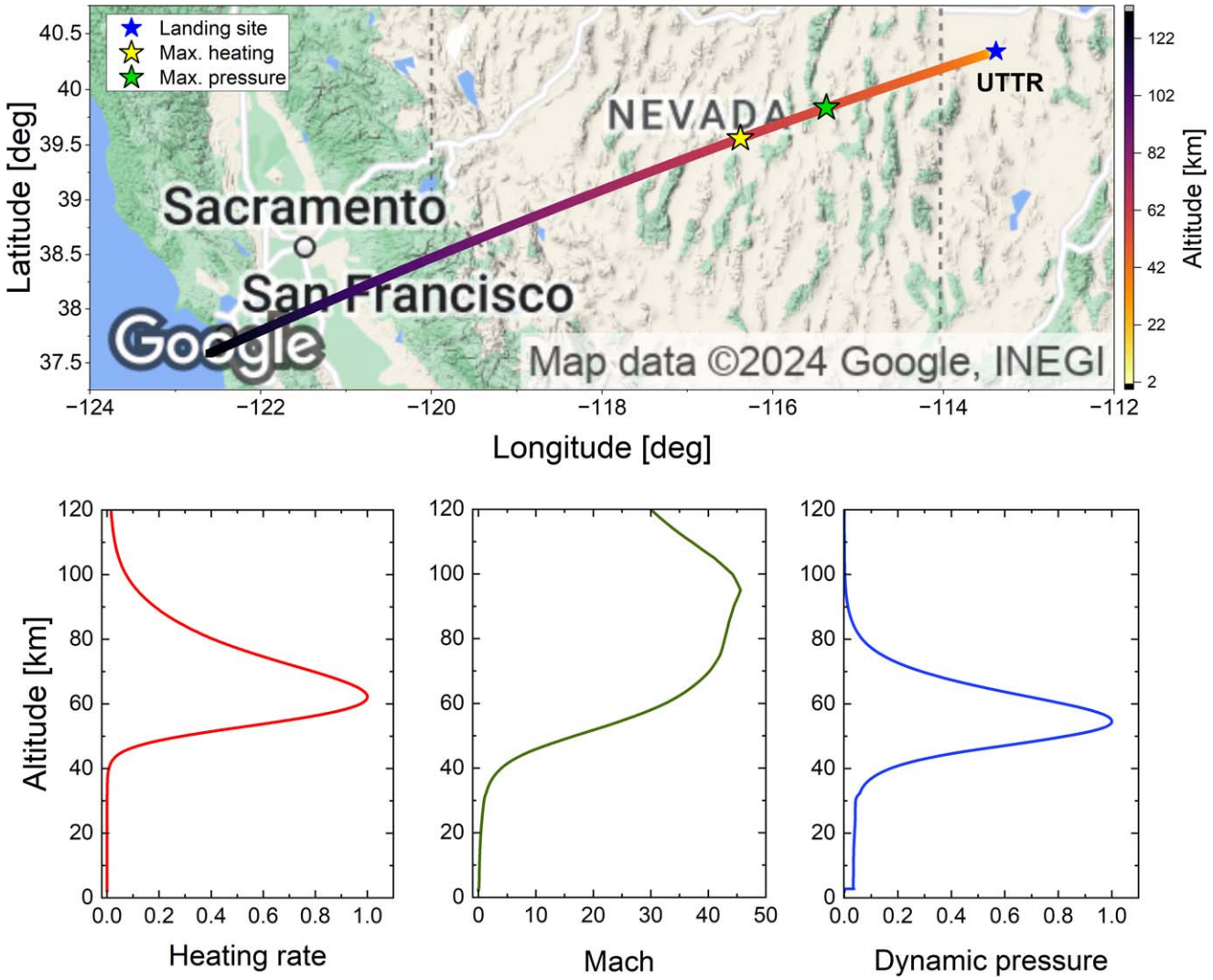

Figure 2. Top panel: OSIRIS-REx ground track. Yellow and green stars show the points of maximum heating and maximum dynamic pressure, respectively. The landing site is indicated with a blue star. Bottom panels: the normalized heating rate, Mach number, and normalized dynamic pressure as a function of altitude (left to right). Trajectory data are courtesy of NASA.

function of altitude are also shown in Figure 2. We note that any trajectory-related values (geographical coordinates, altitudes, peak heating, dynamic pressure, and Mach number) presented here correspond to the nominal trajectory (Francis et al. 2024) that was released by NASA before the OSIRIS-REx reentry, and it therefore may not accurately represent the real-time reentry trajectory. However, it is expected that the two would be in very close agreement.

One significant distinction between reentry phenomena and conventional controlled experiments, such as static sources (e.g., chemical explosions) or sources with constrained lateral movement at mid- and low altitudes (e.g., rocket launches), is the extensive geographical area (Figure 2) covered and the multitude of potential observation points available to capture the dynamic changes occurring along the trajectory. Consequently, selecting the most relevant regions of interest becomes pivotal to ensure the acquisition of high-fidelity data. Although permanent infrasound and seismic stations are established throughout the United States, the immediate vicinity beneath and adjacent to the trajectory lacks sufficient geophysical instrumentation to reliably capture signals with a high degree of certainty. While incidental detections remain plausible, there exists uncertainty regarding the likelihood of signal recording. This uncertainty stems from the fact that the altitude of the SRC could be too elevated or the SRC ground track could be at a considerable distance from the existing permanent instrument installations. Given the infrequency of reentry events from interplanetary space, relying solely on distant instruments to gather data entails substantial risk. Therefore, systematic planning of a dedicated observational campaign is imperative.

Our geophysical observational campaign was carefully planned to maximize the scientific output and ensure the highest chance of success while considering various intrinsic and extrinsic factors. These include, but are not limited to, the following:

i. Signal detection and data collection locations (e.g., identify locations through research and analysis where signals related to the reentry are most likely to be detected; consider factors such as geological features, topography, and historical data on similar events to pinpoint optimal observation sites and prioritize locations that are accessible for instrumentation setup and maintenance; evaluate the

potential for multiple observation points to capture different aspects of the reentry and enhance data coverage).

ii. Cost considerations (e.g., develop a budget that accounts for all expenses associated with the campaign, including personnel salaries, fieldwork costs, equipment procurement and maintenance, logistics, and administrative expenses; allocate resources strategically to ensure the campaign's financial viability and explore cost-saving measures such as optimizing logistical arrangements to minimize expenses without compromising scientific objectives).

iii. Instrument synergy and deployment (e.g., assess the compatibility and capabilities of different instrumentation options to ensure that they complement each other and provide comprehensive data coverage; consider factors such as instrument reliability, data transmission capabilities, and power requirements when selecting deployment locations and configurations; implement contingency plans and redundancy measures to mitigate the risk of instrument failure and ensure continuous data collection throughout the campaign).

iv. Environmental and infrastructure impact (e.g., conduct environmental risk assessments to identify potential safety hazards associated with fieldwork activities, such as exposure to extreme temperatures, rough terrain, or wildlife encounters; engage with relevant stakeholders, regulatory bodies, and environmental agencies to obtain permits and approvals for fieldwork activities; implement mitigation measures to minimize environmental disruption, such as site restoration efforts and adherence to best practices for minimizing habitat disturbance; coordinate with landowners, facility managers, and infrastructure operators to ensure minimal interference with existing infrastructure and facilities).

v. Personnel allocation (e.g., define roles and responsibilities for scientific and technical staff, students, and collaborators involved in the campaign and provide specialized training to personnel on wilderness safety, navigation techniques, and emergency first aid to enhance their ability to respond to safety incidents in remote locations; foster a collaborative and inclusive work environment that encourages communication, teamwork, and knowledge sharing among team members; prioritize the inclusion of personnel with a cardiopulmonary resuscitation certification and wilderness knowledge in field teams to oversee safety protocols and emergency response procedures; establish clear lines of communication and designated safety officers within field teams to facilitate coordination and decision-making in emergency situations).

vi. Timeline and coordination (e.g., schedule safety briefings and training sessions to reinforce safety protocols and address any emerging safety concerns; establish communication protocols for reporting safety incidents or concerns, including designated channels for contacting emergency services and obtaining assistance; incorporate safety checkpoints into the campaign timeline to review safety procedures, assess risks, and adjust plans as necessary to ensure the ongoing safety of all personnel involved).

With respect to the most optimal observational point, the region beneath the peak heating point would be of primary interest since the energy deposition would be the greatest and the signals would be the strongest. The peak heating was projected to take place over Eureka, Nevada, a small town along US Route 50, known as "the loneliest road in America." Therefore, this region was deemed to be ideal for emplacement of geophysical instruments to best capture the signals from OSIRIS-REx. At the coordinates corresponding to the peak heating (39.5585N, −116.3852E, altitude 62.1 km), the dynamic pressure was predicted to be 69% of the maximum. The SRC was estimated to be traveling at Mach 34.8. At this speed the Mach cone angle is only 1°.65. Thus, for the purposes of modeling and signal prediction, the shock can be approximated as a cylindrical line source (Figure 1), traveling ballistically relative to the path of the object (ReVelle 1976; Silber & Brown 2019). Consequently, emplacing some number of instruments roughly perpendicular to the trajectory would theoretically capture the shock decay as a function of distance. Moreover, emplacing instruments in several locations beneath and roughly parallel to the trajectory would theoretically capture signals generated at different parts of the trail and aid in studying the signal characteristics as a function of altitude and other factors (e.g., velocity, atmospheric specifications).

Another region of scientific interest from the observational standpoint would be the trajectory segment related to the SRC deceleration and the flight regime change from hypersonic to supersonic and finally subsonic. The lower altitude of the SRC would ideally provide ample opportunity for the signals to be detected by geophysical instruments. The maximum dynamic pressure was predicted to occur at an altitude of 54.5 km (39.8365N, −115.3717E). Here the heating would have decreased to 66% of the maximum. In the case of OSIRIS-REx, this is just beyond the Nevada−Utah state line. For reference, the West Wendover Airport in Utah is due north.

The highest Mach achieved by the SRC was 45.6, at 95 km altitude (38.5178N, −119.8486E). Here the heating rate was estimated at only 11% of the maximum achieved and dynamic pressure at ∼0.5% of the maximum. Based on the available parameters, the onset of the shock wave is estimated to occur at an altitude of ∼80 km (or slightly higher). The shock wave, as soon as it forms, would also produce infrasound. It would be scientifically interesting to attempt to capture the shock wave as it forms at these altitudes. However, considering that the SRC is at a high altitude and the energy deposition is much lower than at the peak heating point, such an endeavor would carry a high risk of nondetection. Therefore, our observational campaign focused on the geographic region spanning from slightly west of Eureka, Nevada (roughly the peak heating point), toward east, in the area relatively close to the landing site (Figure 2).

5. Institutional Engagement and Site Selections

5.1. Institutional Engagement

Approximately 80 investigators from over a dozen institutions participated in this historical observational campaign. The primary participating institutions were Sandia National Laboratories (SNL), Los Alamos National Laboratory (LANL), NASA Jet Propulsion Laboratory (JPL), Air Force Research Laboratory (AFRL), Atomic Weapons Establishment (AWE) Blacknest, Boise State University (BSU), Defense Threat Reduction Agency (DTRA), Idaho National Laboratory (INL), Johns Hopkins University (JHU), Kochi University of Technology (KUT), Nevada National Security Site (NNSS),

Table 1
List of Institutions That Deployed Instruments in the Various Regions

West Region			East Region		Distal Region
Eureka Airport	Newark Valley	Bean Flat Rest Area	West Wendover Airport	NV/UT	All Sites
SNL, LANL, UM, SMU, KUT, TDA, JPL, AFRL	SNL, LANL	JHU	OSU, UH	UH, AFRL, INL	LANL, AWE, BSU, NNSS

Oklahoma State University (OSU), Southern Methodist University (SMU), TDA Research Inc. (TDA), University of Hawaii (UH), and University of Memphis (UM). For brevity, affiliations of those who were involved and/or contributed through primary institutions (e.g., student exchange, internships, second-level collaboration, and similar means) are stated at the front of the paper but not reiterated here.

To keep focus on the scientific aspect of the campaign, the main text might not always differentiate who did what unless contextually necessary. While each team had their own scientific objectives, the entire multi-institutional group collaborated toward the common goal of gathering high-fidelity data. In the remainder of this section, we first describe the geographical context, followed by ground-based observations, and conclude with balloon-borne observations. We also include the appendices and supplemental materials with additional pertinent information, which we will refer to throughout the main text.

5.2. Geographical Context

5.2.1. West Region: Eureka, Nevada

Two primary locations were selected as deployment sites in the region of Eureka, Nevada: Eureka Municipal Airport (EUE; 39.6039N, −116.0036E) and the Newark Valley (centered at 39.6833N, −115.7217E). EUE was selected because it was situated almost directly beneath the OSIRIS-REx reentry path, was access controlled, and had large areas of pavement for equipment layout. Moreover, for balloon deployment, trajectory calculations using weather model outputs from previous years indicated that the balloons would most likely remain close to the reentry path if launched from the EUE. Finally, there were very few other suitable sites in the area for multiple balloon releases. The town of Eureka graciously allowed us to use the airport. The Newark Valley was selected because it is traversed by Strawberry Road, which is not traffic heavy, passes through large plots of land owned by the Bureau of Land Management (BLM), and, most importantly, runs north to south, with a section situated directly beneath the nominal reentry trajectory. This is ideal for configuring a transect with instrument installations perpendicular to the nominal trajectory. Permits or confirmation of casual use compliance were obtained from BLM to install infrasound and seismic sensors, as well as DAS. Bean Flat Rest Area (BFRA) was an additional location (39.4996N, −116.5095E), farther west and very close to the point of peak heating, that was selected for seismic instrument installations. The list of institutions that deployed instruments in the West Region is shown in Table 1. The map is shown in Figure 3.

5.2.2. East Region: Utah–Nevada

The East Region included several locations, chosen because of their proximity to the nominal reentry trajectory and the ease of access. These included the Nevada−Utah state line, West Wendover Airport (ENV) in Utah, and two locations east of the UTTR. The area around the Nevada−Utah state line (centered around 40.201N, −114.047E) was selected because of accessibility and the BLM landownership. Importantly, on the Utah side, just beyond the Nevada−Utah state line (centered around 40.1738N, −113.9960E), there is a local road (North Ibapah Road) that runs approximately north–south beneath the nominal reentry trajectory. On the Nevada side, US Route 93 runs from the nominal trajectory and north up to ENV (the halfway point is approximately at 40.4773N, −114.1555E). ENV (40.7280N, −114.0212E) was previously utilized in observing the reentry of Genesis and Stardust, although their nominal trajectories were significantly closer than that of OSIRIS-REx. Preliminary propagation modeling and hypersonic carpet prediction modeling using averaged atmospheric specifications and winds from previous years showed that signals generated by the OSIRIS-REx SRC would be received at ENV. The airport offered a secure large space that would allow sensor setup without any tampering. Two other locations east of the UTTR were selected, one north of Dugway, Utah (40.2571N, −112.7404E), and the other in Clive, Utah (40.7089N, −113.1167E). Dugway is ∼63 km east and Clive is ∼52 km northeast from the nominal landing site. See Table 1 for institutions that deployed in the East Region. The map is shown in Figure 3.

5.2.3. Distal Region

Distal Region stations consisted of permanent infrasound array stations, which were part of larger networks and wider trial series, as well as dedicated stations that were installed for the purpose of detecting the OSIRIS-REx SRC reentry. These stations were situated in several areas east (Price, Utah), north (Boise, Idaho), and south (St. George, Utah, and NNSS, Nevada) of the SRC's nominal trajectory, and at distances ranging from ∼250 to ∼400 km. The list of institutions that operated these infrasound assets is shown in Table 1.

6. Instruments and Deployment

The team deployed over 400 sensors combined among all participating institutions, marking the most instrumented reentry in history. For clarity, we present instruments and describe field deployments by instrument type (infrasound, seismic, etc.). Additional deployment photographs and the initial results that could not be included in the main text are presented in Appendix A, Figures A1–A16 and Table A1. Because it is not possible to include the particulars for that many instruments in the main text, we include the detailed list (consisting of the instrument make, the sampling rate, the geographical coordinates, and the affiliated institution) in the tables in the appendices, as follows: Table B1 (infrasound), Table C1 (seismic), and Table D1 (GPS). Our goal was to deploy instruments beneath the trajectory and perpendicular to

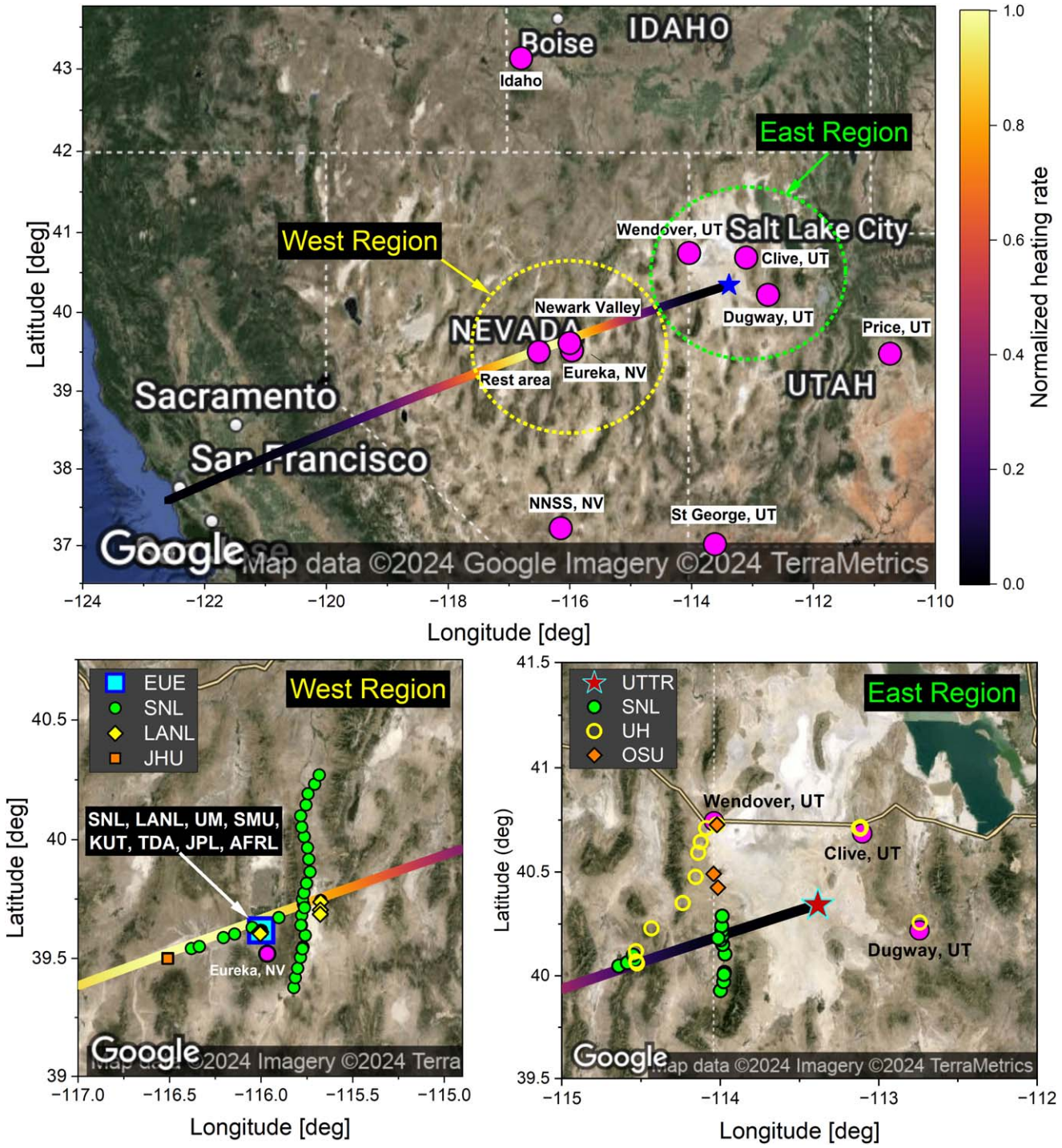

Figure 3. Top: map showing deployment regions. Areas beyond the circled areas are within the Distal Region. Bottom left: zoomed-in view of the West Region. Bottom right: zoomed-in view of the East Region. Pink circles are various landmarks (to be explained further in the text). In the West Region, most institutions deployed at EUE. Installations beyond the airport are plotted separately by institutions for the West and East Regions. Instrument type is further enumerated in Appendices B and C.

it wherever possible in order to evaluate signal characteristics as a function of the SRC flight along and away from the propagation path (see Figure 3). The numbers and type of instruments each institution deployed are shown in Table 2.

6.1. Ground-based Infrasound and Audible Acoustic

SNL deployed three four-element arrays and 47 single-sensor stations in the West and East Regions. The three infrasound arrays, deployed in the West Region, consisted of analog and digital Hyperion sensors arranged in a triangular formation. Hyperion sensors are manufactured by Hyperion Technology Group Inc. and are widely used in a variety of infrasound monitoring applications (e.g., Bowman & Albert 2018). One array was at the EUE, in the northeast corner, and the other two were in Newark Valley along Strawberry Road. We aimed to arrange the arrays into an "L", such that two arrays are positioned roughly parallel to the nominal OSIRIS-REx trajectory

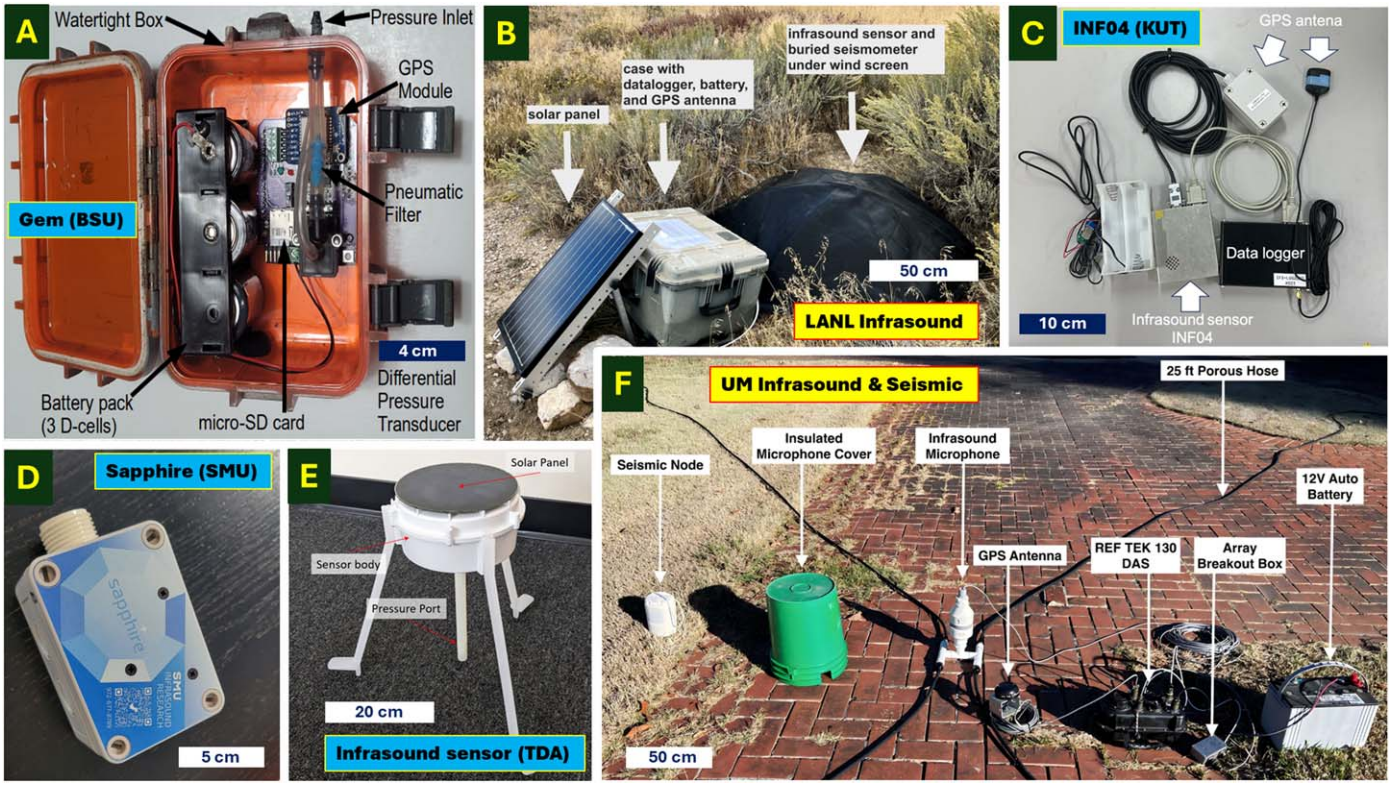

Figure 4. Representative examples of infrasound and seismic sensors and their field installations. (a) Gem Infrasound logger developed by BSU (photo credit: J. Anderson); (b) infrasound installation (LANL; photo credit: C. Carr); (c) INF04 infrasound sensor (KUT; photo credit: Y. Nikishawa); (d) Sapphire infrasound sensor (SMU; photo credit: E. Silber); (e) TDA's infrasound sensor (photo credit: D. Eisenberg); (f) Infrasound and seismic instruments (UM; photo credit: S. Bazargan).

Table 2
Summary of All Instruments Observing the Reentry of OSIRIS-REx

Institution	Infrasound (Single Sensor)	Infrasound (Array)	Total No. of Sensors in Arrays	Large N-array (No. of Sensors)	Audible Microphone	Smartphone	Seismic	DAS	GPS	Balloons
SNL	47	3 (x4)	12	…	…	2	19	…	…	6
LANL	6	2 (x4) + 1 (x6)	14	…	1	1	6	2	5	
AWE	…	1 (x4)	4	…	…	…	…	…	…	
BSU	…	3 (x4), 1 (x44)	56	…	…	…	…	…	…	
JHU	…	…	…	…	…	…	11	…	…	
JPL	…	…	…	…	…	…	…	…	…	2
KUT	…	1 (x4)	4	…	5	…	…	…	…	
OSU	12	1 (x4)	4	…	…	…	…	…	…	
SMU	…	1 (x4)	4	…	…	…	…	…	…	
TDA	…			114	…	…	…	…	…	
UH, AFRL, INL	…	…	…	…	…	33	…	…	…	
UM	…	2 (x4)	8	…	…	…	20 + 96	…	…	
	65	16	106	114	6	36	56	2	5	8

Note. The detailed list of instruments with geographical coordinates can be found in the appendices.

(∼10–12 km shortest path) and one is positioned perpendicular to it (∼24 km shortest path). The reasoning is that such a configuration could potentially capture the signals from different parts of the trail and help evaluate signal properties as it propagates away from the reentry path. Each array had two colocated seismic nodes. The instruments were powered by marine deep-cycle batteries and solar panels. Timing was tracked through GPS.

In addition to the three arrays, SNL and DTRA also deployed 46 single stations consisting of Gem infrasound loggers (Figure 4(a)) in various locations (30 in the West Region and 16 in the East Region). Gems (ver. 1.01) are self-contained sensor loggers optimized for deployment and maintenance in large numbers (i.e., small, lightweight, low-power consumption, cable-free, and fast deployment process; Figure 4(a); Anderson et al. 2018). They sample at 100 Hz,

with a flat response between 0.039 and 27.1 Hz and an rms self-noise of 1.55 mPa (0.5–2 Hz) and 3.9 mPa (0.1–20 Hz). Gem infrasound loggers have previously been used in campaigns using large numbers of sensors (Rosenblatt et al. 2022; Anderson et al. 2023; Scamfer & Anderson 2023), campaigns where ease of concealment was essential (Ronan 2017; Tatum et al. 2023), and airborne infrasound recording requiring a lightweight sensor (Bowman & Albert 2018; Krishnamoorthy et al. 2020; Bowman & Krishnamoorthy 2021; Silber et al. 2023b). Twenty-three Gems were installed along Strawberry Road to form a transect relative to the nominal trajectory, extending both north and south. Out of these, 11 were to the south relative to the nominal trajectory (∼44 km due south, and ∼40 km shortest distance), and 12 were to the north (∼56 km due north, and ∼51 km shortest distance). The approximate separation between stations was 5 km. The sensors were powered with batteries and portable solar panels. To reduce the adverse effect of wind noise, Gems were emplaced inside bushes, but the solar panels were left exposed. The remaining seven Gems were deployed about 3–5 km from and parallel to the nominal ground track, extending from the point of peak heating toward east, just beyond Strawberry Road. The total end-to-end distance was ∼65 km. In the East Region, SNL deployed 15 Gems. Four of these were very close to the nominal trajectory (∼1–3 km) and in the vicinity of US Route 93 Alternate (Nevada). Some ∼45 km to the east, 10 Gems were installed along the Nevada−Utah state line, forming a 41 km long transect (North Ibapah Road), with an additional Gem positioned slightly to the west to coincide with the nominal reentry path. All instruments were installed 2 days before the OSIRIS-REx reentry and removed either immediately after the reentry or the next day.

TDA Research deployed a 115-element Large N-array, colocated with SNL's infrasound array in the northeast corner of EUE, in a 100 × 100 m array. The sensors (Figure 4(e)), designed and built by TDA Research Inc., were previously tested during a controlled field experiment. This observational campaign was the second fielding, and it was the first time the sensors were used against a real-life event. TDA's sensors are low in cost and specifically designed to be networked into large and dense arrays with hundreds of sensors and to wirelessly stream data to a central computer. The array design is modular and flexible, and its size can be anywhere from 5 sensors up to 500 sensors added in groups of five. These sensors have a sensitivity of <0.1 Pa and a sampling frequency of 200 Hz (which can be increased up to 330 Hz if needed). Each sensor has an onboard battery with a battery lifetime of approximately 9 days. They also come equipped with a solar panel that will recharge a day's worth of power in 1–2 hr of sunlight and will fully recharge the sensors in 9–13 hr. They are located using a differential GPS system with accuracy of <1 cm, and clocks from all sensors in the array are synced to within 1 ms. The sensors weigh 0.703 kg each and are 33 cm tall when fully assembled. TDA's sensors minimize wind noise by sampling at only 1.3 cm off the ground, taking advantage of the ground's boundary layer to reduce effective wind speed by 75%.

There were three teams from LANL, two in the West Region (DAS/seismoacoustic and GPS; see Section 6.5) and one in the Distal Region. The DAS/seismoacoustic LANL team in the West Region deployed DAS at EUE and Newark Valley, also colocating infrasound (Figure 4(b)) and seismic sensors. Infrasound sensors (Hyperion IFS-3000) were installed at strategic locations along the DAS fiber (for complete instrumentation details, see the appendices). Additionally, at the Newark Valley site, a PCB microphone sampling at 50 kHz was deployed near the DAS interrogator setup location, and a personal iPhone was filming during the reentry.

The Distal Region LANL team (alongside AWE, BSU, and NNSS) focused on infrasound data collection at distal infrasound stations. The high speed of arrival and the known time and path made this an ideal opportunity to test LANL's shockwave propagation estimate algorithms (Blom et al. 2024). Three arrays were deployed by LANL, one in Price, Utah, one in St. George, Utah, and one on the north side of the NNSS, Nevada. These sites were chosen because an early estimate of regional infrasound arrivals indicated that they were likely to occur at these locations. The sensors deployed were Hyperion IFS-3000 infrasound sensors. Digitization was done with RefTek 130 digitizers powered by batteries that were kept charged by solar panels. These three arrays were deployed during the week prior to the reentry. There were no team activities on the day of the reentry.

At EUE, KUT deployed five microphones, as well as four infrasound sensors (SAYA INF04), the same kind as those used to observe Hayabusa 1 and Hayabusa 2 SRCs (Figure 4(c)). Hayabusa 1 was also observed with Chaparral microbarometers (Yamamoto et al. 2011; Ishihara & Hiramatsu 2012; Sansom et al. 2022). The sampling rate of SAYA INF04 was 100 Hz (using Mathematical Assist Design Lab's INFLOG 2020). These infrasound sensors were arranged to form an elongated north–south triangle array (see the appendices for sensor locations).

UM installed a four-element infrasound array at each of two subarrays of the seismic array (described in the next section) at EUE. Instruments were made by VLF Designs and are flat to pressure between 0.25 and 25 Hz. These were placed on the ground surface within a plastic bucket insulated with 10 cm rubber foam. Four porous 7.5 m hoses attach to the bottom pressure manifold of the microphone. The four elements were arranged in a triangular configuration with a central element. Elements communicated with a RefTek 130 digitizer via 30 m cables to a breakout box that routed infrasound signals to channels 1–4. Timing was through GPS. The instruments and digital acquisition system were powered by a 12 V car battery (Figure 4(f)). The rationale for having two infrasound arrays was to ensure that we could record the atmospheric pressure signal at a minimum of one position, with the other being a backup. The small-aperture (∼60 m) infrasound arrays precluded high resolution for determining the incident wave slowness and azimuth for the expected near-vertical incidence angle for the incoming N-wave. However, having four instruments in each array added an additional redundancy in measuring the incident wave pressure to compare with the test seismometer that was placed at the center of each array.

SMU deployed four lightweight portable Sapphire sensors (Figure 4(d)) at the EUE. The Sapphire is an infrasound nodal recorder developed at SMU inspired by the Gem infrasound node (Anderson et al. 2018) and similar in design (although developed independently) to the node described by den Ouden et al. (2021). The Sapphire response is reasonably flat above 0.1 s, with a sensor that is factory calibrated to 0.25% amplitude response, enabling the recorder to apply the factory calibration constant and log pressures in units of pascals, thus for most experiments avoiding the need to do instrument

corrections. The unit records continuously for about 2 weeks on four AA batteries, recording at 128 Hz with a GPS controlled clock. Although the Sapphire sensor has a higher self-noise than more expensive infrasound microphones, its low cost, good calibration, quick deployment, and small size make it convenient for many experiments that expect reasonable signal-to-noise ratio (SNR) in the 1–5 Hz band.

OSU set up their instruments at the ENV, deploying three different models of microbarometers. A four-sensor infrasonic array was formed with Chaparral Physics Model 64S sensors and deployed at ENV. Each sensor had a nominal sensitivity of 0.08 mV Pa^{-1} and a flat response to within 3 dB from 0.01 to 245 Hz. Each sensor was mounted within a weatherproof case (1300 Case, Pelican). A single data acquisition system (PGS-140 four-channel, Pegasus) was used to record the Chaparral Physics sensors at 1000 Hz. The nominal separation between each sensor and the center sensor was 60 m, which produced an aperture of 112 m. OSU also deployed eight model ISSM23 microbarometers manufactured by the Wilson Engineering Research and Development (WERD). These sensors had a nominal frequency range of 0.1–200 Hz and had onboard sampling at 400 Hz. One of the sensors malfunctioned during the deployment, leaving only seven that successfully recorded the reentry. Four of the sensors were arranged in a triangle with an aperture of 51 m and centered on the Chaparral Physics array center sensor, with the fourth WERD sensor colocated at the center. The remaining three WERD sensors were positioned around the southwest sensor of the Chaparral Physics array with an aperture of 51 m.

OSU also deployed five Gem infrasound loggers (Anderson et al. 2018). Each sensor was secured within an enclosure that was then secured inside of a small Styrofoam box, with the side walls replaced with the windscreens developed in Swaim et al. (2023). Three of the Gem sensors were arranged in a triangle with an aperture of 49 m and the east corner of the triangle colocated with the center Chaparral Physics sensor (and the one WERD sensor). It should also be noted that the UH also colocated a RedVox sensor at this central location, and UH colocated several of their sensors with OSU sensors. The remaining two Gem sensors were located between ENV and the OSIRIS-REx SRC flight path to the south of the airport. These Gem sensors were 26 and 34 km south of the ENV deployment.

UH, along with AFRL and INL, deployed smartphones with the RedVox app, which utilizes the phone's built-in microphone (Garcés et al. 2022) in a variety of locations, including the West, East, and Distal Regions. Deployment locations in the East Region included Clive, Utah, Dugway, Utah, and around US Route 93 Alternate, Nevada.

The BSU infrasound campaign used Gem infrasound sensors (ver. 1.01). The instruments used belong to BSU and were deployed as part of a temporary network active between 2023 July and October. The southwest Idaho infrasound network operated by BSU was deployed in Reynolds Creek Experimental Watershed (Seyfried et al. 2018) from 2023 July to October with objectives of recording a prescribed wildland fire and regional signals in addition to the OSIRIS-REx entry. The large array ("TOP") included 44 sensors approximately in a rectangle with overall dimensions of 210 m × 120 m; its large size was intended to facilitate detecting weak signals while providing precise back azimuths in beamforming operations. Additionally, three four-element small arrays (JDNB, JDSA, JDSB) were deployed within 1.5 km of TOP, helping to increase the spatial extent of the overall network. The smaller dimensions of these arrays are due to being constrained to small protected zones within the anticipated prescribed burn area. When possible, sensors were placed in or under shrubs in order to mitigate wind noise in these treeless sites.

6.2. Seismic

SNL deployed two seismic nodes colocated with each infrasound array. The nodes were buried at EUE because we had permission to dig holes. However, land permits at the other two arrays did not allow for digging, so the nodes were placed on the surface. An additional 12 seismic nodes were deployed at EUE, distributed across a large area. As mentioned in the previous section, LANL installed six seismometers colocated with infrasound sensors (see the appendices for further details).

At EUE, UM also set up seismic sensors. A 1 km aperture, phased seismic array was sized to fit in the northern part of county land associated with the EUE (see Appendix C). The EUE was chosen because of its proximity to the ground track of the incoming capsule trajectory (within 10 km) and because Eureka County allowed seismometers to be buried. The phased array is relatively unusual and based on the "Golay 3 × 6" geometry (Followill 2006). It consists of six tripartite subarrays arranged in a surprisingly open geometry following design principles of minimizing the number of array elements while maximizing the array spatial bandwidth (Followill et al. 1997). This can be seen in the co-array diagram that shows uniform sampling in space (Figure A16 in Appendix A). The broadband array response (Nawab et al. 1985) shows a highly focused beam that can resolve the slowness of the expected infrasound signal to 0.02 s km^{-1}. Instrumentation for the seismic array elements consisted of Magseis–Fairfield three-component nodal seismometers (see Appendix C). These seismometers have a low-frequency corner near 5 Hz, self-contained GPS timing, and power and data storage for 30-day deployments. Installation consists of digging a 20 cm deep hole with a posthole shovel such that the top of the seismometer is within 5 cm of the surface in order to maintain GPS lock. Seismometers were oriented with respect to north using a magnetic compass. Instruments were installed on September 21 and 22 at locations determined using a handheld GPS receiver. Thus, location accuracy is estimated to be within 3 m of the target locations. Note that 20 seismic sensors served to detect OSIRIS-REx. The refraction profiles included 48 vertical component geophones and 48 horizontal component geophones, but these were not used to detect the SRC signals.

At the BFRA site, JHU installed Fairfield ZLand three-component nodes equipped with GPS timing and inbuilt power supply. These are deployed from a handheld terminal and placed in a small hole in the ground. Recovery also uses this terminal. The sampling rate is 2000 Hz. Instruments were placed into an 11-station array, in a cross-shape with the long axis aligned parallel to the OSIRIS-REx trajectory. The field site was left unattended, and instruments were collected back in the afternoon after the reentry.

6.3. DAS with Colocated Seismoacoustic Sensors

LANL deployed single-mode optical fiber at two sites: EUE and in Newark Valley (Figure 5). Fiber was laid on the ground (deployment photos are provided in Appendix A). An AP

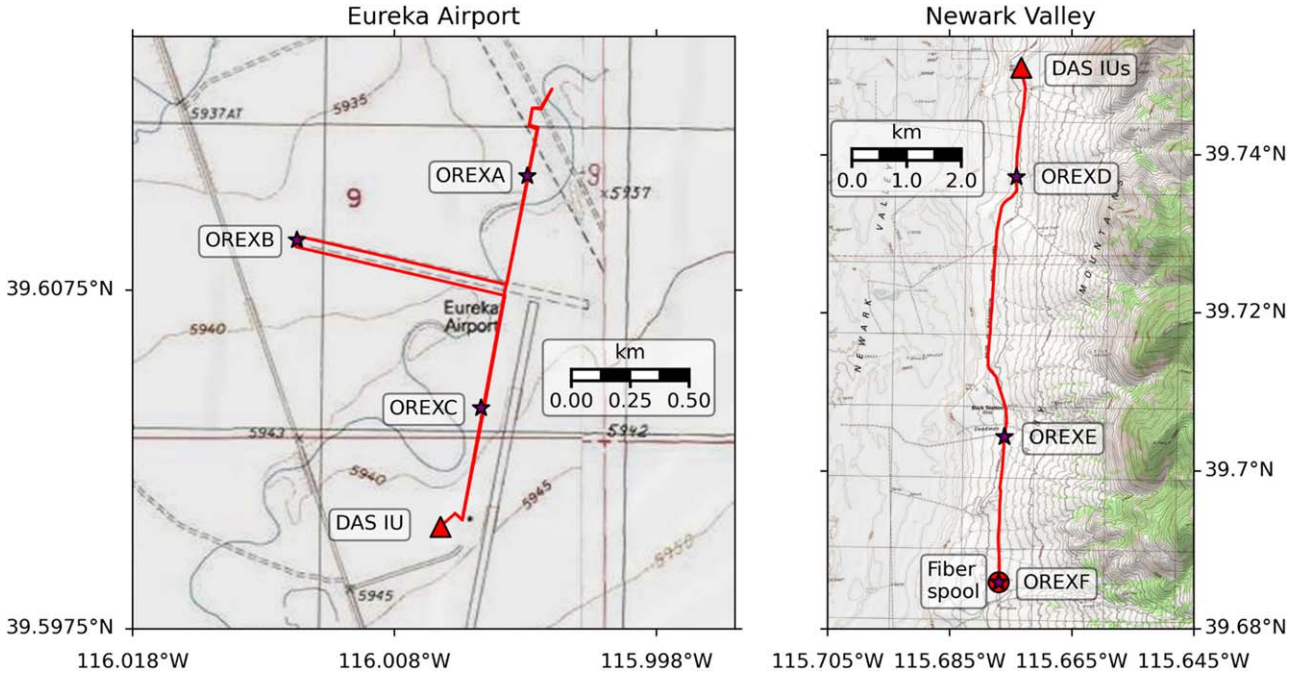

Figure 5. Map of DAS and colocated seismometers and infrasound instruments deployed at two sites: at the Eureka Airport (left) and in Newark Valley (right). OREXA, OREXB, OREXC, OREXD, OREXE, and OREXF are colocated seismometer/infrasound pairs. DAS IU(s) indicates the DAS interrogator unit(s). At the Eureka Airport, fiber was placed running from the DAS IU toward OREXC and continuing along the edge of the main taxi runway, before bending 90° toward the west (toward OREXB) along the cross runway, then returning to the main taxiway and continuing north toward OREXA. The fiber returned from the turnaround point to the north of OREXA and continued directly toward OREXC without returning to OREXB. In Newark Valley, the fiber ran from the DAS IU south past OREXD, OREXE, and OREXF. A spool with the remaining fiber was placed near OREXF.

Sensing instrument (N5225B-R100) was used at the airport to probe 4.5 km of fiber. The AP Sensing DAS had a sampling frequency of 500 Hz, a gauge length of 5 m, and a channel spacing of 1.23 m. In Newark Valley, a Silixa iDASv2 (Version 2.4.1.111) and an Alcatel OptoDAS were connected to 7.5 km of single-mode optical fiber. The iDAS used a sampling frequency of 500 Hz, a gauge length of 10 m, and a channel spacing of 2.0 m. The OptoDAS used a sampling frequency of 10 kHz, with a gauge length of 5.1 m and a channel spacing of 1.02 m. All DAS units operated intermittently for testing purposes in addition to during the reentry, unlike the seismometers and infrasound sensors that operated continuously. LANL installed six of each colocated seismometers (Geospace HS-1 3 Component) and infrasound sensors (Hyperion IFS-3000) at strategic locations along the DAS fiber (for complete instrumentation details, see the appendices). The seismometers and infrasound sensors recorded at 200 Hz, with each seismometer-infrasound sensor pair connected to a RefTek 130 data logger with timing information provided by Garmin GPS 16x-HVS antennas. All instruments were deployed specifically for the purposes of capturing the reentry. Instruments were installed over several days prior to the reentry and removed by the evening of 2023 September 24 (local time).

6.4. Balloons

SNL and JPL deployed balloons carrying sensor payloads. There are several types of balloons capable of bearing infrasound payloads. All of them depend on relatively low winds at the launch site, and some have additional restrictions, such as requiring sunlight to fly. To increase the odds that at least one balloon would be successfully deployed during the OSIRIS-REx overflight, SNL and JPL deployed two helium zero-pressure balloons, two helium meteorological balloons, two 7 m diameter heliotrope solar hot-air balloons towed aloft using helium meteorological balloons, and two "cloudskimmer" 3.5 m heliotrope solar hot-air balloons. Each balloon carried a parachute to slow the payload during descent. They also carried a flight termination system that ended the deployment when the balloon crossed a preprogrammed geofence and/or after a certain amount of time had elapsed. Some balloons utilized Balloon Ascent Technologies Bounder, and others used a High Altitude Science Stratocut termination system. The balloons were tracked using StratoTrack Automatic Package Retrieval System radios that transmitted during flight and a SPOT TRACE unit that reported the payload position after landing using the Globalstar satellite network. The location of this equipment on the balloon is shown in Figure 6.

Helium zero-pressure balloons climb until they reach their neutral buoyancy altitude. Two zero-pressure balloons with a maximum capacity of 4300 cu ft (121.8 m^3) were fielded, each targeting a different altitude in the lower stratosphere. The sensor packages consisted of Paroscientific Digiquartz 15A-IS microbarometers and an InertialSense μINS inertial measurement with a Raspberry Pi flight computer and custom-built interface board (similar to Brissaud et al. 2021). The Paroscientific microbarometers recorded at 158 Hz with an internal five-stage anti-alias filter set at 25.1 Hz, providing a pre-digitized output. The inertialSense IMU was sampled at 15 Hz. Each balloon had two sensor packages separated by a 33 m tether. The inertialSense IMU also provided timing information from the Global Navigation Satellite Systems (GNSS) network to the Paroscientific barometers through the custom interface board for time stamps accurate to 1 μs for time-of-flight analysis.

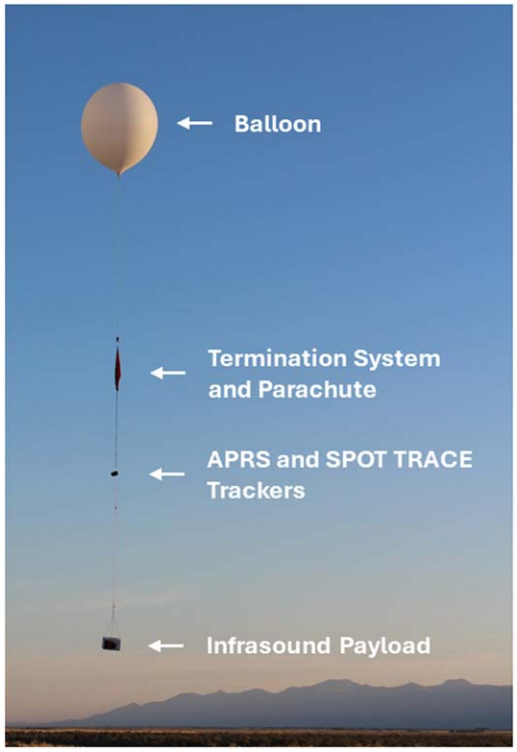

Figure 6. Example infrasound balloon configuration from the OSIRIS-REx deployment. This is the low-altitude weather balloon just after release. Photo credit: R. Lewis.

Meteorological balloons climb continuously until either they burst or the flight is terminated by other means. Despite relatively high levels of wind noise during ascent, Popenhagen et al. (2023) found that distant acoustic events could be recorded on such platforms. Thus, we deployed two meteorological balloons with infrasound payloads: a Kaymont 3000 g envelope released early with a rapid ascent rate and a Kaymont 600 g envelope released later with a very slow ascent rate. The rapid-ascent balloon was meant to capture the OSIRIS-REx signal in the lower/middle stratosphere, and the slow-ascent balloon was meant to capture the signal within a few acoustic wavelengths of the ground. Each balloon carried two InfraBSU microbarometers (Marcillo et al. 2012) and a Camas condenser microphone (Slad & Merchant 2021) digitized on a DiGOS DATA-CUBE recorder digitizing at 400 Hz. One of the two infraBSU microbarometers was polarity reversed, which assists in discriminating between true pressure signals and spurious nonpressure fluctuations like those caused by electronic interference (Bowman et al. 2019).

Heliotrope solar hot-air balloons rise into the lower stratosphere, where they maintain a constant altitude until sunset or the flight is terminated by other means (Bowman et al. 2020). They are less expensive and can be launched at a more rapid cadence than zero-pressure balloons but have more restrictive launch conditions. This constant altitude greatly reduces wind noise on infrasound microbarometers, permitting much fainter signals to be recorded. However, the OSIRIS-REx overflight occurred too close to dawn, meaning that the heliotropes would not be able to reach their neutral buoyancy in time to record the acoustic signal. Therefore, two 7 m diameter heliotropes were towed aloft by meteorological balloons and then released into sunlight, achieving level flight before the OSIRIS-REx event. After dawn, two 3.5 m "cloudskimmer" heliotropes were launched from the ground in the hopes that their slow ascent rate would reduce wind noise to acceptable levels. One 7 m heliotrope carried a single Gem microbarometer (Anderson et al. 2018), and the other carried two Gem microbarometers separated by a 30.5 m long tether. The Cloudskimmer balloons each carried an Android cell phone running the RedVox infrasound recording app (Garcés et al. 2022; Popenhagen et al. 2023). The RedVox phones recorded pressure data at 800 Hz.

Starting about a week before the reentry, trajectory calculations were performed at least daily in order to refine our launch times and ascent rates. The area of operation was challenging, with restricted airspace on three sides. Furthermore, the OSIRIS-REx landing site was to the east of Eureka Airport—exactly where the balloons were expected to go. Therefore, we set termination geofences to prevent balloons from drifting into restricted airspace, including the OSIRIS-REx landing site.

Balloons were launched in two batches: an initial salvo meant to capture signals at high altitude (>20 km) and the second intended for very low altitude recordings (within several acoustic wavelengths of the ground). The first batch included the 7 m heliotrope balloons towed aloft using helium-filled meteorological balloons, one meteorological balloon with an infrasound payload, and the two helium zero-pressure balloons. The first balloon was launched at 11:54 UTC, and all but one had been launched by 12:12 UTC. The final zero-pressure balloon was launched at 13:12 UTC. The second batch consisted of a very slowly ascending meteorological balloon and the two cloudskimmer heliotropes. The meteorological balloon was released at 14:00 UTC, and the last cloudskimmer was released at 14:13 UTC.

Despite gusty winds in the town of Eureka, conditions were calm at the airport, due to a strong temperature inversion that had set up overnight. Winds began to pick up around 14:05 UTC, resulting in the decision to add helium to the cloudskimmers to help them get off the ground faster. Because of the rising wind and the imminent arrival of the OSIRIS-REx SRC, we opted not to launch the spare heliotrope balloon. Instead, we left the still-recording spare payloads at the launch site and proceeded to the pilots' lounge. After the capsule overflight, the balloon flights were automatically terminated. Payloads from the low-altitude meteorological balloon and both cloudskimmers were recovered on the same day. The remainder of the payloads were recovered the following day.

6.5. GPS

LANL's GPS team deployed in the West Region, with the aim of measuring and characterizing ionospheric Total Electron Content (TEC) signatures (via GPS *L*-band measurements), as well as atmospheric current and electric field signatures. Analyses involve modeling and measuring signature speed and period, geolocating likely sources, and estimating source strength using the LANL/GPS Rex-five stations with controlled/compact placement and large data-rate collections to probe small-scale ionospheric effects. The most significant caveat of this method, of course, is that ionospheric TEC signatures with the highest SNR are known to be tens of minutes delayed from any source in the troposphere. The LANL/GPS team deployed five GPS/GNSS ground stations at EUE along the runways: four along one taxiway (stations Rex-2, Rex-3, Rex-4, and Rex-5), and one at the end of its orthogonal dirt runway (station Rex-1). The geographical coordinates are listed in the appendices. Septentrio PolaRX5s GPS receivers were

used in all stations with Veraphase 6000/High-Precision Full GNSS Spectrum Antennas. Standard solar panels and voltage regulators were used to supply power. Power expectations were designed to ensure that consistent power was maintained.

When properly calibrated, GPS ground stations measure the group and phase dispersion of *L*-band signals (1–2 GHz) to all GNSS satellites simultaneously. These measured quantities determine the integrated electron density along the line of sight or TEC to each satellite. Nearly all of that dispersion occurs in the ionosphere, and mostly near the altitude of peak ionization (250–400 km). As a result, these lines of sight, mapped though the ionosphere, can be used to scan for small changes and to characterize and locate atmosphere-impacting events perturbing the upper atmosphere.

The GPS stations, atmospheric current, and electric field measuring instrumentation were set up a few days prior to the OSIRIS-REx SRC reentry to ensure that all units were working properly and calibrated. The GPS stations were deployed less than 400 m apart from one another to allow detection of small-scale ionospheric disturbances. The most widely separated stations were 2000 m apart, nearly spanning the EUE main taxiway. In addition, the data-measuring interval was set to 50 ms to enhance the resolution of small timescale measurements of ionospheric disturbances. The OSIRIS-REx SRC reentry occurred nearly an hour after dawn under clear skies.

7. Preliminary Results

Here we present a snapshot of the preliminary data and our initial results. Nearly all instruments located near the nominal trajectory (i.e., direct arrivals) successfully detected the signals produced by the reentry of OSIRIS-REx. Additionally, numerous stations in the Distal Region also captured the signals. Illustrative examples of detections are shown throughout this section to demonstrate the remarkable success of this largest-ever geophysical observational campaign of a reentry. We note that some results are omitted from this paper because detailed analyses are underway by various teams and will be disseminated as separate studies in due course.

7.1. Witness Reports

During the anticipated time window during which the OSIRIS-REx SRC overflight was expected to take place, the teams in the West Region exercised the so-called silent observation time. At EUE, some team members were stationed at the airport entrance to prevent inadvertent vehicular intrusion into the observation zone. The highway adjacent to EUE is commonly busy, and with steady tractor trailer traffic. We asked the local police if they could assist in temporarily closing the highway during the overflight, but the request needed to be escalated with the Nevada State police. Despite lacking direct confirmation regarding the feasibility of our request, the EUE team observed a notable absence of vehicular activity for several minutes prior to reentry, indicative of a road closure. The area was nearly windless and very quiet, and the only dominant audible noise came from birds and a rooster. Regrettably, approximately 1 minute before the anticipated OSIRIS-REx overflight, we noted a gradual resumption of vehicular activity. By the time traffic returned to full speed, the OSIRIS-REx SRC had already passed, but not before some traffic noise started to become apparent. At EUE, the experiences in audible perception of a possible sound generated by the OSIRIS-REx reentry varied. Some people perceived it as a single soft "thump," some as a double "thump," while others heard nothing. Notably, the observed audible signatures (or lack thereof) exhibited strong dependence on the locality where the witnesses were present at the time. The sound may have gone unnoticed if individuals were engaged in casual conversation.

In Newark Valley, during the silent observation time, team members observed several airplanes, bird noise, and various wind noises. One team member out of six likely saw the OSIRIS-REx SRC. Four observers in Newark Valley heard a double boom at 14:45:52 UTC; other observers recorded the time to the minute as 14:45 UTC. Newark Valley observers perceived the sound as coming from the east (two observers), southwest (one observer), and northwest (one observer). The four Newark Valley observers agreed that the sound was distinct and unmistakable given the quiet conditions but could have been missed if a loud conversation had been happening. A clip from the video recorded by Carr's personal phone is included in a .tar.gz package. The animation clip begins at 14:45:40 UTC and ends at 14:46:00 UTC. A double boom is audible about 11 s into the clip, corresponding to 14:45:51 UTC. The SRC is not visible in the recording. A more detailed account of the LANL team's visual and audible observations in Newark Valley can be found in Appendix A. There were no visual or audible observations from the BFRA site at the time of reentry.

In the East Region, both the OSU and UH teams heard the sound. The entire OSU team viewed the reentry from their lodging location (40.7347N, −114.0805E). One audible boom was heard at 14:46 UTC that was not loud but easily noticeable. The JSU team, situated at 39.2646N, −116.0269E at the time of reentry, heard a clear single "thud" at 14:46:45 UTC. The OSU team had noted that the sound would likely be brushed off as another ancillary source of noise if not expected. It was very calm with little to no wind (i.e., no wind at the observation location as perceived by the team) and mostly clear skies. The team members located in Clive, Utah, also heard a soft, double "thump" resulting from the sonic boom.

7.2. Signal Detections on Ground-based Sensors

All of SNL's arrays and most Gems detected clear signals generated by the OSIRIS-REx SRC reentry. A plot with the arrivals received at Gem stations south of the nominal reentry path is shown in Figure 7. The time series were filtered with a high-pass filter at 10 s. The difference in timing is due to the airwave traveling a longer path to more distant stations. The N-wave indicates a ballistic arrival. Station A05 was closest to the nominal trajectory (∼13 km), and A01 was the farthest (∼40 km). More detailed analysis is needed to determine whether all stations received the signal from a single point of the reentry path or perhaps from different points along the trajectory. The latter is more plausible when one considers the ballistic nature of the shock wave.

All the instruments deployed by LANL in the West Region captured the signal from the capsule. All seismometers and infrasound sensors recorded high-SNR signals (Figure 8). The Silixa DAS data recorded a move out of the signal as it propagated along the fiber that can be seen without any preprocessing (Figure 8 shows data from fiber wrapped around a spool near OREXF). The AP Sensing (EUE) and OptoDAS (Newark Valley) recorded the signal, but the signal is only

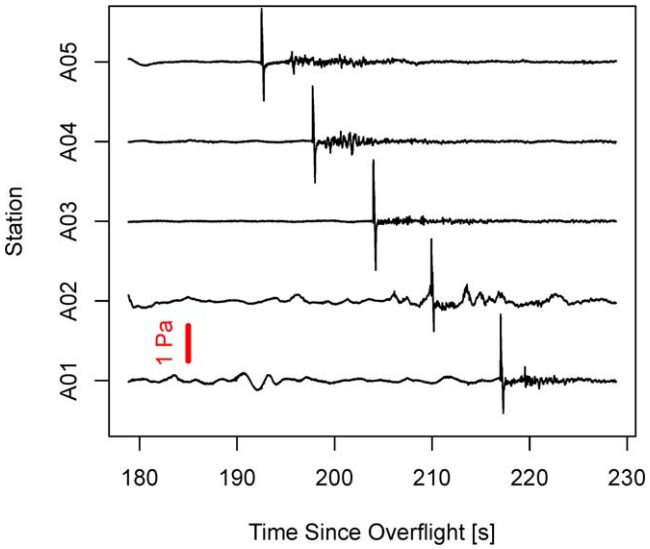

Figure 7. Signals received at Gem stations situated south of the nominal reentry path in Newark Valley (Strawberry Road). The time series were filtered (high pass, 10 s). The *x*-axis is in seconds from 14:45:50 UTC.

visible after data preprocessing. In the examples shown in Figure 8, we manually pick arrivals because the SNR is so large (red circles in Figure 8). For infrasound detection, we choose the corner at the start of the increase in pressure of the incoming N-wave (peak amplitude). For the seismic records, we pick the corresponding corner at the start of the rise toward the first high-SNR peak amplitude on the vertical channel. For the DAS detection, we pick the corresponding corner at the start of the rise toward the maximum peak in strain. Detection metadata are in Appendix A, Table A1.

TDA's Large N-array started collecting data at 19:23 UTC on September 23 and stopped collecting data at 15:05 UTC the next day, shortly after the reentry. At the time of the reentry (14:46 UTC), 114 of the 115 sensors were collecting data and detected the N-wave generated by the OSIRIS-REx SRC (clearly visible in Figure 9).

Three of the four SMU infrasound sensors made a detection, clearly noticeable even without any data filtering (see Appendix A). KUT's infrasound instruments and microphones also detected the signal generated by the OSIRIS-REx SRC reentry, with the arrival time around 14:45:59 UTC (see the appendices). The apparent direction of arrival was north to south, as expected. JHU recorded a clear sonic boom on all seismic stations, arriving at approximately 14:46 UTC. The lateral offset from the nominal trajectory was less than 2 km.

All passive seismic and infrasound sensors deployed by UM recorded the capsule return signal. UM also obtained an extensive data set of refraction waveforms to be used in developing P and S velocity functions for the sediments of Diamond Valley using body wave arrival times and high-frequency surface wave dispersion. The refraction profile data are necessary to develop appropriate Earth models at the site. These velocity models are important for inferring the efficiency of the acoustic−seismic interaction and to understand how secondary seismic waves distort the acoustic source function as seen by a seismic instrument. Seismic signatures can be affected by local P-to-S conversions, by creation of Rayleigh waves, and by the absolute values of both the P and S wave velocities in the near surface (e.g., Langston 2004).

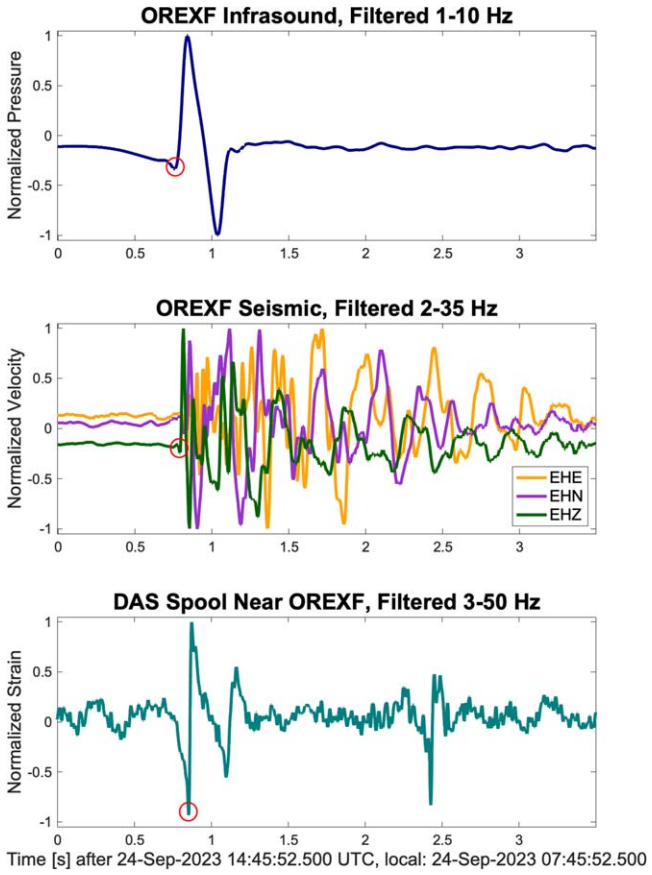

Figure 8. High-SNR arrivals on the colocated OREXF infrasound (top) and three-channel seismic (middle) sensors and on fiber wrapped around a spool near OREXF (bottom); the sensor is at 7436 m from the interrogator at channel 3718. Data are filtered with a bandpass filter from [1–10] Hz for the infrasound channel, [2–35] Hz for the seismic channels, and [3–50] Hz for the DAS channel. Time picks are shown with open circles.

Broadband frequency-slowness analysis of the seismic array data gives an apparent velocity of 2.9 km s^{-1} and azimuth of approach of the acoustic N-wave of N02°E. We observed significant differences of both acoustic and seismic signals between the western and eastern infrasound arrays (Figure 10) suggesting differences in atmospheric wave propagation and differences in local seismic site responses. Indeed, we also saw significant differences in the seismic responses between northern and southern stations (Figure 10), suggesting the development of secondary Rayleigh waves.

Smartphones running the RedVox infrasound recording app detected strong signals (see the appendices). OSU's sensors at ENV that were operational during the reentry (14 out of 15 sensors) detected a signal at 14:47:16.5 UTC. All of these sensors were ∼58 km from the perpendicular intersection of the OSIRIS-REx SRC trajectory. The received wave was an N-wave with more broadband coherent "rumbling" after the initial arrival. Figure 11 shows the signal recorded by the Chaparral array. The sensors situated south of ENV also captured the signal from the reentry. The signal first arrived at Gem 092 at 14:46:02.7 UTC and then at Gem 074 at 14:46:17.2 UTC. These two sensors were ∼25 and ∼33 km, respectively, from the perpendicular intersection of the OSIRIS-REx SRC trajectory. Both sensors had a dominant N-wave arrival, with some broadband coherent "rumbling" after the initial arrival.

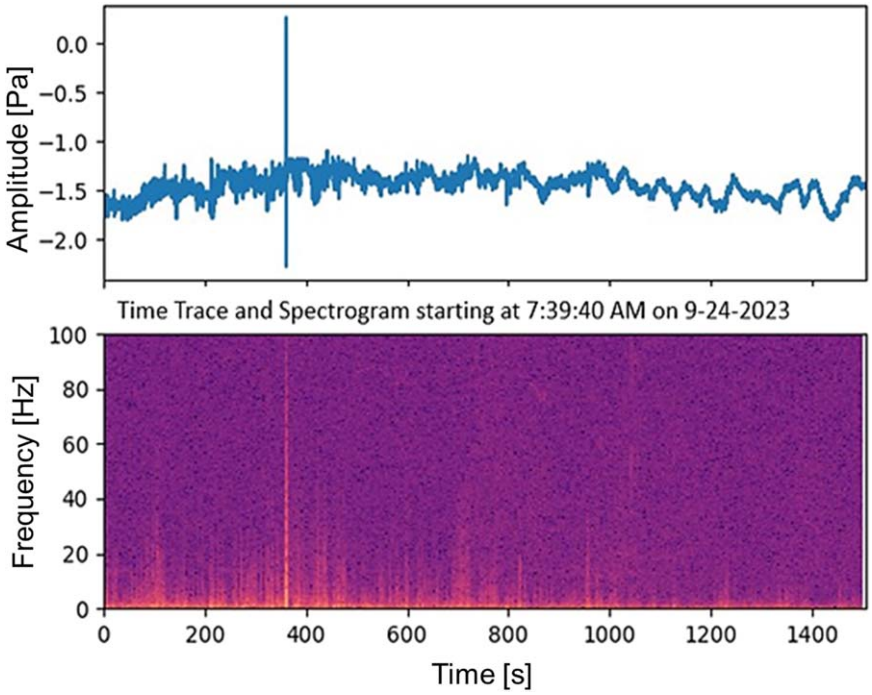

Figure 9. Signal detected at one of the TDA sensors of the Large N-array. The strong signal is clearly visible just before the 400 s mark. The top panel shows the time series, while the bottom panel shows the spectrogram.

In the Distal Region, early analysis from BSU's Idaho stations shows possible signals. At this location, we recorded good data from 47 of 66 sensors during the OSIRIS-REx entry. Causes of sensor failure include dead batteries, disturbance by cattle, and theft/loss. The AWE's station at the NNSS detected the signal (Figure 12). All LANL's sensors in the Distal Region performed well. The array near Price, Utah, did not detect the OSIRIS-REx reentry. However, the other two arrays (NNSS array (Figure 12) and the St. George, Utah, array) did capture signals from the reentry. The stations at NNSS are situated ∼260 km from the point of peak heating.

Infrasound signals in the 1–4 Hz passband that were observed on two small-aperture four-element arrays at ∼420 km west–southwest of the OSIRIS-REx landing site (Figure 12) exhibited back azimuths (the direction from which the signal arrived) of ∼345° (i.e., from just west of north) consistent with signal generation along the reentry trajectory. The arrays are separated by a horizontal distance of 1500 m and a vertical distance of 300 m, with PSDJK (AWE) located on top of a mesa and OREX1 (LANL) located in the base of a steep-sided valley.

Although the signals at each array are qualitatively similar in terms of duration and waveform variation, beamforming results at OREX1 have a higher resolution, likely due to the larger array aperture of 160 m (compared to 100 m for PSDJK). Despite the close proximity of the arrays, there are significant differences in the temporal variations of background noise amplitudes. On the mesa, PSDJK exhibits low noise in the period prior to the OSIRIS-REx signal, such that a persistent high-frequency, low-amplitude acoustic source can be observed toward the west. During and after the OSIRIS-REx signal, the noise amplitude at PSDJK increases, obscuring the low-amplitude signal. The opposite is observed at OREX1 in the valley; here, high-amplitude noise prior to the OSIRIS-REx signal obscures the persistent source to the west. During and after the OSIRIS-REx signal, the noise amplitude drops, allowing the persistent source to be observed. This indicates how wind-generated noise at an array can be highly localized, as well as the impact it has on signal detection.

7.3. Balloon-borne Infrasound

The high-altitude meteorological balloons and heliotropes traveled farthest west (relative to other balloons) owing to their relatively low ascent rates (Figure 13) and were over halfway to the capsule's altitude at the time of overflight (Figure 13). The zero-pressure balloons were about 50 km from the launch site at the time of the overflight. The cloudskimmers and low-altitude meteorological balloon were still quite close to the launch site because they were released just before the overflight. Ground winds were generally low, allowing for the successful inflation and launch of the balloons. While a strong tropospheric jet was present, the winds were not rapid enough to carry the balloons into the termination zone before the OSIRIS-REx SRC reentered. The balloon data are being analyzed and will be published in the near future.

7.4. GPS

The LANL GPS team observed several signatures originating from the incoming OSIRIS-REx (SRC; Figure 14). Several faint signatures were detected in the TEC along lines of sight from our GPS ground units through the ionospheric peak density altitudes, arriving more than 10 minutes after the reentry as expected (having traversed 300 km from maximum shock-wave altitudes to the ionospheric peak; Figure 14, left panel). Estimated ionospheric signatures were traveling at speeds expected in the thermosphere (greater than 800 m s^{-1}), much faster than ground speeds (343 m s^{-1}). We were also able to observe signatures (possibly moving at faster speeds) in the refined GPS scintillation measurements. In addition, data from 12 publicly available GPS ground stations within 300 km of

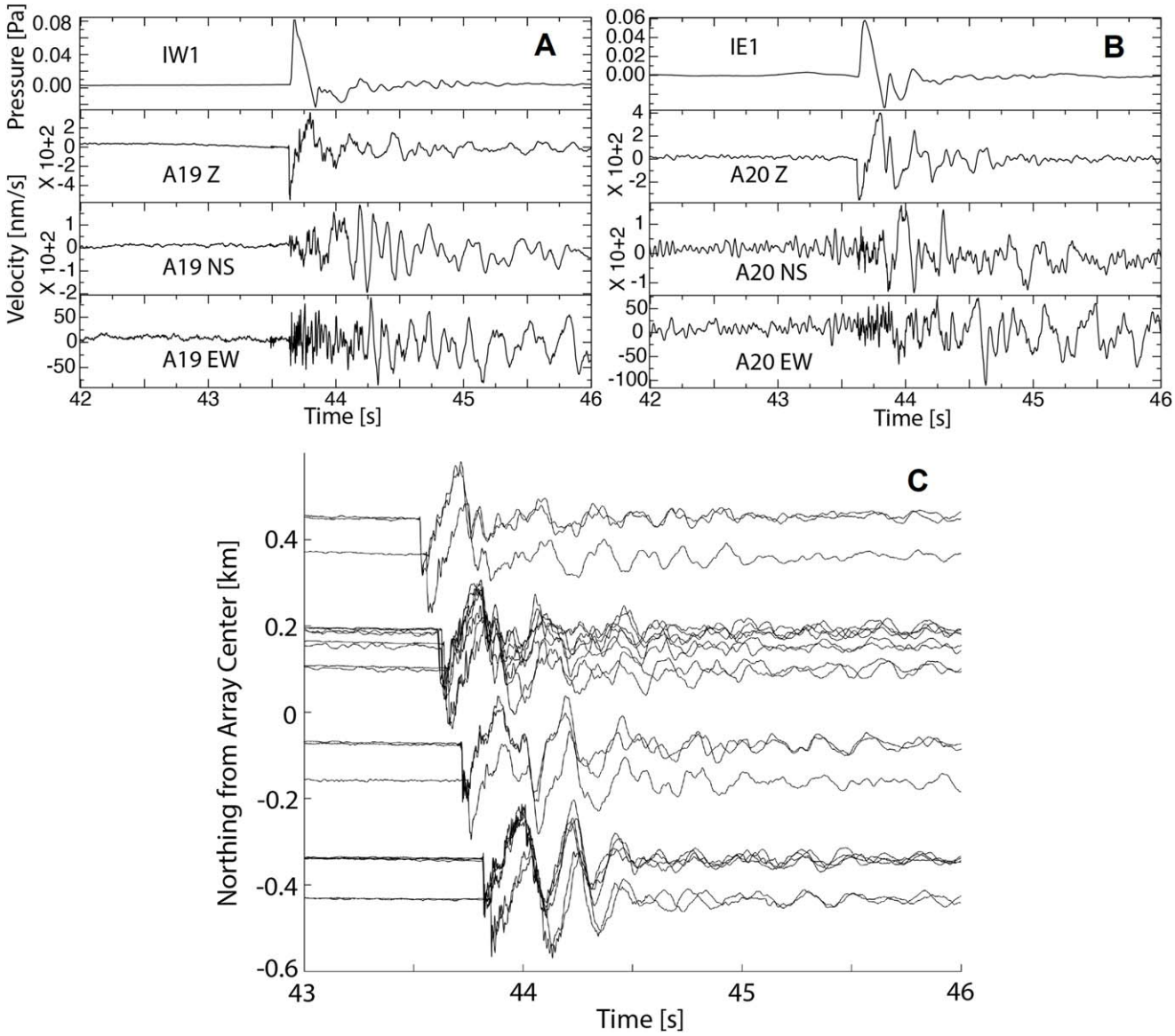

Figure 10. Comparison of pressure and ground velocity data at the central elements of the (a) western and (b) eastern UM seismoacoustic arrays. Pressure and velocity amplitude values are provisional pending further calibration of the instruments. Time is relative to 14:45:13.818 UTC. (c) Vertical velocity waveforms from the Golay 3×6 array plotted as a function of distance from an azimuth of 0°, i.e., the data have been plotted along a virtual north–south profile, with north at the top of the figure. Waveform amplitudes have been normalized. Note the large oscillating secondary arrivals for stations in the south. Time is relative to 14:45:13.818 UTC.

Eureka (Nevada) were used to approximate the location of the final descent after the parachute deployment stage (Figure 14, right panel). The immediate results of the observational campaign are encouraging. The LANL GPS team will continue to examine the data from the OSIRIS-REx capsule return and refine their analysis methodologies.

8. Conclusions

NASA's OSIRIS-REx SRC returned to Earth on 2023 September 24, delivering precious cargo consisting of physical samples of the asteroid Bennu. This was the first asteroid sample return mission for the United States. Considering that SRCs come from interplanetary space at hypervelocity, they can serve as ideal analogs for studying meteor phenomena. The most recent reentry over the United States had been in 2006 with the return of NASA's Stardust mission. The OSIRIS-REx SRC's hypersonic flight through the atmosphere provided an exceptionally rare opportunity to carry out geophysical observations of a well-characterized source with known parameters, including timing and trajectory.

A large team of researchers from 16 institutions gathered to perform a coordinated geophysical observational campaign at strategically and carefully selected locations that were projected to provide robust and high-fidelity data. Over 450 ground-based sensors including infrasound, seismic, DAS, and GPS were deployed. Moreover, several balloons carrying infrasound sensors were launched with the aim of capturing the signals at high altitude. This was the largest geophysical observational campaign of a reentry ever performed, collecting a wealth of valuable data that are expected to promote scientific inquiry for many years to come.

The observational campaign was highly successful, with detections on nearly all instruments, near and far. Here we present our early results collectively, noting that more focused studies will be disseminated in due course. Data collected during this effort will be eventually made openly available.

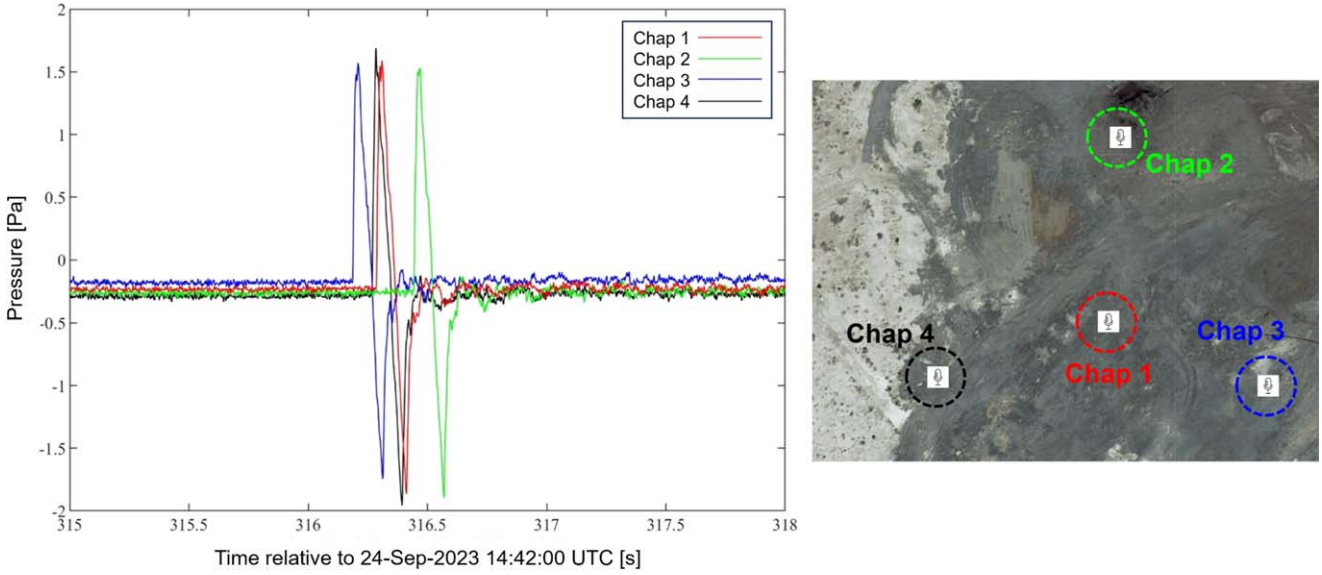

Figure 11. Left panel: time trace from the four Chaparral Physics model 64 s sensors in OSU Array 1 located at the Wendover Airport. Right panel: satellite image showing the orientation of the sensors (Chap 1–4), with colors matching those in the left panel, which shows that the signal was arriving from the south–southeast direction. The width across the map is 175 m.

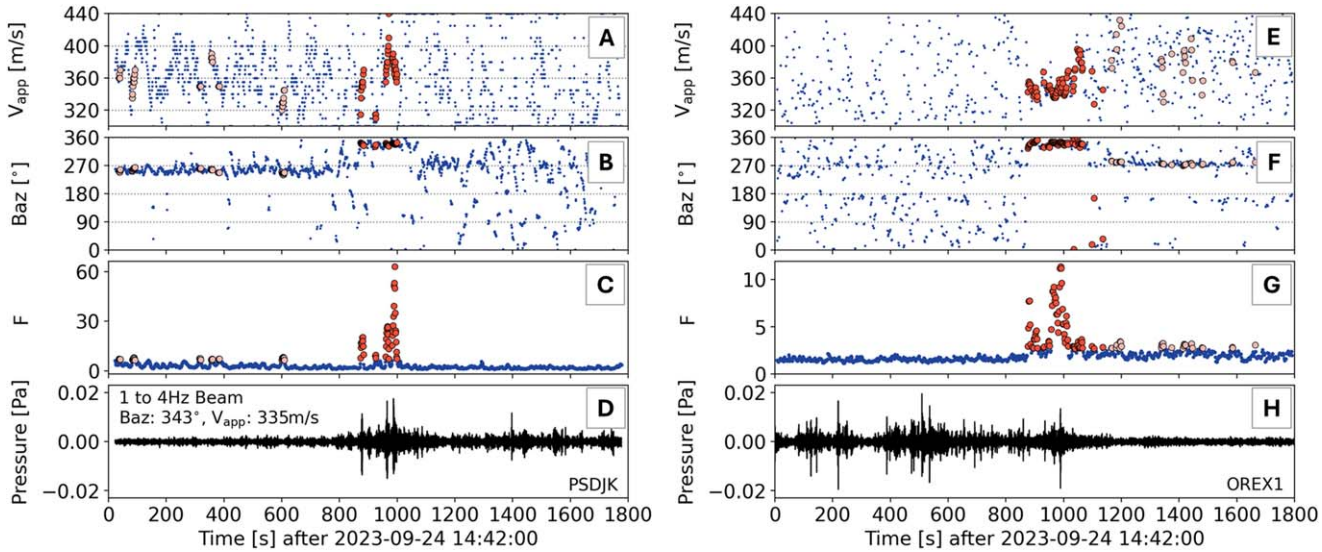

Figure 12. Left: AWE's PSDJK array. Right: LANL's OREX1 array. Panels top to bottom show values of apparent velocity (V_{app}), back azimuth (Baz), and *F*-statistic (F) corresponding to the beam direction that exhibits the highest signal coherence across consecutive 4 s long windows (overlapping by 50%). Orange circles represent time periods for which there is a >95% probability that the window contains a signal with an SNR greater than or equal to 4. The bottom panel shows the 1–4 Hz beam for a back azimuth of approximately 345°. Note that the OSIRIS-REx signal is seen above a persistent low-SNR signal arriving from a back azimuth of approximately 260°.

Here we summarize our preliminary findings and conclusions:

i. Infrasound and Seismic: The campaign to record the OSIRIS-REx capsule return seismoacoustic signals was remarkably successful. Nearly all passive instrumentation at the variety of vantage points recorded the signal generated by the reentry. Most instruments performed well, including arrays, single stations, Large N-array, and smartphones. A diverse range of instruments recorded the signal at distances from beneath the nominal trajectory to several hundreds of kilometers from the nominal trajectory. The seismic array design proved to be able to accurately determine the wave characteristics of the incoming acoustic signal, and we observed interesting seismoacoustic interactions at our infrasound subarrays. Our refraction work is also an important element of the experiment since it will yield baseline information on near-surface P and S wave velocities that are important constraints on the nature of the acoustic–seismic interaction.

ii. DAS: As expected, within each site (Eureka Airport and Newark Valley), detections sweep across the instruments from north to south, with instruments closer to the trajectory recording arrivals before instruments farther from the trajectory. This event marks the first time that DAS recorded a reentry event. In Newark Valley in particular, the arrivals were clear across much of the 7.5 km of deployed fiber, despite the simple placement of cable directly onto the ground (no trenching). This is particularly promising in

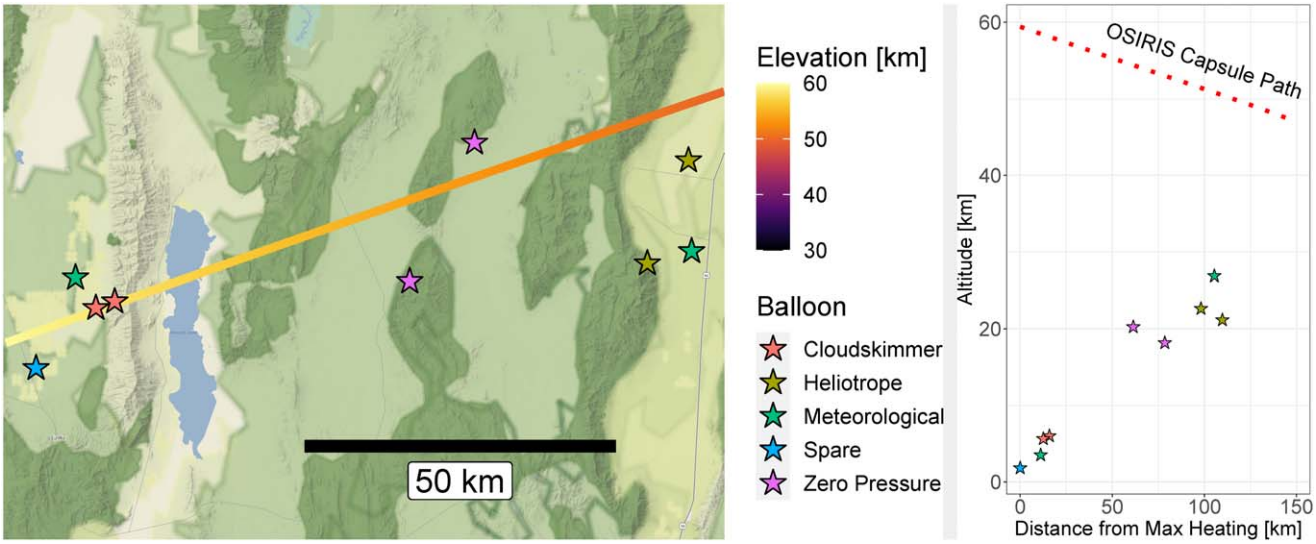

Figure 13. Left: locations of OSIRIS-REx balloons compared to OSIRIS-REx flight path and altitude. Map imagery from Stadia Maps. Right: altitude of balloon payloads at the time of OSIRIS signal arrival compared to the altitude of the OSIRIS-REx capsule.

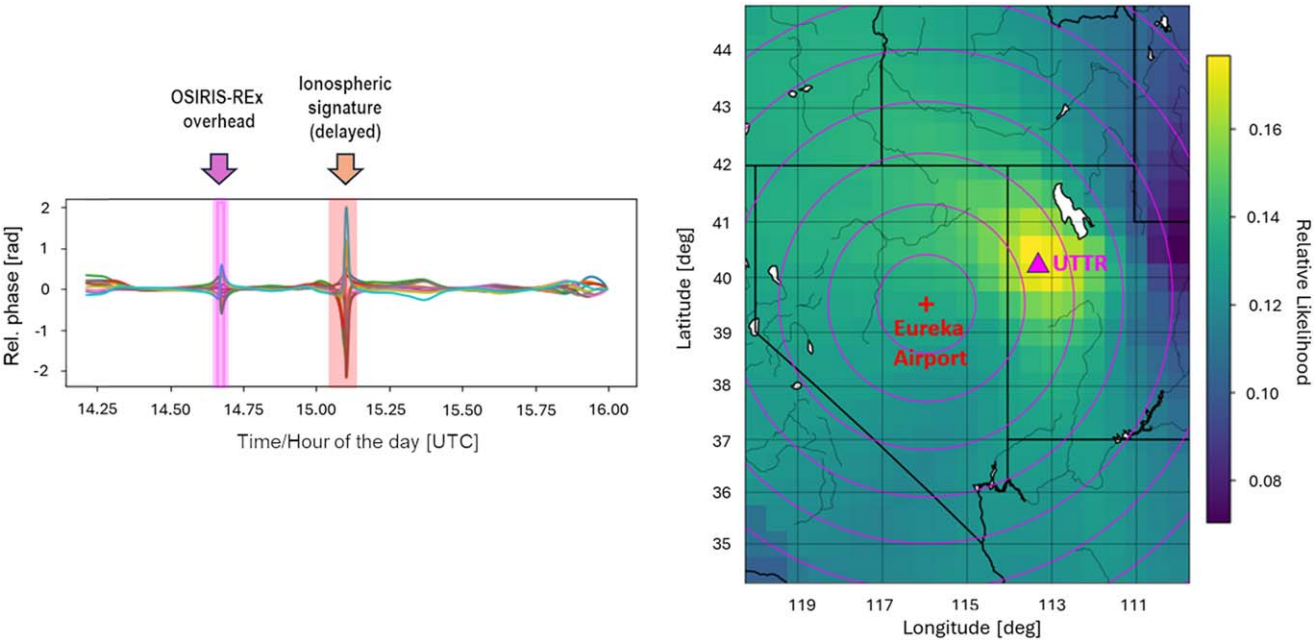

Figure 14. Left: relative LANL GPS filtered precision TEC measurements, identifying 10-minute acoustic signatures. Right: most likely acoustic source location identified from 10-minute TEC waves derived from public GNSS data.

light of rapid deployment observation campaigns, where trenching may be logistically prohibitive.

iii. Balloons: A diverse set of balloon-borne acoustic stations were fielded during the OSIRIS-REx observation campaign, with the hope that at least one of them would succeed. Fortunately, every airborne sensor recorded data during the overflight. While careful planning and experienced launch crews played a major role in this achievement, the weather played a critical part as well.

iv. GPS: The GPS observational campaign was successful. Several faint signatures generated by the OSIRIS-REx SRC during reentry were detected in the TEC and *L*-band scintillation (directly). Additionally, we were able to infer the location of the final descent after the parachute using data from a dozen publicly available GPS ground stations.

This largest-to-date observational campaign of a hypersonic reentry with a multitude of geophysical instruments provided valuable insight and data collection that can serve as a blueprint not only for terrestrial applications but also for future space mission planning. Future campaigns should attempt to capture the onset of the shock wave as the object transitions into the continuum flow regime. Having radiosondes launched in various locations along the ground track to collect atmospheric data up to 40 km altitude would be of immense value. Moreover, seismic instruments extending over a longer region would further help constrain the source. Because we prioritized the West Region, where the likelihood of capturing the signal would be the greatest, we did not have any dedicated seismic sensors farther east. Future balloon campaigns should focus on broadening the horizontal range between the sensors and the reentering object, as well as deployments at a wider array of azimuths.

Acknowledgments

The authors thank the two anonymous reviewers for their valuable and supportive feedback. The authors gratefully acknowledge the Board of Eureka County Commissioners (Chairman Rich McKay, Vice Chair Michael Sharkozy, Commissioner Marty Plaskett, and Deputy Clerk Jackie Berg) and the Eureka Municipal Airport personnel (Jayme Halpin). The authors thank Sergeant Adam Zehr (Nevada Highway Patrol) and Eureka County Deputies Jason Flanagan and Allison Flanagan for their assistance during the OSIRIS-REx SRC reentry. The authors also extend heartfelt thanks to the people of the town of Eureka for their hospitality.

We are grateful for the Bureau of Land Management Ely District Office for granting us permission to deploy sensors in eastern Nevada, as well as assisting us with coordination. We are also grateful for the BLM Salt Lake Field Office for granting us permission to deploy sensors in western Utah.

E. A. Silber thanks M. Moreau (NASA) for sharing the EDL data.

SNL. This article has been authored by an employee of National Technology & Engineering Solutions of Sandia, LLC under contract No. DE-NA0003525 with the US Department of Energy (DOE). The employee owns all right, title, and interest in and to the article and is solely responsible for its contents. The US government retains and the publisher, by accepting the article for publication, acknowledges that the US government retains a nonexclusive, paid-up, irrevocable, worldwide license to publish or reproduce the published form of this article or allow others to do so, for US government purposes. The DOE will provide public access to these results of federally sponsored research in accordance with the DOE Public Access Plan https://www.energy.gov/downloads/doe-public-access-plan. This paper describes objective technical results and analysis. Any subjective views or opinions that might be expressed in the paper do not necessarily represent the views of the US Department of Energy or the US government. This work was supported by the Nuclear Arms Control Technology (NACT) program at the Defense Threat Reduction Agency (DTRA).

LANL. This research was supported by Los Alamos National Laboratory (LANL) through the Laboratory Directed Research and Development (LDRD) program, under project No. 20220188DR and under the LANL Center for Space and Earth Science (CSES) LDRD project No. 20240477CR-SES. We also thank the Eureka County Commission and Eureka Airport for access at the airport site, and the Bristlecone BLM Field Office for guidance in complying with casual use requirements at the Newark Valley site. We are grateful for the loan of a field truck by the MPA-Q Division at LANL. Funding for Elisa A. McGhee was provided by the Pat Tillman Foundation Scholarship and the Colorado State University Vice President for Research Graduate Fellowship Program. Colors used in plots of seismic, infrasound, and DAS data are from Diana (2023). All the deployed instruments belong to LANL, with the exception of the OptoDAS, which was rented from Alcatel, and one personal cell phone. Loïc Viens was partly supported by the Chick Keller Fellowship from the Center for Space and Earth Science (CSES) at LANL. All tools and software used for measurement and analyses were LANL owned/operated, except the personal cell phone.

AWE and LANL acknowledge the assistance and expertise provided by our MSTS colleagues in deploying and maintaining the infrasound arrays at NNSS.

JPL. Contributions from JPL authors were performed at the Jet Propulsion Laboratory, California Institute of Technology, under a contract with the National Aeronautics and Space Administration (80NM0018D0004). The authors acknowledge funding from the NASA Planetary Science and Technology through Analog Research (PSTAR) program.

INL. INL is operated for the US Department of Energy by Battelle Energy Alliance under DOE contract DE-AC07-05-ID14517. This work was supported by the Department of Energy National Nuclear Security Administration under award DE-NA0003921 (Consortium for Enabling Technologies and Innovation).

OSU. This work was funded, in part, by Gordon and Betty Moore Foundation under grant GBMF11559 (10.37807/GBMF11559). The OSU team would also like to thank the Wendover Airport for providing access to the airport site.

UM: We would like to thank the Damele family of Eureka, Nevada, for allowing access to the eastern portion of the experiment through their farm, which is adjacent to the airport. The authors acknowledge the use of the "Seismic Analysis Code" (SAC) (Goldstein et al. 2003) in preparing this paper. Travel funding was provided by the University of Memphis Research and Innovation Office.

BSU. Data collection was funded by US Forest Service award 23-JV-11111135-067 and NSF award EAR-2122188. We thank Z. Cram and V. Porter for help arranging fieldwork in Reynolds Creek Experimental Watershed.

RedVox: This work was supported by the Air Force Research Laboratory under agreement FA8650-18-C-1669.

UH. This work was supported in part by the Department of Energy National Nuclear Security Administration under award Nos. DE-NA0003920 (MTV) and DE-NA0003921 (ETI). This report was prepared as an account of work sponsored by agencies of the US government. Neither the US government nor any agency thereof, nor any of their employees, makes any warranty, express or implied, or assumes any legal liability or responsibility for the accuracy, completeness, or usefulness of any information, apparatus, product, or process disclosed, or represents that its use would not infringe privately owned rights. Reference herein to any specific commercial product, process, or service by trade name, trademark, manufacturer, or otherwise does not necessarily constitute or imply its endorsement, recommendation, or favoring by the US government or any agency thereof. The views and opinions of authors expressed herein do not necessarily state or reflect those of the US government or any agency thereof. The US government is authorized to reproduce and distribute reprints for governmental purposes notwithstanding any copyright notation thereon.

Data Availability

Tables with the locations of the instruments are provided in the appendices. Tables B1 and C1 are also available in machine-readable format. Data from some components of this observational campaign will be made openly available in the future. UM data collected from this experiment will be openly available from the Seismological Facility for the Advancement of Geoscience (SAGE) of the EarthScope Consortium in 2025 September. Currently, the data are forming part of a PhD thesis at the University of Memphis. LANL/GPS observational data may be released at a later date. SMU data will be made available in the near future.

Appendix A

Appendix A contains additional deployment photos and figures with signal detections (Figures A1–A16), LANL signal detection metadata (Table A1), and a section describing visual and audio observations in Newark Valley (Appendix A.3).

A.1. Los Alamos National Laboratory (LANL) Deployment photos (DAS)

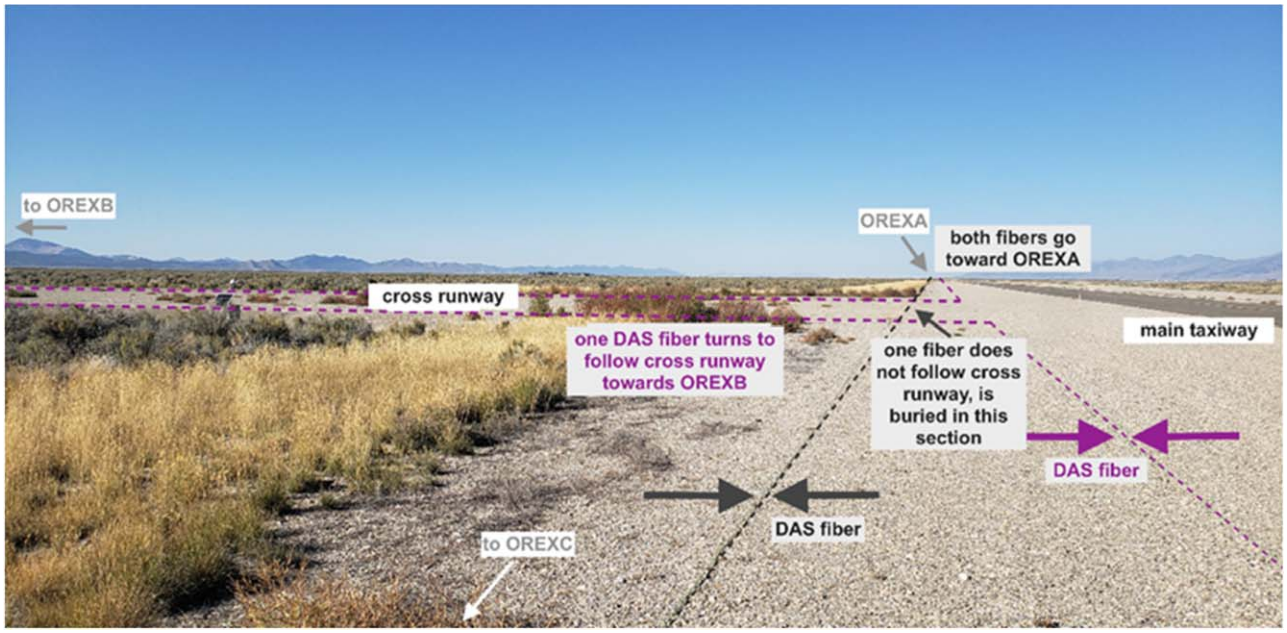

Figure A1. DAS fiber deployment at the Eureka Airport (photo credit: C. Carr).

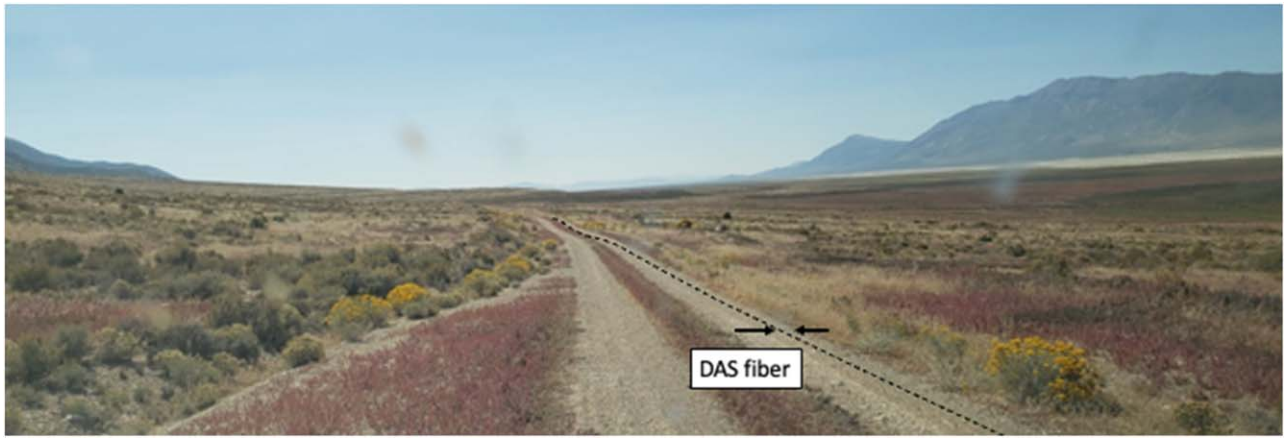

Figure A2. DAS fiber deployment in Newark Valley (photo credit: C. Carr).

A.2. Deployment Photos (DAS)

Figure A3. GPS ground station: Rex-2 (photo credit: R. Hasser).

A.3. Visual and Audio Observations in Newark Valley

In preparation for observing the reentry on the morning of 2023 September 24 in Newark Valley, two team members stood at the trailer containing the DAS interrogator unit to monitor operation during the overflight. One team member sat about 50 m to the north–northwest of the trailer, and one team member lay on the ground about 60 m to the north of the trailer. The team members maintained a quiet observation time from 07:35 AM to 08:10 AM local (14:35–15:10 UTC 2023 September 24) in sunny weather. While conditions were calm earlier in the morning, as the Sun rose in the valley, the wind increased such that during the quiet observation time observers described the wind as breezy. During the quiet observation time, team members observed several airplanes, bird noise, and various wind noises. At the airport, the two team members were outside the hangar and noted that the weather was sunny and slightly windy. The airport observers noted that traffic noise from the nearby highway was present during the reentry time frame.

One team member out of six likely saw the SRC. The team member (Carr) lying on the ground in Newark Valley observed a very bright whitish-yellow streaking flash. They estimated afterward that the streak covered about 5°, starting nearly vertically overhead and moving roughly toward the northeast. They estimated the time as 07:43:06 AM local (14:43:06 UTC) based on counting seconds since the last check of their GPS watch; they did not look at the watch at the time to maintain visual observation overhead. The other three team members in Newark Valley did not see the capsule. Team members at the airport reported that they had no visual observations of the capsule.

Most team members in Newark Valley and at Eureka Airport heard a sound, though perceptions of the sound and direction of sound origin varied. Four observers in Newark Valley heard a double boom; Carr recorded the time as 07:45:52 AM local (14:45:52 UTC), and other observers recorded the time to the minute as 07:45 AM local (14:45 UTC). Newark Valley observers perceived the sound as coming from the east (two observers), southwest (one observer), and northwest (one observer). The four Newark observers agreed that the sound was distinct and unmistakable given the quiet conditions but could have been missed if a loud conversation had been happening. At the airport, one team member heard a faint "pop" sound (time not recorded).

Carr recorded a video (duration 35 minutes, 20 s) with their personal cell phone, starting just after 07:35:00 AM local time (14:35 UTC) on 2023 September 24. Timing was determined by their personal GPS-enabled smart watch, and the video timing is within a second but slightly behind the time as recorded by the watch at the start of the video. Timing resolution is limited by the watch and phone. A clip from the video is included in a .tar.gz package; the clip begins at 07:45:40 AM local (14:45:40 UTC) and ends at 07:46:00 AM local (14:46:00 UTC). A double boom is audible about 11 s into the clip, corresponding to 07:45:51 AM local (14:45:51 UTC). This is consistent with a written observation by Carr of an audible double boom at 07:45:52 AM local (14:45:52 UTC) based on the watch. The SRC is not visible in the recording.

A.4. Signal Detection Metadata

Table A1
Detection Times for LANL Seismometers, Infrasound Sensors, the DAS Spool near OREXF, Human Observers, and a Cell Phone

Instrument or Observer	Signal Notes	Detection Time (Local) on 2023 Sep 24	Detection Time (UTC) on 2023 Sep 24	Latitude (deg N)	Longitude (deg E)	Distance to Trajectory
OREXA—infrasound sensor	N-wave	45:57.4	45:57.4	39.6109883	−116.002932	5.6 km
OREXA—seismometer	impulsive arrival with coda	45:57.5	45:57.5	39.6109883	−116.002932	5.6 km
OREXB—infrasound sensor	N-wave	45:57.5	45:57.5	39.60899	−116.011737	5.6 km
OREXB—seismometer	impulsive arrival with coda	45:57.6	45:57.6	39.60899	−116.011737	5.6 km
OREXC—infrasound sensor	N-wave	45:57.7	45:57.7	39.6040433	−116.004643	6.3 km
OREXC—seismometer	impulsive arrival with coda	45:57.8	45:57.8	39.6040433	−116.004643	6.3 km
OREXD—infrasound sensor	N-wave	45:51.6	45:51.6	39.7372017	−115.674093	1.8 km
OREXD—seismometer	impulsive arrival with coda	45:51.6	45:51.6	39.7372017	−115.674093	1.8 km
OREXE—infrasound sensor	N-wave	45:52.5	45:52.5	39.7043	−115.676033	5.2 km
OREXE—seismometer	impulsive arrival with coda	45:52.5	45:52.5	39.7043	−115.676033	5.2 km
OREXF—infrasound sensor	N-wave	45:53.3	45:53.3	39.6858783	−115.676975	7.1 km
OREXF—seismometer	impulsive arrival with coda	45:53.3	45:53.3	39.6858783	−115.676975	7.1 km
DAS spool near OREXF	peak in strain	45:53.4	45:53.4	39.6875	−115.67696	7.1 km
Chris Carr	visual bright streak	7:43:06 (estimated)	14:43:06 (estimated)	39.7516	115.6736	0.3 km
Chris Carr	audible double boom	07:45:52	14:45:52	39.7516	115.6736	0.3 km
Chris Carr cell phone	audible double boom	07:45:51	14:45:51	39.7516	115.6736	0.3 km
Carly Donahue	audible double boom	07:45	14:45	39.7511	−115.6734	0.4 km
Luke Beardslee	audible double boom	07:45	14:45	39.7511	−115.6734	0.4 km
Lisa Danielson	audible double boom	07:45	14:45	39.7515	−115.6737	0.4 km
Loïc Viens	audible faint pop	not recorded	not recorded	39.600158	−116.0058	6.6 km

Note. We manually picked arrivals on unfiltered data because the SNR is so large. For infrasound detection, we chose the corner at the start of the increase in pressure of the incoming N-wave. For the seismic records, we pick the corresponding corner at the start of the rise toward the first high-SNR peak amplitude on the vertical channel. For the DAS detection, we pick the corresponding corner at the start of the rise toward the maximum peak in strain. Ground distance (last column) represents the distance measured along a perpendicular back azimuth to the closest ground path of the nominal trajectory.

A.5. Johns Hopkins University (JHU)

Deployment Photos

Figure A4. One of the seismic nodes deployed by JHU at the Beans Flat Rest Area (photo credit: B. Fernando).

A.6. Kochi University of Technology (KUT)

Signal Detection

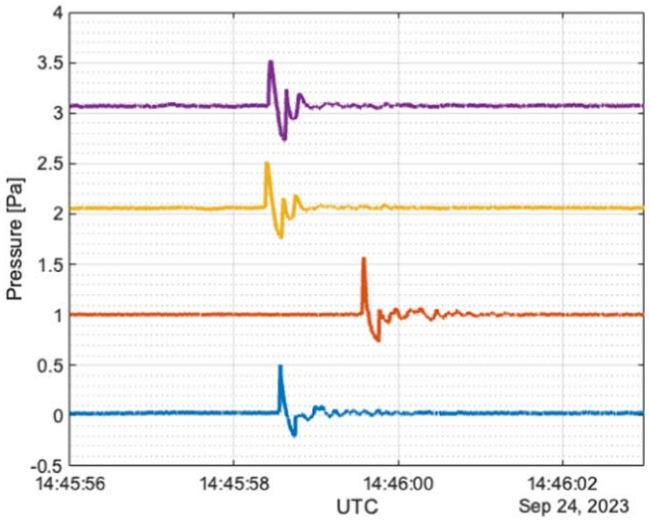

Figure A5. The signals recorded by the INF04 sensors deployed at EUE by KUT.

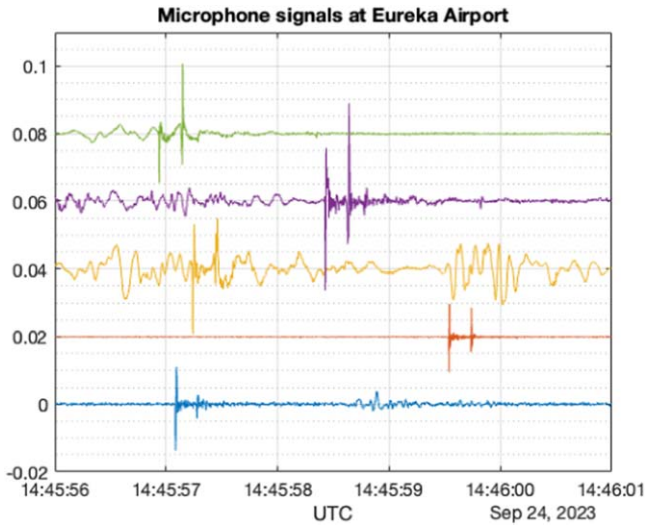

Figure A6. The signals recorded by microphones at EUE.

A.7. Oklahoma State University (OSU)

Deployment Photos

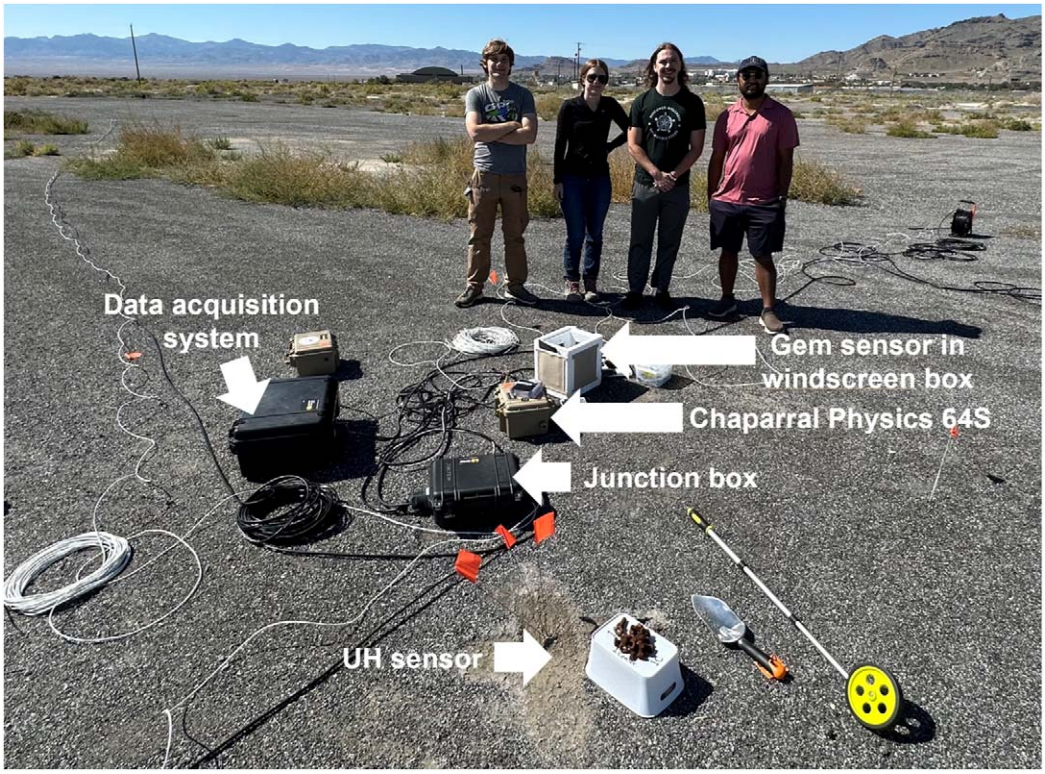

Figure A7. OSU Team (left to right: Douglas Fox, Kate Spillman, Trevor Wilson, and Real KC) at the Wendover Airport near the central location where four different sensors were colocated (Chaparral Physics 64s, GEM, WERD ISSM23, and RedVox deployed by the University of Hawaii). Photo credit: M. Garcés.

Figure A8. (a) Photo of the four Chaparral Physics 64s sensors in their cases before the OSIRIS-REx SRC reentry deployment. (b) One of the Chaparral Physics sensors deployed near a RedVox sensor deployed by UH (photo credit: B. Elbing).

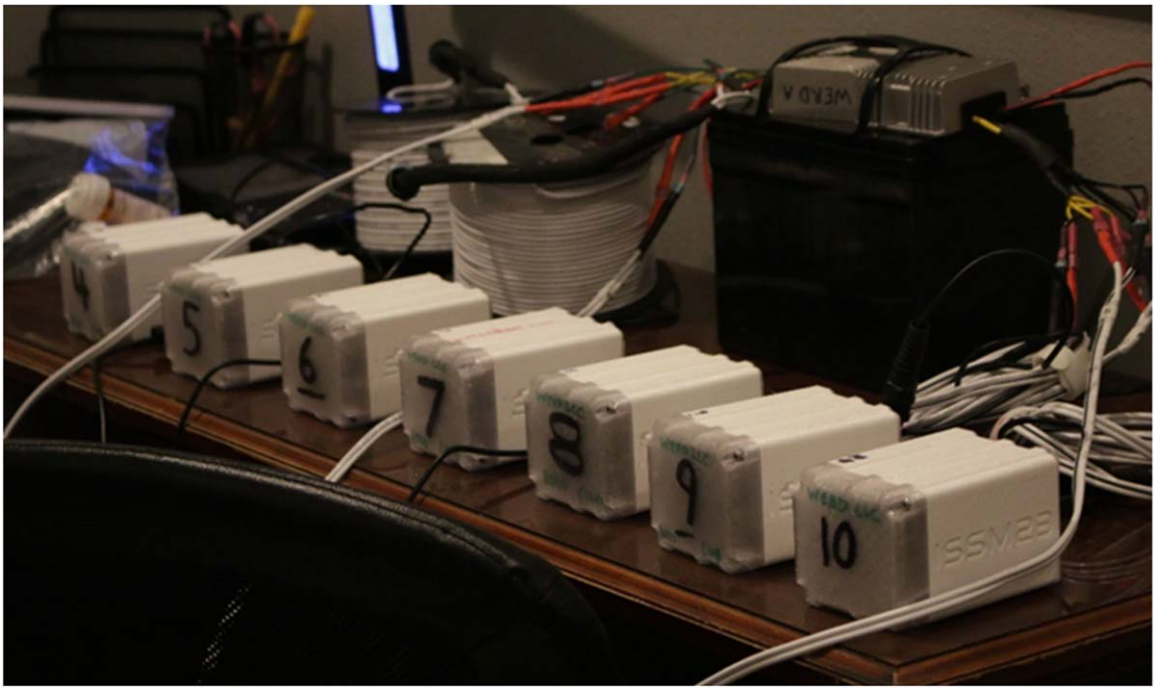

Figure A9. Picture of the seven WERD ISSM23 sensors being tested the night before the deployment for the OSIRIS-REx SRC reentry deployment (photo credit: B. Elbing).

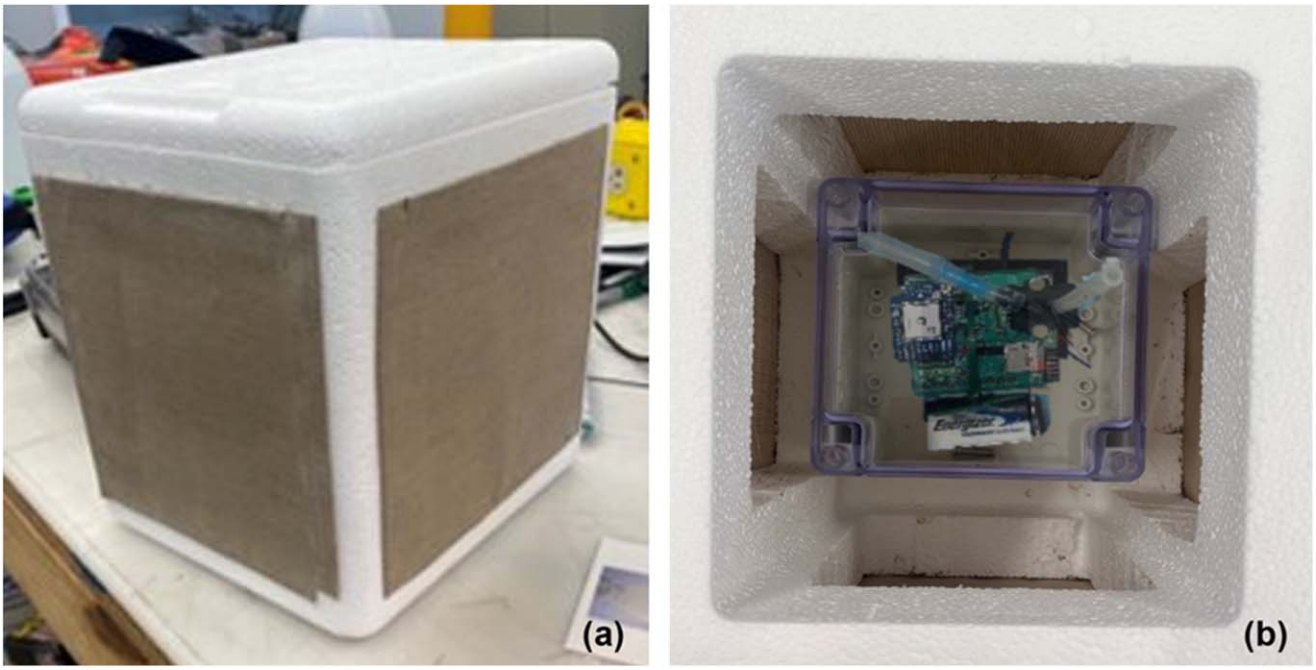

Figure A10. (a) Picture of one of the windscreen boxes (Swaim et al. 2023) that housed a GEM sensor. (b) View from above with the cover removed showing a single GEM sensor held within an enclosure and positioned within the windscreen box (photo credit: B. Elbing).

A.8. Signal Detection

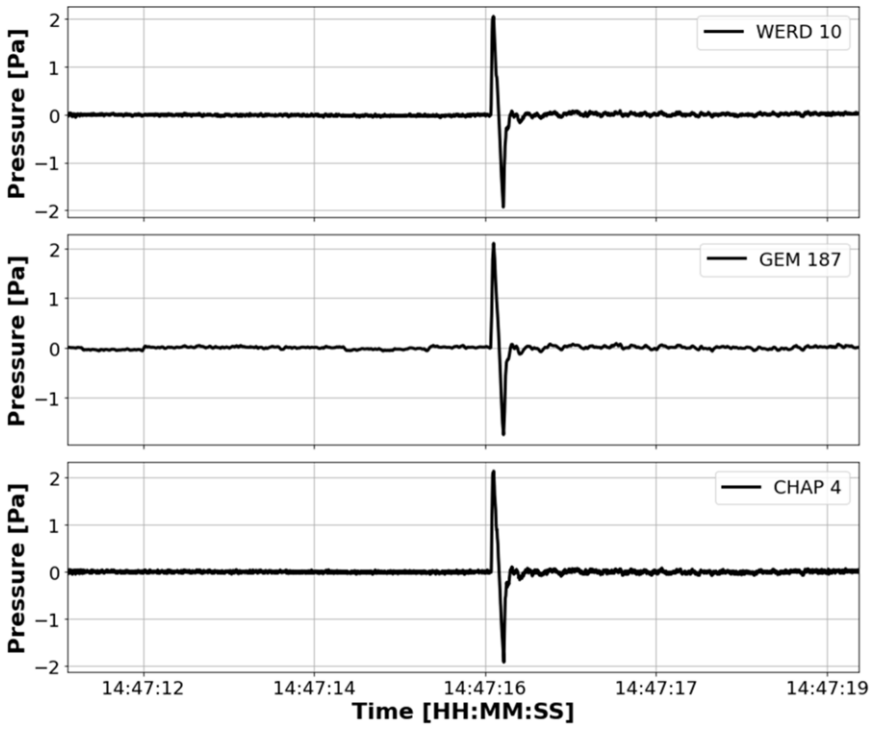

Figure A11. Signal detection at the West Wendover Airport, Utah. The figure shows a comparison between the three sensor types used.

A.9. South Methodist University (SMU)

Signal Detection

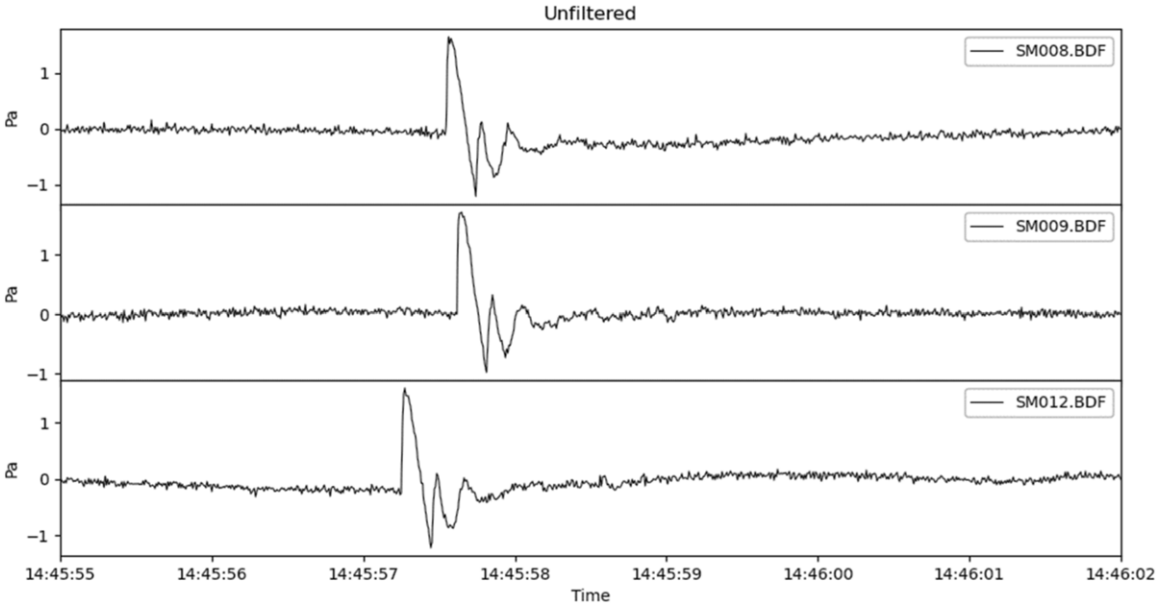

Figure A12. Signal detection at the Eureka Airport, Nevada. The time series shown are unfiltered. Time is shown in UTC.

A.10. University of Hawaii (UH)

Signal Detections

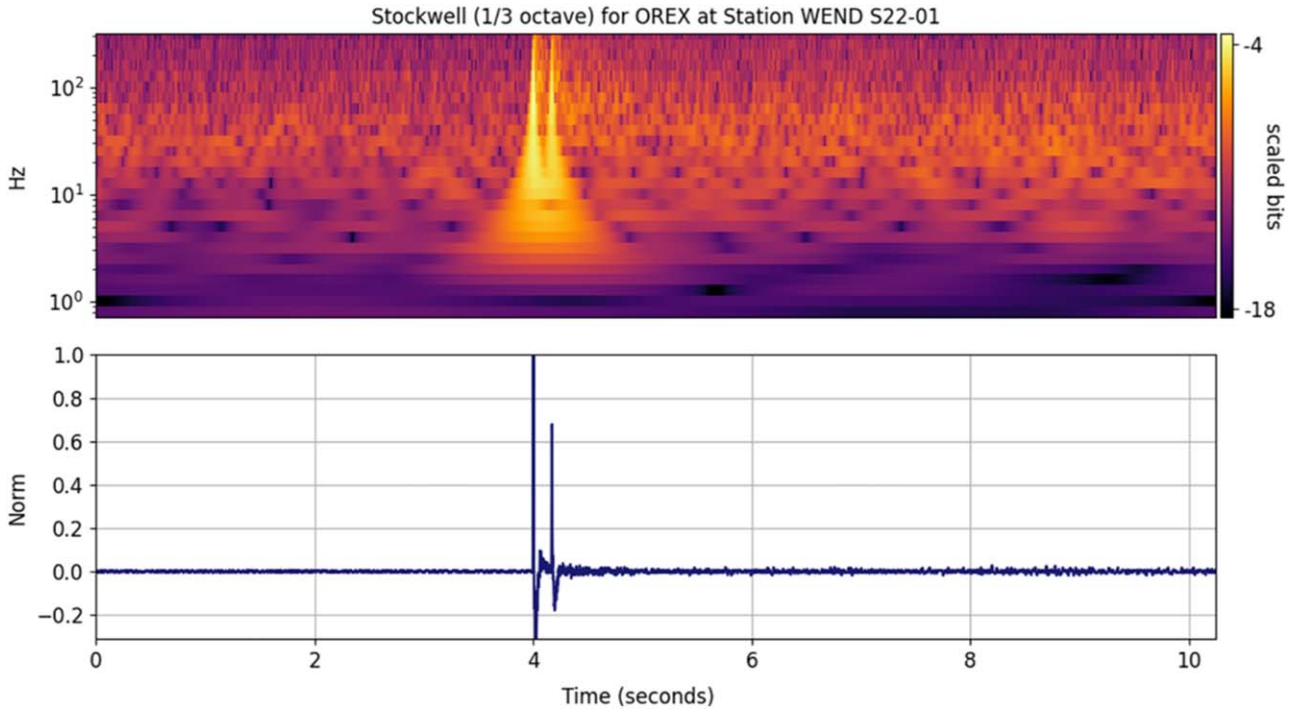

Figure A13. Signal detection at the West Wendover Airport, Utah. The time series in the bottom panel shows the smartphone microphone equivalent high-pass filter response of the N-wave; the time between the two distinct peaks is the N-wave duration. The top panel shows the multiresolution time-frequency representation of the signal using a Stockwell transform (Garces 2023) and showing the lower-frequency components of the N-wave. All channels of the Wendover array showed nearly identical waveforms time-shifted by their arrival time.

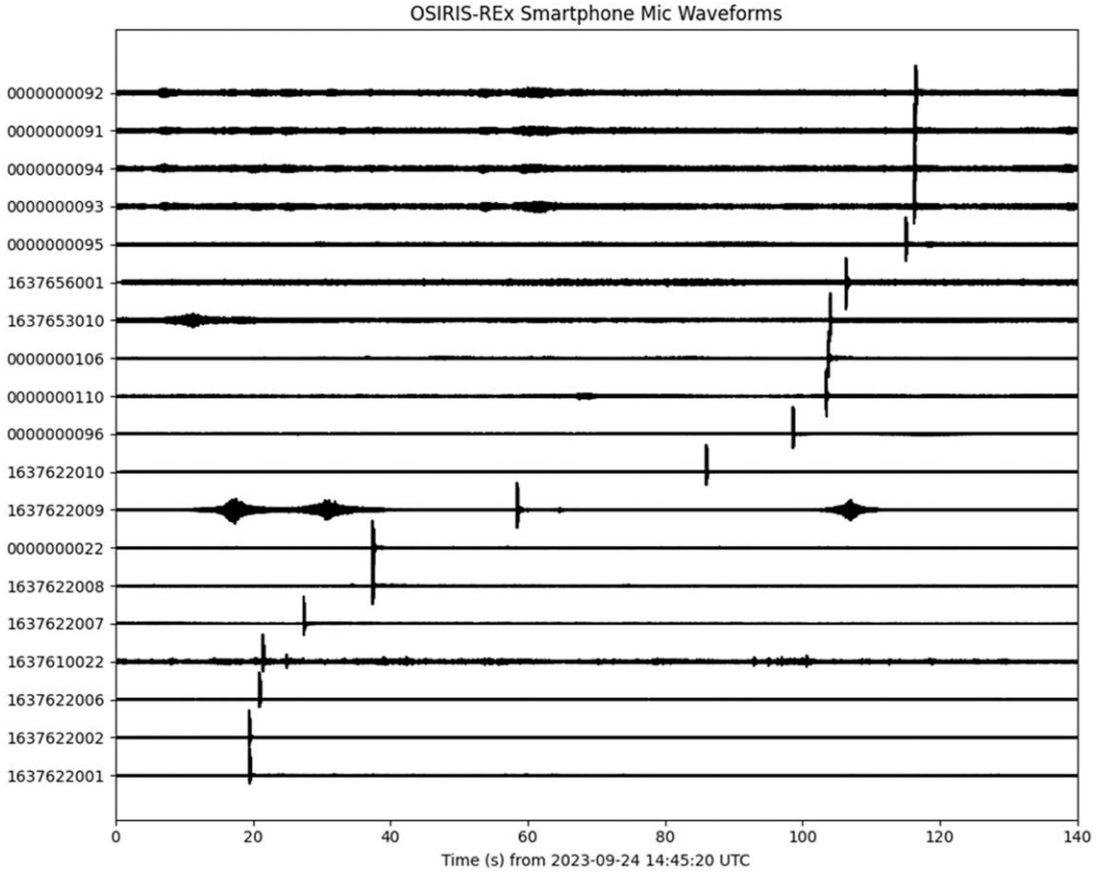

Figure A14. Detections made by smartphones, ordered by arrival time. The arrival waveforms and spectra are similar to those in Figure A13, but the N-wave duration depends on the source height and speed. The timing of the arrivals corresponds to the time of closest approach of the source plus the time it would take to reach the station. This arrival pattern is only possible from hypersonic and supersonic sources.

A.11. University of Memphis (UM)

Figure A15. University of Memphis seismoacoustic array experiment. Yellow triangles show the location of the three-component seismic nodes in the Golay 3 × 6 array configuration (A1–A18). Red triangles show the center infrasound instrument and colocated three-component seismic node for the western and eastern infrasound arrays (A19 + IW1, A20 + IE1). Green triangles show locations for infrasound microphones. Green lines show locations for the P and SH refraction profiles near the western and eastern infrasound arrays. The red lines show the boundary of the airport property.

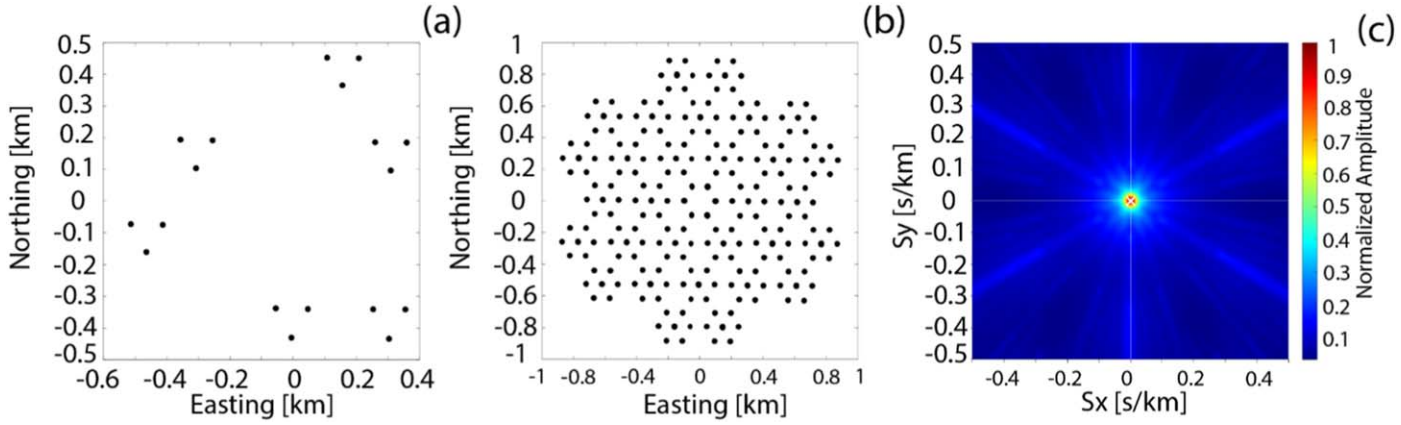

Figure A16. Geometry and response of the Golay 3 × 6 Array. (a) The OSIRIS-REx array design. (b) The co-array, which consists of distances and azimuths between all pairs of stations of the array. (c) The broadband array response for a vertically incident plane wave for the frequency band 0.25–35 Hz.

Appendix B

Table B1 lists the infrasound instrumentation metadata. The table data are also available in the machine-readable format online.

Table B1
Infrasound Instrument Installation Data

Institution	Instrument Field Name	Instrument Type	Sampling Rate (Hz)	Location	Lat (N) (deg)	Lon (E) (deg)	Comments
SNL	C1	Gem	100	Utah	39.92841	−113.99949	Single sensor
SNL	C2	Gem	100	Utah	39.97127	−113.97749	Single sensor
SNL	C3	Gem	100	Utah	40.01614	−113.97312	Single sensor
SNL	C4	Gem	100	Utah	40.006113	−113.9766	Single sensor
SNL	C5	Gem	100	Utah	40.10518	−113.97008	Single sensor
SNL	C6	Gem	100	Utah	40.1518	−113.98394	Single sensor
SNL	C7	Gem	100	Utah	40.17377	−113.99698	Single sensor
SNL	C8	Gem	100	Utah	40.19454	−113.98697	Single sensor
SNL	C9	Gem	100	Utah	40.21743	−113.99005	Single sensor
SNL	C10	Gem	100	Utah	40.24075	−113.99157	Single sensor
SNL	C11	Gem	100	Utah	40.28813	−113.98843	Single sensor
SNL	A1	Gem	100	Eureka Airport	39.37657	−115.82061	Single sensor
SNL	A2	Gem	100	Eureka Airport	39.41789	−115.81251	Single sensor
SNL	A3	Gem	100	Eureka Airport	39.45742	−115.80031	Single sensor
SNL	A4	Gem	100	Eureka Airport	39.50356	−115.78451	Single sensor
SNL	A5	Gem	100	Eureka Airport	39.54794	−115.77042	Single sensor
SNL	A6	Gem	100	Eureka Airport	39.59715	−115.75859	Single sensor
SNL	A7	Gem	100	Eureka Airport	39.64012	−115.77885	Single sensor
SNL	A8	Gem	100	Eureka Airport	39.681	−115.7779	Single sensor
SNL	A9	Gem	100	Eureka Airport	39.72717	−115.76785	Single sensor
SNL	A10	Gem	100	Eureka Airport	39.74884	−115.77333	Single sensor
SNL	A11	Gem	100	Eureka Airport	39.77546	−115.76523	Single sensor
SNL	A12	Gem	100	Eureka Airport	39.81548	−115.75109	Single sensor
SNL	A13	Gem	100	Eureka Airport	39.86349	−115.73202	Single sensor
SNL	A14	Gem	100	Eureka Airport	39.91697	−115.73846	Single sensor
SNL	A15	Gem	100	Eureka Airport	39.96471	−115.74647	Single sensor
SNL	A16	Gem	100	Eureka Airport	40.01179	−115.76422	Single sensor
SNL	A17	Gem	100	Eureka Airport	40.05231	−115.77848	Single sensor
SNL	A18	Gem	100	Eureka Airport	40.09891	−115.7832	Single sensor
SNL	A19	Gem	100	Eureka Airport	40.14403	−115.75413	Single sensor
SNL	A20	Gem	100	Eureka Airport	40.19088	−115.74343	Single sensor
SNL	A21	Gem	100	Eureka Airport	40.23178	−115.70692	Single sensor
SNL	A22	Gem	100	Eureka Airport	40.26937	−115.68173	Single sensor

Table B1
(Continued)

Institution	Instrument Field Name	Instrument Type	Sampling Rate (Hz)	Location	Lat (N) (deg)	Lon (E) (deg)	Comments
SNL	T1	Gem	100		39.54136	−116.38015	Single sensor
SNL	T2	Gem	100		39.55026	−116.33675	Single sensor
SNL	T3	Gem	100		39.58732	−116.20592	Single sensor
SNL	T4	Gem	100		39.60226	−116.1448	Single sensor
SNL	T5	Gem	100		39.63018	−116.04795	Single sensor
SNL	T6	Gem	100		39.67194	−115.90301	Single sensor
SNL	T7	Gem	100		39.71323	−115.7629	Single sensor
SNL	T8	Gem	100		39.74373	−115.6735	Single sensor
SNL	T10	Gem	100		40.04763	−114.64058	Single sensor
SNL	T11	Gem	100		40.06358	−114.58548	Single sensor
SNL	T12	Gem	100		40.07789	−114.53723	Single sensor
SNL	T13	Gem	100		40.09932	−114.54961	Single sensor
SNL	T14	Gem	100		40.18212	−114.01282	Single sensor
SNL	HA1-W	Hyperion	100		39.61691	−115.99818	Array
SNL	HA1-E	Hyperion	100		39.61691	−115.99764	Array
SNL	HA1-N	Hyperion	100		39.60727	−115.99791	Array
SNL	HA1-C	Hyperion	100		39.61705	−115.99794	Array
SNL	HA2-E	Hyperion	100		39.63933	−115.78173	Array
SNL	HA2-W	Ultra Light	100		39.63933	−115.78227	Array
SNL	HA2-C	Ultra Light	100		39.63945	−115.78200	Array
SNL	HA2-N	Hyperion	100		39.63969	−115.78200	Array
SNL	HA3-W	Hyperion	100		39.54036	−115.77476	Array
SNL	HA3-C	Hyperion	100		39.54048	−115.77450	Array
SNL	HA3-E	Hyperion	100		39.54036	−115.77423	Array
SNL	HA3-N	Hyperion	100		39.54072	−115.7745	Array
LANL	OREXA	Hyperion 3000	200		39.6109883	−116.002932	Single sensor
LANL	OREXB	Hyperion 3000	200		39.60899	−116.011737	Single sensor
LANL	OREXC	Hyperion 3000	200		39.6040433	−116.004643	Single sensor
LANL	OREXD	Hyperion 3000	200		39.7372017	−115.674093	Single sensor
LANL	OREXE	Hyperion 3000	200		39.7043	−115.676033	Single sensor
LANL	OREXF	Hyperion 3000	200		39.6858783	−115.676975	Single sensor
LANL	OREX1, e1	Hyperion IFS-3000	100	Price, UT	39.4751582	−110.7433235	Array
LANL	OREX1, e2	Hyperion IFS-3000	100	Price, UT	39.475359	−110.7451219	Array
LANL	OREX1, e3	Hyperion IFS-3000	100	Price, UT	39.4739251	−110.7449485	Array
LANL	OREX1, e4	Hyperion IFS-3000	100	Price, UT	39.474677	−110.7442959	Array
LANL	OREX3, e1	Hyperion IFS-3000	100	St. George, UT	37.0151557	−113.616179	Array
LANL	OREX3, e2	Hyperion IFS-3000	100	St. George, UT	37.0149832	−113.6170342	Array
LANL	OREX3, e3	Hyperion IFS-3000	100	St. George, UT	37.0155959	−113.6171397	Array

Table B1
(Continued)

Institution	Instrument Field Name	Instrument Type	Sampling Rate (Hz)	Location	Lat (N) (deg)	Lon (E) (deg)	Comments
LANL	OREX3, e4	Hyperion IFS-3000	100	St. George, UT	37.0162369	−113.6170218	Array
LANL	OREX3, e5	Hyperion IFS-3000	100	St. George, UT	37.0160341	−113.6162266	Array
LANL	OREX3, e6	Hyperion IFS-3000	100	St. George, UT	37.0155697	−113.6161785	Array
LANL	OREX2, e1	Hyperion IFS-3000	500	NNSS, NV	37.224998	−116.149168	Array
LANL	OREX2, e2	Hyperion IFS-3000	500	NNSS, NV	37.223915	−116.149249	Array
LANL	OREX2, e3	Hyperion IFS-3000	500	NNSS, NV	37.223589	−116.148195	Array
LANL	OREX2, e4	Hyperion IFS-3000	500	NNSS, NV	37.224247	−116.1488	Array
UM	IW1	VLF Designs IAM-1	1000	Eureka Airport	39.61159286	−116.004319	Array
UM	IW2	VLF Designs IAM-1	1000	Eureka Airport	39.61172807	−116.0040416	Array
UM	IW3	VLF Designs IAM-1	1000	Eureka Airport	39.61178112	−116.0045212	Array
UM	IW4	VLF Designs IAM-1	1000	Eureka Airport	39.61133569	−116.0043187	Array
UM	IE1	VLF Designs IAM-1	1000	Eureka Airport	39.61150004	−115.997155	Array
UM	IE2	VLF Designs IAM-1	1000	Eureka Airport	39.61165862	−115.9968662	Array
UM	IE3	VLF Designs IAM-1	1000	Eureka Airport	39.61124095	−115.9972107	Array
UM	IE4	VLF Designs IAM-1	1000	Eureka Airport	39.61162776	−115.9974629	Array
KUT		microphone		Eureka Airport	39.6166	−115.9986	Single sensor
KUT		microphone		Eureka Airport	39.6165	−115.9974	Single sensor
KUT		INF04	100	Eureka Airport	39.6175	−115.9974	Array
KUT		INF04	100	Eureka Airport	39.6175	−115.9986	Array
KUT		INF04	100	Eureka Airport	39.6138	−116.0046	Array
KUT		microphone		Eureka Airport	39.6138	−116.0046	
KUT		INF04	100	Eureka Airport	39.5893	−116.0049	Array
KUT		microphone		Eureka Airport	39.5893	−116.0049	
BSU	JDSA1	GEM, Infrasound Loggers 1.01	100	Southwest Idaho	43.12185907	−116.7856059	Array
BSU	JDSA2	GEM, Infrasound Loggers 1.01	100	Southwest Idaho	43.12192087	−116.7855215	Array
BSU	JDSA3	GEM, Infrasound Loggers 1.01	100	Southwest Idaho	43.12178317	−116.7855284	Array
BSU	JDSA4	GEM, Infrasound Loggers 1.01	100	Southwest Idaho	43.12181649	−116.7856906	Array
BSU	JDSB1	GEM, Infrasound Loggers 1.01	100	Idaho	43.12157218	−116.7879959	Array
BSU	JDSB2	GEM, Infrasound Loggers 1.01	100	Idaho	43.12160936	−116.7879871	Array
BSU	JDSB3	GEM, Infrasound Loggers 1.01	100	Idaho	43.12155341	−116.7879649	Array
BSU	JDSB4	GEM, Infrasound Loggers 1.01	100	Idaho	43.12156295	−116.788055	Array
BSU	JDNB1	GEM, Infrasound Loggers 1.03	100	Idaho	43.12543365	−116.7875822	Array
BSU	JDNB2		100	Idaho	43.12547297	−116.7875298	Array

Table B1
(Continued)

Institution	Instrument Field Name	Instrument Type	Sampling Rate (Hz)	Location	Lat (N) (deg)	Lon (E) (deg)	Comments
		GEM, Infrasound Loggers 1.04					
BSU	JDNB3	GEM, Infrasound Loggers 1.05	100	Idaho	43.12541687	−116.7875265	Array
BSU	JDNB4	GEM, Infrasound Loggers 1.06	100	Idaho	43.12543144	−116.7876213	Array
BSU	TOP01	GEM, Infrasound Loggers 1.08	100	Idaho	43.12550998	−116.8013974	Array
BSU	TOP02	GEM, Infrasound Loggers 1.09	100	Idaho	43.12560459	−116.8015603	Array
BSU	TOP03	GEM, Infrasound Loggers 1.10	100	Idaho	43.12572902	−116.8017619	Array
BSU	TOP04	GEM, Infrasound Loggers 1.11	100	Idaho	43.12584698	−116.8019344	Array
BSU	TOP05	GEM, Infrasound Loggers 1.12	100	Idaho	43.12596533	−116.8020799	Array
BSU	TOP06	GEM, Infrasound Loggers 1.13	100	Idaho	43.12606252	−116.8021671	Array
BSU	TOP07	GEM, Infrasound Loggers 1.14	100	Idaho	43.12620928	−116.8023396	Array
BSU	TOP08	GEM, Infrasound Loggers 1.15	100	Idaho	43.12634974	−116.8024834	Array
BSU	TOP09	GEM, Infrasound Loggers 1.16	100	Idaho	43.12643686	−116.8026145	Array
BSU	TOP10	GEM, Infrasound Loggers 1.17	100	Idaho	43.12655189	−116.8027244	Array
BSU	TOP11	GEM, Infrasound Loggers 1.18	100	Idaho	43.12666905	−116.8028433	Array
BSU	TOP12	GEM, Infrasound Loggers 1.19	100	Idaho	43.12677948	−116.8030524	Array
BSU	TOP13	GEM, Infrasound Loggers 1.20	100	Idaho	43.12674003	−116.803228	Array
BSU	TOP14	GEM, Infrasound Loggers 1.21	100	Idaho	43.1266241	−116.8033681	Array
BSU	TOP15	GEM, Infrasound Loggers 1.22	100	Idaho	43.12663831	−116.8035886	Array
BSU	TOP16	GEM, Infrasound Loggers 1.23	100	Idaho	43.1265124	−116.8036435	Array
BSU	TOP17	GEM, Infrasound Loggers 1.24	100	Idaho	43.1264339	−116.8038132	Array
BSU	TOP18	GEM, Infrasound Loggers 1.25	100	Idaho	43.12634576	−116.8039767	Array
BSU	TOP19	GEM, Infrasound Loggers 1.26	100	Idaho	43.12624488	−116.804096	Array
BSU	TOP20	GEM, Infrasound Loggers 1.27	100	Idaho	43.12617945	−116.8042248	Array
BSU	TOP21	GEM, Infrasound Loggers 1.28	100	Idaho	43.1260073	−116.8041484	Array

Table B1
(Continued)

Institution	Instrument Field Name	Instrument Type	Sampling Rate (Hz)	Location	Lat (N) (deg)	Lon (E) (deg)	Comments
BSU	TOP22	GEM, Infrasound Loggers 1.29	100	Idaho	43.12583556	−116.8039579	Array
BSU	TOP23	GEM, Infrasound Loggers 1.30	100	Idaho	43.12569345	−116.8037969	Array
BSU	TOP24	GEM, Infrasound Loggers 1.31	100	Idaho	43.12556656	−116.8036705	Array
BSU	TOP25	GEM, Infrasound Loggers 1.32	100	Idaho	43.12546093	−116.8035615	Array
BSU	TOP26	GEM, Infrasound Loggers 1.33	100	Idaho	43.1252966	−116.8034484	Array
BSU	TOP27	GEM, Infrasound Loggers 1.34	100	Idaho	43.1251737	−116.8032903	Array
BSU	TOP28	GEM, Infrasound Loggers 1.35	100	Idaho	43.12508251	−116.8030776	Array
BSU	TOP29	GEM, Infrasound Loggers 1.36	100	Idaho	43.12494683	−116.8029506	Array
BSU	TOP30	GEM, Infrasound Loggers 1.37	100	Idaho	43.12481786	−116.8028627	Array
BSU	TOP31	GEM, Infrasound Loggers 1.38	100	Idaho	43.12469091	−116.8027794	Array
BSU	TOP32	GEM, Infrasound Loggers 1.39	100	Idaho	43.12472395	−116.802606	Array
BSU	TOP33	GEM, Infrasound Loggers 1.40	100	Idaho	43.12478858	−116.8024612	Array
BSU	TOP34	GEM, Infrasound Loggers 1.41	100	Idaho	43.12490261	−116.8023562	Array
BSU	TOP35	GEM, Infrasound Loggers 1.42	100	Idaho	43.12498012	−116.8022125	Array
BSU	TOP36	GEM, Infrasound Loggers 1.43	100	Idaho	43.12508385	−116.8020925	Array
BSU	TOP37	GEM, Infrasound Loggers 1.44	100	Idaho	43.1251528	−116.8019492	Array
BSU	TOP38	GEM, Infrasound Loggers 1.45	100	Idaho	43.12523129	−116.8018297	Array
BSU	TOP39	GEM, Infrasound Loggers 1.46	100	Idaho	43.12535378	−116.8016928	Array
BSU	TOP40	GEM, Infrasound Loggers 1.47	100	Idaho	43.12539279	−116.8015533	Array
BSU	TOP41	GEM, Infrasound Loggers 1.48	100	Idaho	43.12550101	−116.8019804	Array
BSU	TOP42	GEM, Infrasound Loggers 1.49	100	Idaho	43.12544889	−116.8022824	Array
BSU	TOP43	GEM, Infrasound Loggers 1.50	100	Idaho	43.12556576	−116.8025817	Array
BSU	TOP44	GEM, Infrasound Loggers 1.51	100	Idaho	43.12561661	−116.8028346	Array
TDA	AA 1	TDA sensor	200	Eureka Airport	39.61752711	−115.9986176	Large N-array

Table B1
(Continued)

Institution	Instrument Field Name	Instrument Type	Sampling Rate (Hz)	Location	Lat (N) (deg)	Lon (E) (deg)	Comments
TDA	AA 2	TDA sensor	200	Eureka Airport	39.61752834	−115.9986619	Large N-array
TDA	AA 3	TDA sensor	200	Eureka Airport	39.61754657	−115.998621	Large N-array
TDA	AA 4	TDA sensor	200	Eureka Airport	39.61752664	−115.9985874	Large N-array
TDA	AA 5	TDA sensor	200	Eureka Airport	39.61749151	−115.9986127	Large N-array
TDA	AB 1	TDA sensor	200	Eureka Airport	39.61752118	−115.9984251	Large N-array
TDA	AB 2	TDA sensor	200	Eureka Airport	39.6175235	−115.9984637	Large N-array
TDA	AB 3	TDA sensor	200	Eureka Airport	39.61754496	−115.9984252	Large N-array
TDA	AB 4	TDA sensor	200	Eureka Airport	39.61752115	−115.9983805	Large N-array
TDA	AB 5	TDA sensor	200	Eureka Airport	39.61748155	−115.9984185	Large N-array
TDA	AC 1	TDA sensor	200	Eureka Airport	39.61751905	−115.9982339	Large N-array
TDA	AC 2	TDA sensor	200	Eureka Airport	39.61753585	−115.9982558	Large N-array
TDA	AC 3	TDA sensor	200	Eureka Airport	39.61753085	−115.9982101	Large N-array
TDA	AC 4	TDA sensor	200	Eureka Airport	39.61750178	−115.9982132	Large N-array
TDA	AC 5	TDA sensor	200	Eureka Airport	39.61749968	−115.9982592	Large N-array
TDA	AD 1	TDA sensor	200	Eureka Airport	39.61752679	−115.9980451	Large N-array
TDA	AD 2	TDA sensor	200	Eureka Airport	39.61753938	−115.9980647	Large N-array
TDA	AD 3	TDA sensor	200	Eureka Airport	39.61754099	−115.9980263	Large N-array
TDA	AD 4	TDA sensor	200	Eureka Airport	39.61750802	−115.9980294	Large N-array
TDA	AD 5	TDA sensor	200	Eureka Airport	39.61750673	−115.9980685	Large N-array
TDA	AE 1	TDA sensor	200	Eureka Airport	39.61752578	−115.9978596	Large N-array
TDA	AE 2	TDA sensor	200	Eureka Airport	39.61754488	−115.9978823	Large N-array
TDA	AE 3	TDA sensor	200	Eureka Airport	39.61754334	−115.997839	Large N-array
TDA	AE 4	TDA sensor	200	Eureka Airport	39.61750814	−115.9978419	Large N-array
TDA	AE 5	TDA sensor	200	Eureka Airport	39.61750734	−115.9978785	Large N-array
TDA	AG 1	TDA sensor	200	Eureka Airport	39.61750459	−115.9973942	Large N-array
TDA	AG 2	TDA sensor	200	Eureka Airport	39.61752665	−115.9974294	Large N-array
TDA	AG 3	TDA sensor	200	Eureka Airport	39.61752726	−115.9973741	Large N-array
TDA	AG 4	TDA sensor	200	Eureka Airport	39.61748733	−115.9973661	Large N-array
TDA	AG 5	TDA sensor	200	Eureka Airport	39.61747382	−115.9974161	Large N-array
TDA	AO 1	TDA sensor	200	Eureka Airport	39.61729741	−115.9973552	Large N-array
TDA	AO 2	TDA sensor	200	Eureka Airport	39.61732845	−115.9973682	Large N-array
TDA	AO 3	TDA sensor	200	Eureka Airport	39.61731556	−115.9973271	Large N-array
TDA	AO 4	TDA sensor	200	Eureka Airport	39.61727182	−115.9973251	Large N-array
TDA	AO 5	TDA sensor	200	Eureka Airport	39.61728508	−115.9973932	Large N-array
TDA	AL 1	TDA sensor	200	Eureka Airport	39.61731577	−115.9980295	Large N-array
TDA	AL 2	TDA sensor	200	Eureka Airport	39.61733268	−115.9980542	Large N-array
TDA	AL 3	TDA sensor	200	Eureka Airport	39.61733605	−115.998002	Large N-array
TDA	AL 4	TDA sensor	200	Eureka Airport	39.61729622	−115.9980052	Large N-array

Table B1
(Continued)

Institution	Instrument Field Name	Instrument Type	Sampling Rate (Hz)	Location	Lat (N) (deg)	Lon (E) (deg)	Comments
TDA	AL 5	TDA sensor	200	Eureka Airport	39.61729946	−115.9980556	Large N-array
TDA	AH 1	TDA sensor	200	Eureka Airport	39.61731637	−115.9985973	Large N-array
TDA	AH 2	TDA sensor	200	Eureka Airport	39.61730556	−115.9986386	Large N-array
TDA	AH 3	TDA sensor	200	Eureka Airport	39.61735896	−115.9985988	Large N-array
TDA	AH 4	TDA sensor	200	Eureka Airport	39.61732078	−115.9985483	Large N-array
TDA	AH 5	TDA sensor	200	Eureka Airport	39.61727528	−115.9985985	Large N-array
TDA	AP 1	TDA sensor	200	Eureka Airport	39.6171509	−115.9985694	Large N-array
TDA	AP 2	TDA sensor	200	Eureka Airport	39.61712029	−115.9985639	Large N-array
TDA	AP 3	TDA sensor	200	Eureka Airport	39.61714777	−115.9986103	Large N-array
TDA	AP 4	TDA sensor	200	Eureka Airport	39.61718634	−115.9985563	Large N-array
TDA	AP 5	TDA sensor	200	Eureka Airport	39.61715099	−115.9985163	Large N-array
TDA	AT 1	TDA sensor	200	Eureka Airport	39.61713803	−115.9980301	Large N-array
TDA	AT 2	TDA sensor	200	Eureka Airport	39.61711037	−115.9980552	Large N-array
TDA	AT 3	TDA sensor	200	Eureka Airport	39.61715787	−115.9980779	Large N-array
TDA	AT 4	TDA sensor	200	Eureka Airport	39.61717115	−115.9979966	Large N-array
TDA	AT 5	TDA sensor	200	Eureka Airport	39.6171214	−115.9979858	Large N-array
TDA	AW 1	TDA sensor	200	Eureka Airport	39.61711683	−115.9973592	Large N-array
TDA	AW 2	TDA sensor	200	Eureka Airport	39.61713963	−115.9973922	Large N-array
TDA	AW 3	TDA sensor	200	Eureka Airport	39.61713069	−115.9973274	Large N-array
TDA	AW 4	TDA sensor	200	Eureka Airport	39.61709491	−115.9973306	Large N-array
TDA	AW 5	TDA sensor	200	Eureka Airport	39.61709719	−115.997395	Large N-array
TDA	BE 1	TDA sensor	200	Eureka Airport	39.61689621	−115.9979975	Large N-array
TDA	BE 2	TDA sensor	200	Eureka Airport	39.61692138	−115.9979683	Large N-array
TDA	BE 3	TDA sensor	200	Eureka Airport	39.61687534	−115.9979646	Large N-array
TDA	BE 4	TDA sensor	200	Eureka Airport	39.61687088	−115.998023	Large N-array
TDA	BE 5	TDA sensor	200	Eureka Airport	39.6169141	−115.9980322	Large N-array
TDA	BB 1	TDA sensor	200	Eureka Airport	39.61696885	−115.998569	Large N-array
TDA	BB 2	TDA sensor	200	Eureka Airport	39.61697081	−115.9985362	Large N-array
TDA	BB 3	TDA sensor	200	Eureka Airport	39.61693557	−115.9985649	Large N-array
TDA	BB 4	TDA sensor	200	Eureka Airport	39.61696674	−115.9986111	Large N-array
TDA	BB 5	TDA sensor	200	Eureka Airport	39.61700185	−115.9985761	Large N-array
TDA	BI 1	TDA sensor	200	Eureka Airport	39.61678249	−115.9985538	Large N-array
TDA	BI 2	TDA sensor	200	Eureka Airport	39.61678141	−115.9985191	Large N-array
TDA	BI 3	TDA sensor	200	Eureka Airport	39.61675684	−115.9985499	Large N-array
TDA	BI 4	TDA sensor	200	Eureka Airport	39.61678143	−115.9986053	Large N-array
TDA	BI 5	TDA sensor	200	Eureka Airport	39.61681847	−115.9985575	Large N-array
TDA	BL 1	TDA sensor	200	Eureka Airport	39.61669171	−115.9979882	Large N-array
TDA	BL 2	TDA sensor	200	Eureka Airport	39.61667753	−115.9979595	Large N-array

Table B1
(Continued)

Institution	Instrument Field Name	Instrument Type	Sampling Rate (Hz)	Location	Lat (N) (deg)	Lon (E) (deg)	Comments
TDA	BL 3	TDA sensor	200	Eureka Airport	39.61667106	−115.9980087	Large N-array
TDA	BL 4	TDA sensor	200	Eureka Airport	39.61670666	−115.9980145	Large N-array
TDA	BL 5	TDA sensor	200	Eureka Airport	39.61671435	−115.9979715	Large N-array
TDA	BO 1	TDA sensor	200	Eureka Airport	39.61673257	−115.9973895	Large N-array
TDA	BO 2	TDA sensor	200	Eureka Airport	39.61671555	−115.9973527	Large N-array
TDA	BO 3	TDA sensor	200	Eureka Airport	39.61670968	−115.9974107	Large N-array
TDA	BO 4	TDA sensor	200	Eureka Airport	39.61675925	−115.997413	Large N-array
TDA	BO 5	TDA sensor	200	Eureka Airport	39.61675637	−115.9973539	Large N-array
TDA	BS 1	TDA sensor	200	Eureka Airport	39.61650194	−115.9979802	Large N-array
TDA	BS 2	TDA sensor	200	Eureka Airport	39.61648103	−115.9980106	Large N-array
TDA	BS 3	TDA sensor	200	Eureka Airport	39.61652107	−115.9980084	Large N-array
TDA	BS 4	TDA sensor	200	Eureka Airport	39.61652053	−115.9979524	Large N-array
TDA	BR 1	TDA sensor	200	Eureka Airport	39.61652715	−115.9981568	Large N-array
TDA	BR 2	TDA sensor	200	Eureka Airport	39.61649997	−115.9981276	Large N-array
TDA	BR 3	TDA sensor	200	Eureka Airport	39.61650461	−115.998182	Large N-array
TDA	BR 4	TDA sensor	200	Eureka Airport	39.61654842	−115.9981822	Large N-array
TDA	BR 5	TDA sensor	200	Eureka Airport	39.61654919	−115.9981286	Large N-array
TDA	BQ 1	TDA sensor	200	Eureka Airport	39.61653333	−115.9983295	Large N-array
TDA	BQ 2	TDA sensor	200	Eureka Airport	39.61649627	−115.9983174	Large N-array
TDA	BQ 3	TDA sensor	200	Eureka Airport	39.61652912	−115.9983727	Large N-array
TDA	BQ 4	TDA sensor	200	Eureka Airport	39.61656311	−115.998334	Large N-array
TDA	BQ 5	TDA sensor	200	Eureka Airport	39.61653614	−115.9982894	Large N-array
TDA	BP 1	TDA sensor	200	Eureka Airport	39.61654933	−115.998579	Large N-array
TDA	BP 2	TDA sensor	200	Eureka Airport	39.61654556	−115.9985301	Large N-array
TDA	BP 3	TDA sensor	200	Eureka Airport	39.61651148	−115.9985766	Large N-array
TDA	BP 4	TDA sensor	200	Eureka Airport	39.61655246	−115.9986164	Large N-array
TDA	BP 5	TDA sensor	200	Eureka Airport	39.6165886	−115.9985852	Large N-array
TDA	AX 1	TDA sensor	200	Eureka Airport	39.61646076	−115.9973911	Large N-array
TDA	AX 2	TDA sensor	200	Eureka Airport	39.61648133	−115.9974156	Large N-array
TDA	AX 3	TDA sensor	200	Eureka Airport	39.61648015	−115.9973568	Large N-array
TDA	AX 4	TDA sensor	200	Eureka Airport	39.61643304	−115.9973639	Large N-array
TDA	AX 5	TDA sensor	200	Eureka Airport	39.61643632	−115.997415	Large N-array
TDA	BT 1	TDA sensor	200	Eureka Airport	39.61645917	−115.9976089	Large N-array
TDA	BT 2	TDA sensor	200	Eureka Airport	39.61644781	−115.9975688	Large N-array
TDA	BT 3	TDA sensor	200	Eureka Airport	39.61644094	−115.9976325	Large N-array
TDA	BT 4	TDA sensor	200	Eureka Airport	39.61647984	−115.9976417	Large N-array
TDA	BT 5	TDA sensor	200	Eureka Airport	39.61648358	−115.9975813	Large N-array
UH	redvox_1173028730		800	Eureka, NV	39.60085476	−116.0061335	Single station

Table B1
(Continued)

Institution	Instrument Field Name	Instrument Type	Sampling Rate (Hz)	Location	Lat (N) (deg)	Lon (E) (deg)	Comments
UH	redvox_0000000022		800	Nevada	39.61727241	−115.9979189	Single station
UH	redvox_1637622001		800	Nevada	40.06032154	−114.525342	Single station
UH	redvox_1637622002		800	Nevada	40.06941936	−114.5299165	Single station
UH	redvox_1637622006		800	Nevada	40.1184172	−114.5319345	Single station
UH	redvox_1637622007		800	Nevada	40.22897117	−114.4351343	Single station
UH	redvox_1637622008		800	Nevada	40.35166394	−114.2376673	Single station
UH	redvox_1637622009		800	Nevada	40.47726143	−114.155499	Single station
UH	redvox_1637622010		800	Nevada	40.59260421	−114.1392218	Single station
UH	redvox_0000000096		800	Nevada	40.6452582	−114.1235271	Single station
UH	redvox_0000000095		800	Nevada	40.71097088	−114.0889773	Single station
UH	redvox_0000000094		800	West Wendover Airport	40.7278619	−114.0218836	Array
UH	redvox_0000000091		800	West Wendover Airport	40.72804373	−114.0211986	Array
UH	redvox_0000000093		800	West Wendover Airport	40.72782152	−114.0205354	Array
UH	redvox_0000000092		800	West Wendover Airport	40.728606	−114.0211872	Array
UH	redvox_1637653010		800	Nevada	40.7124639	−113.1244734	Single station
UH	redvox_0000000110		800	Clive, UT	40.70939688	−113.1214597	Single station
UH	redvox_0000000106		800	Clive, UT	40.7088681	−113.1167137	Single station
UH	redvox_1637656001		800	Clive, UT	40.7165156	−113.1127525	Single station
UH	redvox_0000000103		800	Dugway, UT	40.25711486	−112.7404369	Single station
UH	redvox_0000000104		800	Dugway, UT	40.25731765	−112.7404951	Single station
UH	redvox_1637610021		800	Nevada	39.69948222	−115.8906106	Single station
UH	redvox_1637610022		800	Eureka, NV	39.7076942	−115.8617927	Single station
INL	redvox_1637622022	Samsung S22	800	Idaho Falls, ID	43.65981128	−111.844751	Single station
INL	redvox_1637622023	Samsung S22	800	Idaho Falls, ID	43.49978502	−112.0490684	Single station
INL	redvox_1637622024	Samsung S22	800	Idaho Falls, ID	43.49979985	−112.0491303	Single station
INL	redvox_1637622025	Samsung S22	800	Idaho Falls, ID	43.50714182	−111.9710928	Single station
INL	redvox_1637622026	Samsung S22	800	Idaho Falls, ID	43.48783296	−112.0784373	Single station
INL	redvox_1637622029	Samsung S22	800	Idaho Falls, ID	43.49990583	−112.0491253	Single station
INL	redvox_1637622030	Samsung S22	800	Idaho Falls, ID	43.48782929	−112.0784318	Single station
SMU	SN10	Sapphire		Eureka Airport	39.61727	−116.00037	Array
SMU	SN12	Sapphire		Eureka Airport	39.61704	−116.0004	Array
SMU	SN09	Sapphire		Eureka Airport	39.61691	−116.00064	Array
SMU	SN08	Sapphire		Eureka Airport	39.61691	−116.0001	Array
OSU	Loc04—Center	Chaparral Physics, 64S	1000	West Wendover Airport	40.7280	−114.0212	Array
OSU	Loc03	Chaparral Physics, 64S	1000	West Wendover Airport	40.7286	−114.0211	Array

Table B1
(Continued)

Institution	Instrument Field Name	Instrument Type	Sampling Rate (Hz)	Location	Lat (N) (deg)	Lon (E) (deg)	Comments
OSU	Loc02	Chaparral Physics, 64S	1000	West Wendover Airport	40.7278	−114.0205	Array
OSU	Loc01	Chaparral Physics, 64S	1000	West Wendover Airport	40.7279	−114.0219	Array
OSU	WERD 10—center	WERD, ISSM23	400	West Wendover Airport	40.7280	−114.0212	Single sensor
OSU	WERD 9	WERD, ISSM23	400	West Wendover Airport	40.7282	−114.0210	Single sensor
OSU	WERD 7	WERD, ISSM23	400	West Wendover Airport	40.7278	−114.0213	Single sensor
OSU	WERD 5	WERD, ISSM23	400	West Wendover Airport	40.7281	−114.0214	Single sensor
OSU	WERD 3	WERD, ISSM23	400	West Wendover Airport	40.7281	−114.0218	Single sensor
OSU	WERD 6	WERD, ISSM23	400	West Wendover Airport	40.7276	−114.0219	Single sensor
OSU	WERD 4	WERD, ISSM23	400	West Wendover Airport	40.7278	−114.0222	Single sensor
OSU	GEM 185	GEM, 1.01 Flight version	100	West Wendover Airport	40.7277	−114.0208	Single sensor
OSU	GEM 186	GEM, 1.01 Flight version	100	West Wendover Airport	40.7281	−114.0208	Single sensor
OSU	GEM 187—center	GEM, 1.01 Flight version	100	West Wendover Airport	40.7280	−114.0212	Single sensor
OSU	GEM 074	GEM, 1.01 Flight version	100	West Wendover Airport	40.4924	−114.0425	Single sensor
OSU	GEM 092	GEM, 1.01 Flight version	100	West Wendover Airport	40.4254	−114.0155	Single sensor

(This table is available in its entirety in machine-readable form in the online article.)

Appendix C

Table C1 lists the seismic instrumentation metadata. The table data are also available in the machine-readable format online.

Table C1
Seismic Instrument Installation Data

Institution	Instrument Field Name	Latitude (N) (deg)	Longitude (E) (deg)	Comments
SNL	EA-S1	39.61727	−116.00026	
SNL	EA-S2	39.61551	−115.99598	
SNL	EA-S3	39.61203	−116.00454	
SNL	EA-S4	39.61013	−116.00019	
SNL	EA-S5	39.60808	−116.01050	
SNL	EA-S6	39.60755	−116.00766	
SNL	EA-S7	39.60702	−116.00482	
SNL	EA-S8	39.60623	−116.00057	
SNL	EA-S9	39.60286	−116.00646	
SNL	EA-S10	39.59980	−116.00269	
SNL	EA-S11	39.59782	−116.00742	
SNL	EA-S12	39.59347	−116.00436	
SNL	HA1-SNC	39.61702	−115.99792	Colocated with infrasound
SNL	HA1-SN	39.61727	−115.99791	Colocated with infrasound
SNL	HA2	39.63969	−115.78261	Colocated with infrasound
SNL	HA2	39.63945	−115.78200	Colocated with infrasound
SNL	HA3	39.54050	−115.77453	Colocated with infrasound
SNL	HA3	39.54073	−115.77453	Colocated with infrasound
LANL	OREXA	39.61099	−116.00293	Colocated with infrasound
LANL	OREXB	39.60899	−116.01174	Colocated with infrasound
LANL	OREXC	39.60404	−116.00464	Colocated with infrasound
LANL	OREXD	39.73720	−115.67409	Colocated with infrasound
LANL	OREXE	39.70430	−115.67603	Colocated with infrasound
LANL	OREXF	39.68588	−115.67698	Colocated with infrasound
UM	A1	39.61424	−115.99951	
UM	A2	39.61422	−115.99834	
UM	A3	39.61345	−115.99894	
UM	A4	39.61183	−115.99774	
UM	A5	39.61182	−115.99658	
UM	A6	39.61103	−115.99717	
UM	A7	39.60709	−115.99781	
UM	A8	39.60709	−115.99663	
UM	A9	39.60625	−115.99723	
UM	A10	39.60712	−116.00141	

Table C1
(Continued)

Institution	Instrument Field Name	Latitude (N) (deg)	Longitude (E) (deg)	Comments
UM	A11	39.60710	−116.00023	
UM	A12	39.60629	−116.00083	
UM	A13	39.60951	−116.00676	
UM	A14	39.60950	−116.00559	
UM	A15	39.60872	−116.00619	
UM	A16	39.61191	−116.00494	
UM	A17	39.61189	−116.00376	
UM	A18	39.61109	−116.00437	
UM	A19	39.61159	−116.00432	
UM	A20	39.61150	−115.99716	
UM	Refraction West	39.61113563	−116.00468	South end of line
UM	Refraction East	39.61096743	−115.99691	SouthWest end of line
JHU	S1	39.49957	−116.50945	Array center
JHU	S2	39.49919	−116.51052	Uprange 1
JHU	S3	9.49883	−116.51157	Uprange 2
JHU	S4	39.49844	−116.51262	Uprange 3
JHU	S5	39.49790	−116.50855	South 1
JHU	S6	39.50036	−116.50994	North 1
JHU	S7	39.50117	−116.51045	North 2
JHU	S8	39.49991	−116.50838	Downrange 1
JHU	S9	39.50027	−116.50731	Downrange 2
JHU	S10	39.50060	−116.50623	Downrange 3
JHU	S11	39.49874	−116.50920	South 2

Note. This table is available in machine-readable format.

(This table is available in its entirety in machine-readable form in the online article.)

Appendix D

Table D1 lists the GPS instruments. The table data are also available in the machine-readable format online.

Table D1
GPS Instrument Installation Data

Institution	Instrument Field Name	Latitude (N) (deg)	Longitude (E) (deg)	Elevation (m)
LANL	West Runway	39.608664	−116.011496	1811.8
LANL	Mid-North Runway	39.607281	−116.004027	1810.4
LANL	Mid-South Runway	39.603620	−116.004756	1812.0
LANL	South Runway	39.595354	−116.007202	1814.4
LANL	North Runway	39.612798	−116.002877	1810.3

ORCID iDs

Elizabeth A. Silber https://orcid.org/0000-0003-4778-1409

References

Afraimovich, E., Kosogorov, E., Perevalova, N., & Plotnikov, A. 2001, JASTP, 63, 1941
Ajluni, T., Everett, D., Linn, T., et al. 2015, OSIRIS-REx, Returning the Asteroid Sample, IEEE Aerospace Conf. (Piscatway, NJ: IEEE), 1
Albert, S., Bowman, D., Silber, E., & Dannemann Dugick, F. 2023, E&SS, 10, e2023EA003149
Anderson, J. F., Johnson, J. B., Bowman, D. C., & Ronan, T. J. 2018, SeiRL, 89, 153
Anderson, J. F., Johnson, J. B., Mikesell, T. D., & Liberty, L. M. 2023, ComEE, 4, 399
Arrowsmith, S., Hale, J., Burlacu, R., et al. 2011, Infrasound Signal Characteristics from Small Earthquakes in 2011 Monitoring Research Review: Ground-Based Nuclear Explosion Monitoring Technologies (Los Alamos, NM: Los Alamos National Lab.)
Arrowsmith, S., ReVelle, D., Edwards, W., & Brown, P. 2008a, EM&P, 102, 357
Arrowsmith, S. J., Drob, D. P., Hedlin, M. A. H., & Edwards, W. 2007, JGRD, 112, D09304
Arrowsmith, S. J., Hedlin, M. A. H., Stump, B., & Arrowsmith, M. D. 2008b, BuSSA, 98, 768
Avdellidou, C., & Vaubaillon, J. 2019, MNRAS, 484, 5212
Balachandran, N. K., & Donn, W. L. 1971, GeoJ, 26, 135
Banfield, D., Spiga, A., Newman, C., et al. 2020, NatGe, 13, 190
Belton, M. J. 2004, Mitigation of Hazardous Comets and Asteroids (Cambridge: Cambridge Univ. Press)
Beshore, E., Lauretta, D., Boynton, W., et al. 2015, The OSIRIS-REx Asteroid Sample Return Mission, IEEE Aerospace Conf. (Piscataway, NJ: IEEE), 1
Blaske, C. H., O'Rourke, J. G., Desch, S. J., & Borrelli, M. E. 2023, JGRE, 128, e2023JE007914
Blewitt, G., Hammond, W. C., Kreemer, C., et al. 2009, JGeod, 83, 335
Blom, P., Gammans, C., Delbridge, B., & Carmichael, J. D. 2024, ASAJ, 155, 1667
Bowman, D., Lees, J., Cutts, J., et al. 2019, Geoacoustic Observations on Drifting Balloon-Borne Sensors, in Infrasound Monitoring for Atmospheric Studies, ed. A. Le Pichon, E. Blanc, & A. Hauchecorne (Cham: Springer), 125
Bowman, D. C., & Albert, S. A. 2018, GeoJI, 213, 1524
Bowman, D. C., & Krishnamoorthy, S. 2021, GeoRL, 48, e2021GL094861
Bowman, D. C., & Lees, J. M. 2018, GeoRL, 45, 5144
Brachet, N., Brown, D., Bras, R., et al. 2010, Monitoring the Earth's Atmosphere with the Global IMS Infrasound Network, in Infrasound Monitoring for Atmospheric Studies, ed. A. Le Pichon, E. Blanc, & A. Hauchecorne (Dordrecht: Springer), 77
Brissaud, Q., Krishnamoorthy, S., Jackson, J. M., et al. 2021, GeoRL, 48, e2021GL093013
Bronshten, V. A. 1983, Physics of Meteoric Phenomena, Trans. from Russian (Dordrecht: Reidel)
Brown, P., Spalding, R. E., ReVelle, D. O., et al. 2002, Natur, 420, 294
Brown, P. G., Assink, J. D., Astiz, L., et al. 2013, Natur, 503, 238
Caudron, C., Taisne, B., Perttu, A., et al. 2016, GSL, 3, 26
Ceplecha, Z., Borovička, J., Elford, W. G., et al. 1998, SSRv, 84, 327
Chapman, C. R. 2008, EM&P, 102, 417
Cumming, G. L. 1989, CaJES, 26, 1350
D'Auria, L., Marotta, E., Martini, M., & Ricciolino, P. 2006, JGRB, 111, B10307
Daubar, I. J., Fernando, B. A., Garcia, R. F., et al. 2023, PSJ, 4, 175
den Ouden, O. F. C., Assink, J. D., Oudshoorn, C. D., et al. 2021, AMT, 14, 3301
Devillepoix, H. A. R., Cupák, M., Bland, P. A., et al. 2020, P&SS, 191, 105036
Drolshagen, G., Koschny, D., Drolshagen, S., et al. 2017, P&SS, 143, 21
Edwards, W. N., Eaton, D. W., & Brown, P. G. 2008, RvGeo, 46, RG4007
Edwards, W. N., Eaton, D. W., McCausland, P. J., et al. 2007, JGRB, 112, B10306
Evans, L. B., Bass, H. E., & Sutherland, L. C. 1972, ASAJ, 51, 1565
Evers, L. G., & Haak, H. W. 2003, GeoRL, 30, 2246
Fang, G., Li, Y. E., Zhao, Y., & Martin, E. R. 2020, GeoRL, 47, e2019GL086115
Fernando, B., Charalambous, C., Saliby, C., et al. 2024, Seism, 3, 1154
Fitzgerald, T. J. 1997, JASTP, 59, 829
Followill, F. E., Wolford, J. K., & Candy, J. V. 1997, Proc. SPIE, 3081, 266
Forbes, J. M., & Roble, R. G. 1990, JGR, 95, 201
Francis, S. R., Johnson, M. A., Queen, E., & Williams, R. A. 2024, in 46th Annual AAS Guidance, Navigation and Control (GN&C) Conf. (Breckenridge, CO: American Astronautical Society), https://ntrs.nasa.gov/citations/20240000629
Fujita, K., Yamamoto, M.-y., Abe, S., et al. 2011, PASJ, 63, 961
Garcés, M. A., Bowman, D., Zeiler, C., et al. 2022, Signals, 3, 209
Garcia, R. F., Daubar, I. J., Beucler, É., et al. 2022, NatGe, 15, 774
Giardini, D., Lognonné, P., Banerdt, W. B., et al. 2020, NatGe, 13, 205
Gran, R. 2023, NASA Finds Likely Cause of OSIRIS-REx Parachute Deployment Sequence, https://phys.org/news/2023-12-nasa-osiris-rex-parachute-deployment-sequence.html#google_vignette
Hartog, A. H. 2017, An Introduction to Distributed Optical Fiber Sensors (Boca Raton, FL: CRC press)
Ishihara, Y., Furumoto, M., Sakai, S., & Tsukada, S. 2004, GeoRL, 31, L14702
Ishihara, Y., Hiramatsu, Y., Yamamoto, M.-y., et al. 2012, EP&S, 64, 655
Janches, D., Heinselman, C. J., Chau, J. L., et al. 2006, JGRA, 111, A07317
Jenniskens, P., Albers, J., Tillier, C. E., et al. 2018, M&PS, 53, 2445
Kalashnikova, O., Horányi, M., Thomas, G. E., & Toon, O. B. 2000, GeoRL, 27, 3293
Krehl, P. O. K. 2011, EPJH, H36, 85
Krishnamoorthy, S., & Bowman, D. C. 2023, GeoRL, 50, e2022GL100978
Krishnamoorthy, S., Bowman, D. C., Komjathy, A., et al. 2020, ASAJ, 148, 2361
Langston, C. A. 2004, JGRB, 109, B12309
Lauretta, D., Balram-Knutson, S., Beshore, E., et al. 2017, SSRv, 212, 925

Le Pichon, A., GuéRin, J. M., Blanc, E., & Reymond, D. 2002, JGRD, 107, 4709
Lin, T.-L., & Langston, C. A. 2009a, JGRB, 114, B04303
Lin, T.-L., & Langston, C. A. 2009b, JGRB, 114, B04304
Lindsey, N. J., Martin, E. R., Dreger, D. S., et al. 2017, GeoRL, 44, 11
Lognonné, P., Banerdt, W. B., Pike, W. T., et al. 2020, NatGe, 13, 213
Luo, Y., Yao, Y., & Shan, L. 2020, Senso, 20, 3201
Marcillo, O., Johnson, J. B., & Hart, D. 2012, JAtOT, 29, 1275
Matoza, R., Fee, D., Green, D., & Mialle, P. 2019, Volcano Infrasound and the International Monitoring System, in Infrasound Monitoring for Atmospheric Studies, ed. A. Le Pichon, E. Blanc, & A. Hauchecorne (Cham: Springer), 1023
Matoza, R. S., Fee, D., Assink, J. D., et al. 2022, Sci, 377, 95
Meech, K. J., Weryk, R., Micheli, M., et al. 2017, Natur, 552, 378
Miller, K. L., Torr, D. G., & Richards, P. G. 1986, JGR, 91, 4531
Moorhead, A. V., Brown, P. G., Campbell-Brown, M. D., et al. 2017, P&SS, 143, 209
Mutschlecner, J., & Whitaker, R. 2006, Infrasonic Signals from the Henderson, Nevada, Chemical Explosion, Los Alamos National Lab.
Nawab, S., Dowla, F., & Lacoss, R. 1985, ITASS, 33, 1114
Nishikawa, Y., Yamamoto, M.-y., Sansom, E. K., et al. 2022, PASJ, 74, 308
Nunn, C., Garcia, R. F., Nakamura, Y., et al. 2020, SSRv, 216, 89
Obenberger, K., Bowman, D., & Dao, E. 2022, RaSc, 57, e2021RS007413
Ortiz, H. D., Matoza, R. S., & Tanimoto, T. 2022, GeoRL, 49, e2021GL096225
Ortiz, J. L., Aceituno, F. J., Quesada, J. A., et al. 2006, Icar, 184, 319
Ortiz, J. L., Madiedo, J. M., Morales, N., et al. 2015, MNRAS, 454, 344
Otsuka, Y., Kotake, N., Tsugawa, T., et al. 2006, EP&S, 58, 159
Peña-Asensio, E., Visuri, J., Trigo-Rodríguez, J. M., et al. 2024, Icar, 408, 115844
Perevalova, N., Shestakov, N., Voeykov, S., et al. 2015, GeoRL, 42, 6535
Pilger, C., Ceranna, L., Ross, J. O., et al. 2015, GeoRL, 42, 2523
Pilger, C., Gaebler, P., Hupe, P., et al. 2020, Atmos, 11, 83
Pilger, C., Hupe, P., Gaebler, P., & Ceranna, L. 2021, GeoRL, 48, e2020GL092262
Plane, J. M. 2012, ChSRv, 41, 6507
Plooster, M. N. 1970, PhFl, 13, 2665
Popenhagen, S. K., Bowman, D. C., Zeiler, C., & Garcés, M. A. 2023, GeoRL, 50, e2023GL104031
Popova, O. P., Jenniskens, P., Emel'yanenko, V., et al. 2013, Sci, 342, 1069
Posiolova, L. V., Lognonné, P., Banerdt, W. B., et al. 2022, Sci, 378, 412
ReVelle, D. 1974, PhD thesis, Michigan Univ., Ann Arbor
ReVelle, D. O. 1976, JGR, 81, 1217
Revelle, D. O. 1997, NYASA, 822, 284
ReVelle, D. O., Edwards, W., & Sandoval, T. D. 2005, M&PS, 40, 895
ReVelle, D. O., & Edwards, W. N. 2007, M&PS, 42, 271
Ronan, T. J. 2017, MS thesis, UNC Chapel Hill
Rosenblatt, B. B., Johnson, J. B., Anderson, J. F., et al. 2022, BVol, 84, 103
Sansom, E. K., Devillepoix, H. A., Yamamoto, M.-y., et al. 2022, PASJ, 74, 50
Sarli, B. V., & Tsuda, Y. 2017, AcAau, 138, 225
Scamfer, L. T., & Anderson, J. F. 2023, GeoRL, 50, e2023GL104635
Seyfried, M., Lohse, K., Marks, D., et al. 2018, VZJ, 17, 1
Shimada, S., Fujinawa, Y., Sekiguchi, S., et al. 1990, Natur, 343, 631
Silber, E. A. 2024, AJ, 168, 17
Silber, E. A., Boslough, M., Hocking, W. K., et al. 2018, AdSpR, 62, 489
Silber, E. A., Bowman, D. C., & Albert, S. 2023a, Atmos, 14, 1473
Silber, E. A., Bowman, D. C., & Ronac Giannone, M. 2023b, RemS, 15, 542
Silber, E. A., & Brown, P. 2019, Infrasound Monitoring as a Tool to Characterize Impacting Near-Earth Objects (NEOs), in Infrasound Monitoring for Atmospheric Studies, ed. A. Le Pichon, E. Blanc, & A. Hauchecorne (Cham: Springer), 939
Silber, E. A., & Brown, P. G. 2014, JASTP, 119, 116
Silber, E. A., ReVelle, D. O., Brown, P. G., & Edwards, W. N. 2009, JGRE, 114, E08006
Slad, G., & Merchant, B. J. 2021, Evaluation of Low Cost Infrasound Sensor Packages SAND2021-13632; 701386, Sandia National Lab.
Stopa, J. E., Cheung, K. F., Garcés, M. A., & Badger, N. 2012, JGRC, 117, C12017
Swaim, T., Spillman, K., Hough, E., et al. 2023, Development and Evaluation of Windscreen Designs for High Altitude Balloons in Proc. Meetings on Acoustics 51 (Melville, NY: AIP), 2pCA6
Tatum, T. A., Anderson, J. F., & Ronan, T. J. 2023, WRR, 59, e2023WR034554
Trigo-Rodríguez, J. M., Dergham, J., Gritsevich, M., et al. 2021, AdAst, 2021, 8852772
Tsikulin, M. 1970, Shock Waves during the Movement of Large Meteorites in the Atmosphere DTIC Document AD 715-537, Nat. Tech. Inform. Serv., Springfield, VA
Vera Rodriguez, I., Isken, M. P., Dahm, T., et al. 2023, SeiRL, 94, 731
Watanabe, J.-i., Ohkawa, T., Sato, M., et al. 2011, PASJ, 63, 955
Whipple, F. 1930, QJRMS, 56, 200
Yamada, T., & Yoshihara, K. 2022, Hayabusa2 Sample-return Capsule: System Description and Re-entry Flight, in Hayabusa2 Asteroid Sample Return Mission, ed. M. Hirabayashi & Y. Tsuda (Amsterdam: Elsevier), 477
Yamamoto, M.-y., Ishihara, Y., Hiramatsu, Y., et al. 2011, PASJ, 63, 971
Yang, Y.-M., Komjathy, A., Langley, R. B., et al. 2014, RaSc, 49, 341